

DIGITAL ACCESS TO SCHOLARSHIP AT HARVARD
DASH.HARVARD.EDU

HARVARD LIBRARY


Dielectric Elastomer Actuators as Artificial Muscles for Soft Robotic Applications

Citation

Duduta, Mihai. 2019. Dielectric Elastomer Actuators as Artificial Muscles for Soft Robotic Applications. Doctoral dissertation, Harvard University, Graduate School of Arts & Sciences.

Link

http://nrs.harvard.edu/urn-3:HUL.InstRepos:41121308

Terms of use

This article was downloaded from Harvard University's DASH repository, and is made available under the terms and conditions applicable to Other Posted Material (LAA), as set forth at

https://harvardwiki.atlassian.net/wiki/external/NGY5NDE4ZjgzNTc5NDQzMGIzZWZhMGFlOWI2M2EwYTg

Accessibility

https://accessibility.huit.harvard.edu/digital-accessibility-policy

Share Your Story

The Harvard community has made this article openly available.
Please share how this access benefits you. Submit a story

Dielectric Elastomer Actuators as Artificial Muscles for Soft Robotic Applications

A DISSERTATION PRESENTED
BY
MIHAI DUDUTA
TO
THE JOHN A. PAULSON SCHOOL OF ENGINEERING AND APPLIED SCIENCES

IN PARTIAL FULFILLMENT OF THE REQUIREMENTS
FOR THE DEGREE OF
DOCTOR OF PHILOSOPHY
IN THE SUBJECT OF
ENGINEERING SCIENCES

HARVARD UNIVERSITY
CAMBRIDGE, MASSACHUSETTS
DECEMBER 2018

© 2018 - Mihai Duduta
All rights reserved.

Thesis advisors: Robert J. Wood and David R. Clarke Mihai Duduta

Dielectric Elastomer Actuators as Artificial Muscles for Soft Robotic Applications

Abstract

Dielectric elastomer actuators (DEAs) are electro-mechanical transducers which can convert an electrical input into mechanical work. They have clear advantages (i.e., soft elastomers, direct electrical to mechanical conversion) which make them particularly promising for soft robotics applications. Unfortunately, most DEAs have severe limitations: low output forces, the need for a rigid frame, high voltages needed for actuation, slow response speed, low energy density, and challenging integration with other components. This thesis describes a material-focused approach to address these limitations, using unique robotic demonstrations as proof of the material and device capabilities. To ensure the final DEA is completely soft, I focused on strain stiffening elastomer materials, made from UV curable liquid precursors. These are combined with ultra-thin carbon nanotube (CNT) mats in a multilayering process which yields robust actuators, capable of bending, linear expansion, as well as contraction. The process gives control over each layer's thickness, meaning low voltage demonstrations are possible, such as bending at 300-600 V. Additionally, each electrode can be made from a specific ink, processed independently from the rest of the multilayer. Using thermally treated electrodes at low areal densities of CNTs, I built multilayers that can be charged to high electric fields (>200 $V/\mu m$), to do mechanical work at high energy density (10-20 J/kg).

Using a multilayer bending beam, I demonstrated a crawling robot, capable of high speed locomotion (>1 body length / second). The crawling speed was set by the viscoelasticity of the elastomer, showing the strong dependence of robot performance on material properties. Additionally, the same bending beams were built into a bimorph used to power a swimming robot. By incorporating a pressure sensor and reconfiguring the robot to dive, I demonstrated the first ever autonomous DEA-powered robot. Lastly, using high energy density DEAs and a composite structure, I showed the first ever DEA-powered jumping robot. Overall, the multilayer platform allowed me to use material improvements (elastomers with lower viscoelastic losses, electrodes with higher conductivity, etc.) to build robots with unprecedented capabilities (high energy density, large bandwidth, impulsive behavior, etc.).

Contents

1 Introduction **3**

1.1 Electrically driven actuators 4

1.2 Limitations of dielectric elastomer actuators 7

1.3 Goals and objectives 11

2 Material selection and process optimization for creating multilayered dielectric elastomer actuators **15**

2.1 Experimental details 18

2.2 Multilayering method 19

2.3 Mechanical properties of multilayers 22

2.4 Adhesive properties of multilayers 22

2.5 Electrical properties of CNTs on elastomers 27

2.6 Actuation performance of multilayers 29

2.7 Low voltage actuation 32

2.8 Multimorph demonstration 33

2.9 Summary 35

3 Optimized carbon nanotube electrodes for high energy density actuators **38**

3.1 Experimental methods 40

3.2 Electrode composition impact on dielectric breakdown 43

3.3 Ink selection process 46

3.4 Artificial muscle demonstrations 56
3.5 Actuator bandwidth and cycle life 61
3.6 Artificial muscular hydrostat demonstration 63
3.7 Summary 63

4 Swimming and crawling robots powered by multilayer DEAs 65
4.1 Unimorphs as inchworm robots 66
4.2 Multi-legged crawling robot 70
4.3 Motivation for swimming applications 73
4.4 Bimorph actuator design 75
4.5 Bimorph fin testing setup 76
4.6 Bimorph actuator optimization 77
4.7 Robot design 82
4.8 Manuevers in planar swimming 84
4.9 Autonomous vertical diving 84
4.10 Power consumption 87
4.11 Summary 88

5 Latch-free dielectric elastomer actuator powered jumping robot 89
5.1 Biological inspiration 91
5.2 Fabrication 92
5.3 Modeling the mechanical and electrical energy stored in the DEA 95
5.4 Power amplification 96
5.5 Demonstrations 98
5.6 Next steps 99

6 Conclusions 101
6.1 Multilayer process and materials 102
6.2 Robotic demonstrations 102

References 117

Listing of figures

1.1 Operation mode of a dielectric elastomer actuator 5
1.2 Linear deformation modes of DEAs 6
1.3 Examples of DEA-powered robots with rigid frames 8
1.4 Comparison with natural muscles 10
1.5 Examples of robots which use DEAs for auxiliary tasks 11
1.6 Examples of walking and crawling robots powered by DEAs . . . 12

2.1 Chemical structures of oligomers used 17
2.2 Multilayering process 17
2.3 Cross section imaging of multilayers 21
2.4 Stress vs. strain curves for pure elastomers 23
2.5 Mechanical properties of multilayers 24
2.6 Elastomer adhesive properties 26
2.7 Sheet resistance of CNTs on elastomers under strain 28
2.8 Actuation without pre-strain 29
2.9 Actuator bandwidth and viscoelasticity of elastomers 31
2.10 Low voltage actuation 34
2.11 Multimorph demonstration 35

3.1 Breakdown fields vs. area coverage 44
3.2 Breakdown fields vs. elastomer modulus 45
3.3 Scanning electron microscope images of electrodes 47

3.4 Electrodes on PTFE and elastomer substrates 48
3.5 Example roll actuator 49
3.6 Early testing current peaks 50
3.7 Self-clearing behavior 52
3.8 Capacitance measurement setup 53
3.9 Impact of electrode heating on actuator performance 54
3.10 Impact of thermal treatment 55
3.11 Artificial bicep demonstration 57
3.12 Linear contracting actuators 58
3.13 Linear contracting actuator performance 59
3.14 Roll actuator performance 60
3.15 Actuator energy density and relative bandwidth 60
3.16 Limits of actuator performance 62
3.17 Artificial muscular hydrostat 63

4.1 Unimorph fabrication and operation 67
4.2 Crawling inchworm robot 69
4.3 Inchworm robot crawling speeds 70
4.4 Multi-legged robot construction 71
4.5 Multilegged robot locomotion 72
4.6 Bimorph construction and operation 75
4.7 Fin thrust measurement setup 78
4.8 Thrust output vs. time 79
4.9 Thrust output vs. frequency 80
4.10 Thrust output vs. number of layers 81
4.11 Thrust output vs. elastomer stiffness 82
4.12 Swimming robot design 83
4.13 Horizontal swim demonstration 85
4.14 Vertical dive demonstration 86
4.15 Autonomous dive depth control 87

5.1 Click beetle jumping mechanism 91

5.2 Spore jumping 93
5.3 Fabrication of pre-stretched structure 94
5.4 Energy states in pre-stretched structure 97
5.5 Jump demonstration 100

To M.

Acknowledgments

First I would like to thank my two advisors, Profs. Robert Wood and David Clarke, for their mentoring, support, guidance, and freedom to explore this exciting research area. I will forever be grateful for the truly collaborative atmosphere they fostered, and hope to emulate it in all my future endeavors.

I would also like to thank the third committee member, Professor Zhigang Suo, for his enthusiastic support, and the other faculty who have provided resources and insight along the way, in particular Profs. Radhika Nagpal and George Lauder.

There are numerous other individuals who have helped me get to this point, and all have earned my gratitude. I acknowledge the administrators who guided me through the unique challenges of being a part of two groups, and made sure I could focus on research: Hetchen Ehrenfeld, Greg Freeburn, Sarah Lefebvre, Jane Salant, and Mike Smith. I recognize the support from the senior lab members who helped me get started, and find my own area of interest: Drs. Kevin Galloway, Roger Diebold, and Samuel Shian. I am grateful to have had the opportunity to work with, and learn from such a diverse pool of talent. I want to appreciate those who took the time, and helped made my research more impactful: Ehsan Hajiesmaili, Florian Berlinger, and Dr. Zeynep Temel.

At Harvard I was excited to find an environment that fosters innovation in teaching, and places great emphasis on mentoring. I want to thank Dr. Pia Soerensen for the opportunity to teach an inspiring course, and the students who helped me become a better mentor: Victor Champagne, Eesha Khare, and Anne Raheem.

I am truly grateful for all of the support of my friends and family, both near and far. Boston has been my home for many years, and a great place to live and learn because of the friends I've made. At the same time, my family in Romania and London have kept me grounded and motivated, while providing me with encouragement and support.

Lastly, I want to thank my wife, Dr. Patricia Tcaciuc, who has been an endless source of joy, inspiration, motivation, support, care, knowledge, wisdom, and love.

List of Authors

The following authors contributed to Chapter 1: Mihai Duduta.

The following authors contributed to Chapter 2: Mihai Duduta, Robert J. Wood, David R. Clarke.

The following authors contributed to Chapter 3: Mihai Duduta, Ehsan Hajiesmaili, Huichan Zhao, Robert J. Wood, David R. Clarke.

The following authors contributed to Chapter 4: Mihai Duduta, Florian Berlinger, Hudson Gloria, Radhika Nagpal, Robert J. Wood, David R. Clarke.

The following authors contributed to Chapter 5: Mihai Duduta, Florian Berlinger, F. Zeynep Temel, Robert J. Wood, David R. Clarke.

The following authors contributed to Chapter 6: Mihai Duduta.

List of Publications

Duduta, M., Wood, R.J. and Clarke, D.R., **2016**, April. Flexible, stretchable electroadhesives based on acrylic elastomers. In *Electroactive Polymer Actuators and Devices (EAPAD)* 2016 (Vol. 9798, p. 97981D). International Society for Optics and Photonics.

Duduta, M., Wood, R.J. and Clarke, D.R., **2016**. Multilayer dielectric elastomers for fast, programmable actuation without prestretch. *Advanced Materials*, 28(36), pp.8058-8063.

Duduta, M., Clarke, D.R. and Wood, R.J., **2017**, May. A high speed soft robot based on dielectric elastomer actuators. *In Robotics and Automation (ICRA), 2017 IEEE International Conference on* (pp. 4346-4351). IEEE.

Berlinger, F., Duduta, M., Gloria, H., Clarke, D., Nagpal, R. and Wood, R., **2018**, May. A Modular Dielectric Elastomer Actuator to Drive Miniature Autonomous Underwater Vehicles. *In 2018 IEEE International Conference on Robotics and Automation (ICRA)* (pp. 3429-3435). IEEE.

Zhao, H., Hussain, A.M., Duduta, M., Vogt, D.M., Wood, R.J. and Clarke, D.R., **2018**. Compact Dielectric Elastomer Linear Actuators. *Advanced Functional Materials*, 28(42), p.1804328.

Duduta, M., Hajiesmaili, E., Zhao, H., Wood, R.J. and Clarke, D.R., Realizing the Potential of Dielectric Elastomer Artificial Muscles, *under review*.

1 Introduction

Robots are becoming more prevalent in unpredictable environments, such as near or on the human body. These adaptable machines need to take on a variety of shapes: from soft robots for exploration, to wearable devices for rehabilitation and communication, and novel surgical tools that conform to specific shapes and sizes. The greatest challenge of these soft machines is the technology required to actuate movement for locomotion, manipulation, or another more specific tasks. Since the devices need to be compliant, most off-the-shelf solutions, such as motors, are not suitable, and new technologies need to be developed.

Recent research has focused mainly on pneumatic and hydraulic actuation technologies, that use fluids to deform soft elastomer bodies. After early proof of concept examples [1, 2], multiple capabilities have been demonstrated, including linear contraction to match natural muscles[3], active camouflage[4], and

combustion for fast locomotion[5]. Multiple fabrication technologies have been demonstrated, including molding[6], 3D printing[7], and additive assembly[8]. Additional functionality has been added with strain[9], pressure[10], temperature sensing[11], as well as catalysis for controlled fuel decomposition, and on board microfluidic logic[12]. Despite the numerous variants, the fundamental technology has a significant limitation: it requires either a pump, a method to decompose a fuel, or high pressure storage. The pump becomes a rigid limitation for example, in creating a completely untethered system[13]. Meanwhile, on board fuels can be decomposed quickly but come with safety concerns for some applications[14].

1.1 Electrically driven actuators

To bypass the need for a pump or fuel, other technologies have been developed to directly convert electrical energy into mechanical work. Such actuators can be more easily integrated with the rest of the device because of the ease of storing and converting electrical energy via high energy density rechargeable batteries and miniaturized power electronics. The actuation strategies depend on the materials used: conductive polymers can be incorporated in ionic polymer metal composites that deform when ions migrate inside the material[15]. Twisted carbon nanotube yarns can uncoil to produce contractile or torsional actuation under resistive heating[16]. The same type of resistive heating can be used to deform shape memory alloys[17] and polymers[18] made compliant by the design of the mechanism. Other mechanisms, such as electroosmotic flow, can be employed to create microfluidic actuators[19]. Generally speaking, none of the materials employed are stretchable elastomers, but achieve compliance through design, for example ionic polymer-metal composites (IPMCs) are only used in a bending configuration.

In contrast, dielectric elastomers are soft, stretchable materials, which convert an applied electric field to mechanical work[20, 21].The main focus of my thesis

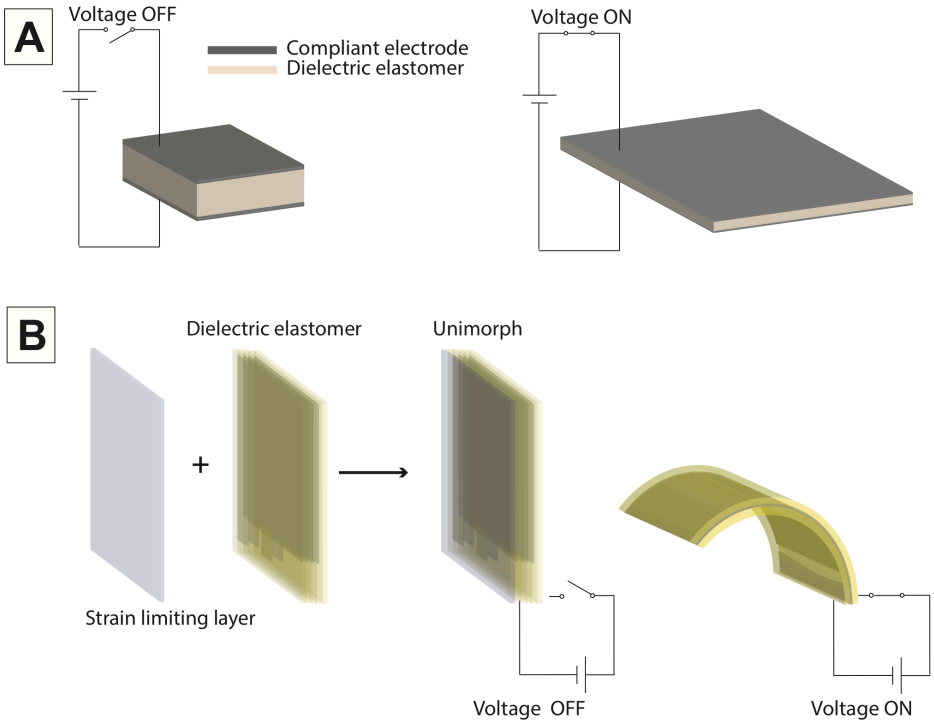


Figure 1.1: Operation mode of a dielectric elastomer actuator A. Schematic operation of a dielectric elastomer actuator. When a field is applied between the two compliant electrodes, a Maxwell stress develops and deforms the dielectric elastomer. **B.** The addition of a strain limiting layer prevents biaxial expansion and causes the unimorph to bend.

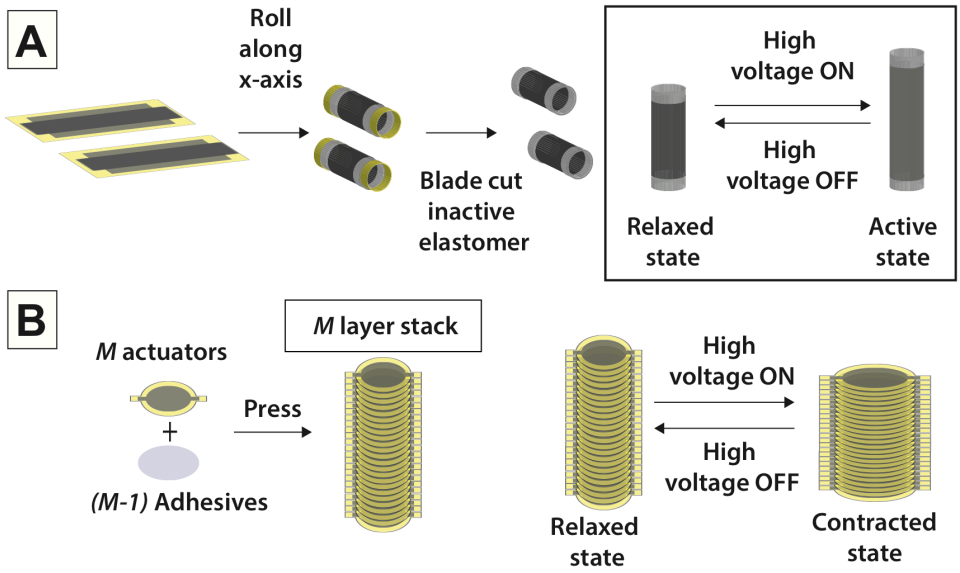


Figure 1.2: Linear deformation modes of DEAs A. Assembly of a roll-type actuator capable of linear expansion along its long axis. **B.** Assembly of a linear contracting actuator and operation mode.

has been the discovery and implementation of materials that overcome existing limitations of DEAs to broaden the range of potential robotic applications. Fundamentally, dielectric elastomer actuators operate as compliant capacitors. An electric field is applied to compliant electrodes on either side of a dielectric elastomer. The attraction between the two electrodes gives rise to a Maxwell stress that compresses the elastomer in the direction perpendicular to the plane of the electrodes (z-axis).

$$\sigma = \varepsilon_0 \varepsilon_r \left(\frac{V}{t}\right)^2 \tag{1.1}$$

where σ is the Maxwell stress, ε_0 is the permittivity of vacuum $(8.85 \cdot 10^{-12}\ \mathrm{F/m})$, ε_r is the dielectric constant of the elastomer, V is the applied voltage across the elastomer, and t is the thickness of the elastomer.

Because the elastomer is incompressible, contraction in the z direction is accompanied by expansion in the xy plane. Using strain limiting layers, the

expansion of the elastomer can be converted into bending[22] (Figure 1.1). By stacking multiple elastomers, the attraction between electrodes can be converted into linear contraction[23]. In the same way, a rolled elastomer can be used to make a linear expanding actuator[24] (Figure 1.2). Starting with the relationship between stress and strain:

$$\sigma = sE \tag{1.2}$$

where s is the strain in the elastomer and E is the Young's Modulus of the elastomer, when considering the mechanical energy density of the elastomer, it is most sensitive to the applied electric field across the elastomer (V/t):

$$u_e = \frac{s\sigma}{2} = \frac{\varepsilon_o^2 \varepsilon_r^2 E}{2} \left(\frac{V}{t}\right)^4 \tag{1.3}$$

where u_e is the mechanical energy density in the elastomer. Most DEAs rarely exhibit mechanical energy densities higher than 2 J/kg, matching only to the lower end of natural muscles (0.4 - 40 J/kg).

1.2 Limitations of dielectric elastomer actuators

Unfortunately, dielectric elastomer actuators suffer from significant material and performance constraints, that limit their use in robotics. The most significant material and device limitations are the following:

1. most elastomers need to operate in a pre-stretched state to avoid electromechanical instabilities[27]. To maintain a pre-stretched state, the elastomer is affixed to a rigid frame, which negates the advantages of the soft material, and imposes harsh constraints on the robot body. In some cases, the frame can be made flexible enough to allow for small deformations, sufficient for swimming[25] or crawling locomotion[26] (Figure 1.3). Overall, the DEAs are not modular, meaning the entire robot must be designed around the single degree of freedom of the actuator.

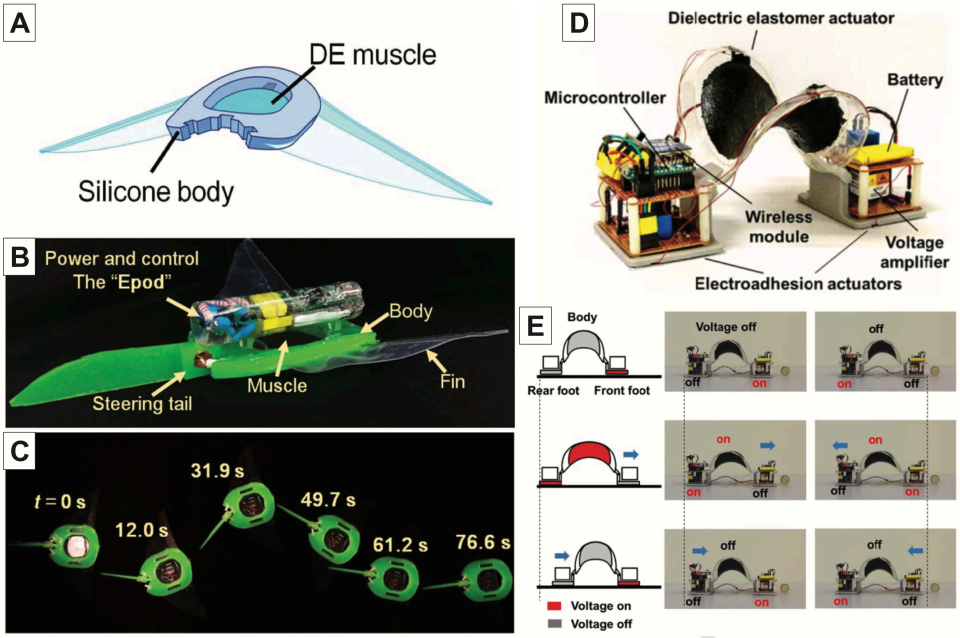


Figure 1.3: Examples of DEA-powered robots with rigid frames A. Model of the swimming robot from [25]. **B.** Swimming robot with on board high voltage power supply. **C.** Robot swimming trajectory viewed from above at different times. **D.** The individual components of the untethered robot from [26]. **E.** Schematic of locomotion of the untethered soft robot. One experimental cycle of the robot moving forward and backward. The dashed line represents the starting position.

2. DEAs are typically made from thick films that need high voltages for appreciable deformation. This scaling limitation emerges from Eq. 1.1, as the stress (or strain) in the material depends on the square of the applied electric field. The electric field (30-100 V/μm) is applied across thick films (30-300 μm) leading to high voltages (>10 kV) needed for appreciable deformation[28] in the range of sizes of interest (0.1-10 cm). Such high voltages can only be supplied by bulky power supplies, meaning high voltage DEAs can only operate in tethered systems.

3. when used as contracting actuators, DEAs have low energy density, limited by the maximum field that can be applied and reduced by the inactive components of the device. The earliest demonstrations[21] established DEAs as high energy density actuators (>3000 J/kg), only when considering just the active material in pre-stretched configurations (the elastomer is stretched bi-axially 3 $\times$ 3 its initial length along the x- and y-axes) at high electric fields (300 V/μm). When comparing to the power and energy requirements for different types of movement[29], we find DEAs operate in the lower range of natural muscle and are only suitable for lower power locomotion (swimming and crawling) (Figure 1.4). Still, DEAs have found use performing auxiliary tasks, such as steering, when the main propulsion task is solved by a different type of actuator[30] (Figure 1.5).

4. DEAs are typically slow actuators[31], their response speed limited by the viscoelasticity of the elastomer and high RC time constants. The most commonly used elastomer is an acrylic polymer with slow response known as VHB (<1 Hz). The slow response times lead to reduced speed in locomotion, as seen in multiple examples[32] (Figure 1.6). Alternative elastomers include silicones which have much faster response times (>100 Hz[33]), but different fabrication challenges.

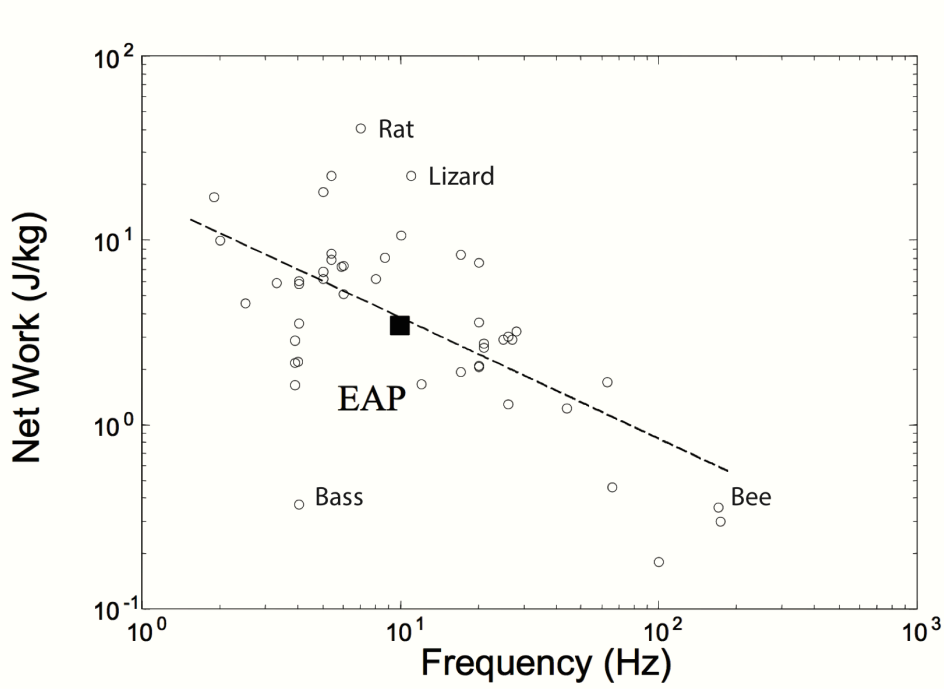


Figure 1.4: Comparison with natural muscles The energy density of natural muscles decreases as the actuation frequency increases, as shown in [29]. The dashed line corresponds to a target of performance for DEAs to allow for locomotion.

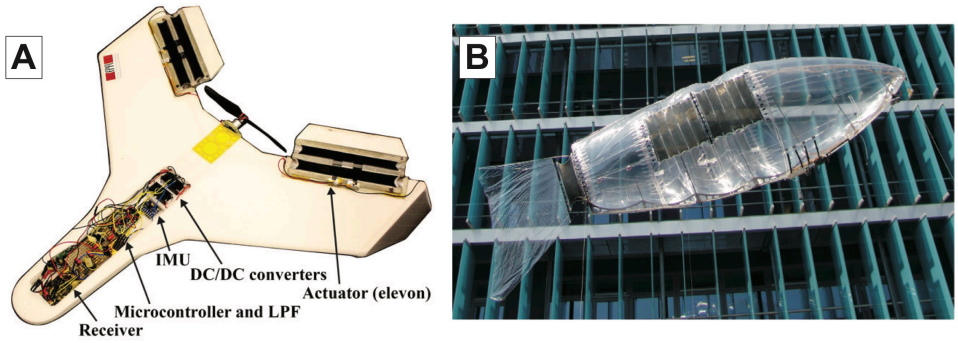


Figure 1.5: Examples of robots which use DEAs for auxiliary tasks A. Model of a UAV which uses DEAs to modify the robot's attitude[30]. **B.** Example of a DEA powered airship which locomotes by flapping its tail. The weight of the robot is balanced by the buoyancy of the helium gas used to inflate the airship.

1.3 Goals and objectives

To summarize, dielectric elastomer actuators are generally limited to use as relatively low force, small displacement, slow actuators in tethered systems that require high voltages for limited performance and usually a single degree of freedom. However, the simplicity of the system (i.e., a compliant capacitor) and high energy density in the active material alone ($>3000\,J/kg$) suggest that DEAs have the potential to operate as artificial muscles to power a range of devices. The following chapter summaries describe the material and device strategies adopted to address each of the previously listed limitations.

Chapter 2 presents a multilayering approach aimed at creating a completely soft DEA that does not require pre-stretch. Stacking multiple actuators is an established strategy for increasing the force output, and reducing the actuation voltage for DEAs. The first challenge was finding elastomers that actuate without pre-stretch and avoid the electromechanical instability: the solution was a class of UV curable liquid acrylic oligomers that exhibit a strain stiffening behavior. The second challenge was finding compliant electrodes that fit a multilayered

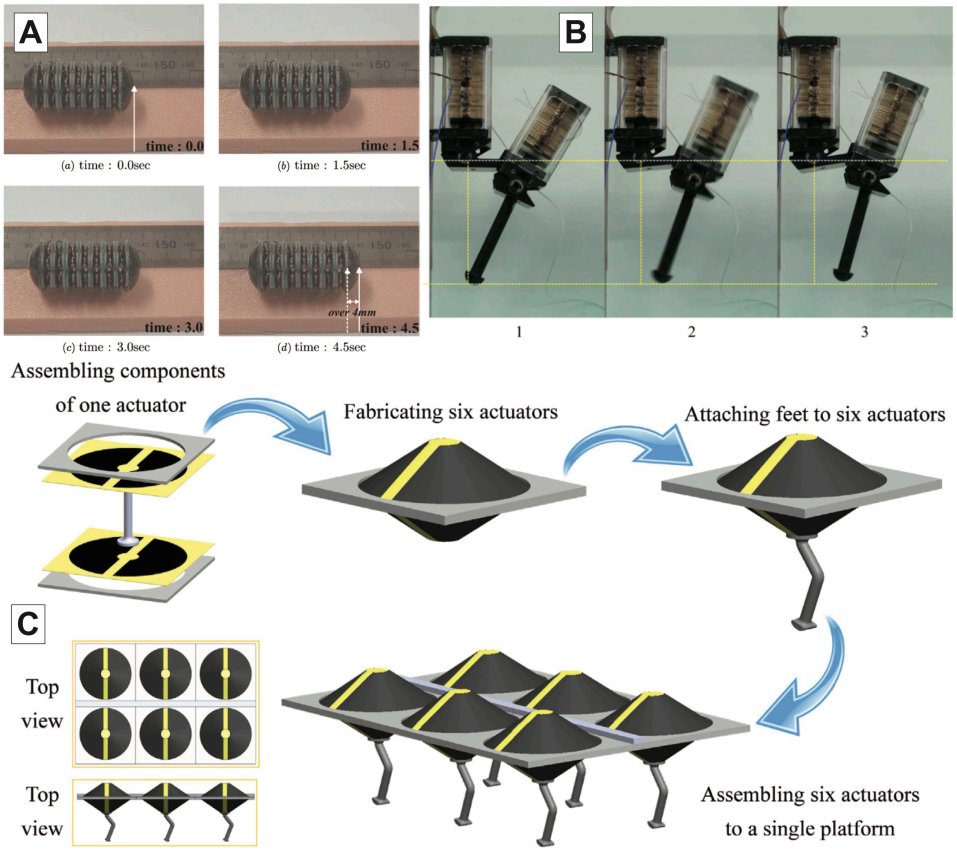


Figure 1.6: Examples of walking and crawling robots powered by DEAs **A.**, Crawling annelid-inspired robot powered by multiple DEA modules[32]. **B.** Linear contracting actuators used to power a leg with two degrees of freedom[34]. The range of motion of the leg is limited by the displacement of the two actuators. **C.**, Assembly steps for multiple degree-of-freedom actuators used in a walking robot. The robot still requires rigid frames to maximize the displacement in each actuator.

configuration without adding significant stiffness or thickness to the elastomer: the solution were mats of carbon nanotubes adhered directly onto the elastomer. The main drawback of multilayering is increased processing time, which was minimized by using UV curable elastomers and stamping of electrodes.

Chapter 3 presents a strategy to maximize the energy density of a multilayered dielectric elastomer actuator. I focused my efforts on finding materials that can sustain high applied electric fields in a multilayered configuration without undergoing detrimental dielectric breakdown. Additional processing was needed, such as thermal annealing of the electrodes to ensure the DEAs could withstand high electric fields ($>100\,\mathrm{V}/\mu\mathrm{m}$). The result is a dielectric elastomer actuator that produces a peak energy density of 19.8 J/kg, on the higher end of the capabilities of natural muscles, without requiring any rigid components.

Chapter 4 presents the impact of materials and fabrication to improve the performance of DEA-driven robots relative to the state of the art. The versatility of the multilayering process is demonstrated by independently varying elastomer parameters (modulus, tan delta) from fabrication and operation parameters (number of active layers, actuation frequency) to maximize speed in crawling and thrust for swimming. Moreover, for a swimming robot, the actuator power requirements can be satisfied by a small, portable power supply. In both cases, the actuator geometry can be optimized independently of the rest of the robot body.

Chapter 5 presents a novel jumping robot powered by DEAs. The mechanism is inspired by an insect, the click beetle, which is able to jump and invert its body without using legs. The robot uses a pre-stretched dielectric elastomer as the actuator, and the flexible frame holding the pre-stretch as a power amplification mechanism. The jumping robot can clear a height similar to its body length, in a jump which happens faster than 200 milliseconds. Unlike the mechanism observed in the click beetle, the jumping robot does not have a latch to rapidly release mechanical energy. Instead, the energy release is triggered by rapid discharge of the DEA compliant capacitor.

Chapter 6 summarizes the advances in materials synthesis, selection, processing, and characterization, as well as the robotic demonstrations made

possible by multilayer dielectric elastomer actuators. The chapter also outlines future research directions enabled by the multilayering process, showing its applicability in a wide range of areas, including robotics, haptics, flexible electronics, and more.

2

Material selection and process optimization for creating multilayered dielectric elastomer actuators

Despite their intrinsic simplicity, DEAs have two major limitations that prevent their wider adoption. The first is the need for pre-stretching of the elastomer in order to attain large actuation strains[35]. By pre-stretching, the well-established electromechanical instability is suppressed and higher actuation voltage can be attained before dielectric breakdown occurs[36]. However, pre-stretching is typically achieved with the use of a rigid frame, which in turn limits the integration of DEAs with other soft components. Some progress has been made to devise elastomer compositions, such as ones consisting of two

interpenetrating polymer networks (IPNs)[37]. In these network materials, the first elastomer is pre-stretched, then a second, interpenetrating polymer network is cross-linked throughout the first. When the first elastomer is released, the internal tensile stress is balanced by the compressive stress in the second network, and the elastomer retains some of the prestretch without using a rigid frame. Another approach that has shown some advantages is to manipulate the composition to create a rapid stiffening behavior above a certain stretch value, suppressing the onset of electromechanical instability[38].

The second major limitation of DEAs is the high voltage typically required for actuation (100 V/μm)[39]. Smaller actuation voltages (100-300 V) can be achieved by using much thinner elastomer films (3 μm)[40], but such films are very fragile and difficult to manipulate to create structures. The development of multilayer actuators has improved robustness[23] but as the thickness of the individual layers approaches the thickness of the electrodes, their combined stiffness limits the attainable actuation strains. Decreasing the thickness of the electrodes then becomes necessary, but this has proven difficult for silicone actuators because silicones, having low surface energies, adhere poorly to most other materials. Furthermore, good adhesion between the individual electrodes and elastomer layers in the multilayer is necessary to prevent delamination. Hitherto, the most reliable electrodes for silicone based actuators have been physical dispersions of carbon black particles in silicone. However, these are much stiffer than the silicone itself and invariably have appreciable thickness (typically >1 μm)[41–43]. By comparison, acrylic elastomers are most often good adhesives and can incorporate a wider variety of conductors with minimal increase in stiffness, including conductive powders such as carbon black and silver nanowires[44, 45]. As will be shown in this work, certain acrylic compositions can readily incorporate carbon nanotube (CNT) mats so the electrodes can be much thinner and still provide percolative electrical conduction. The acrylic elastomers also have sufficient adhesion between the

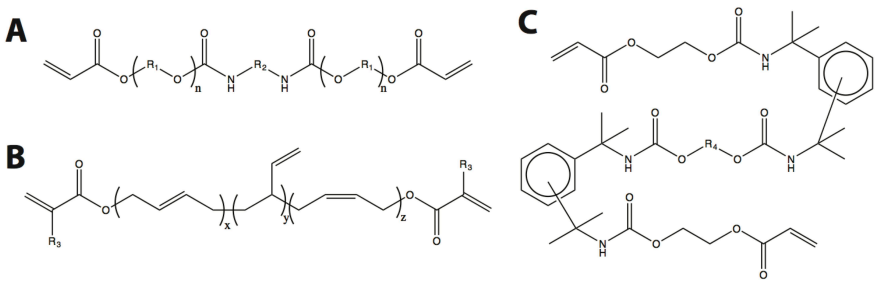


Figure 2.1: Chemical structures of oligomers used. **A**: CN9021, **B**: CN9014, **C**: CN9018.

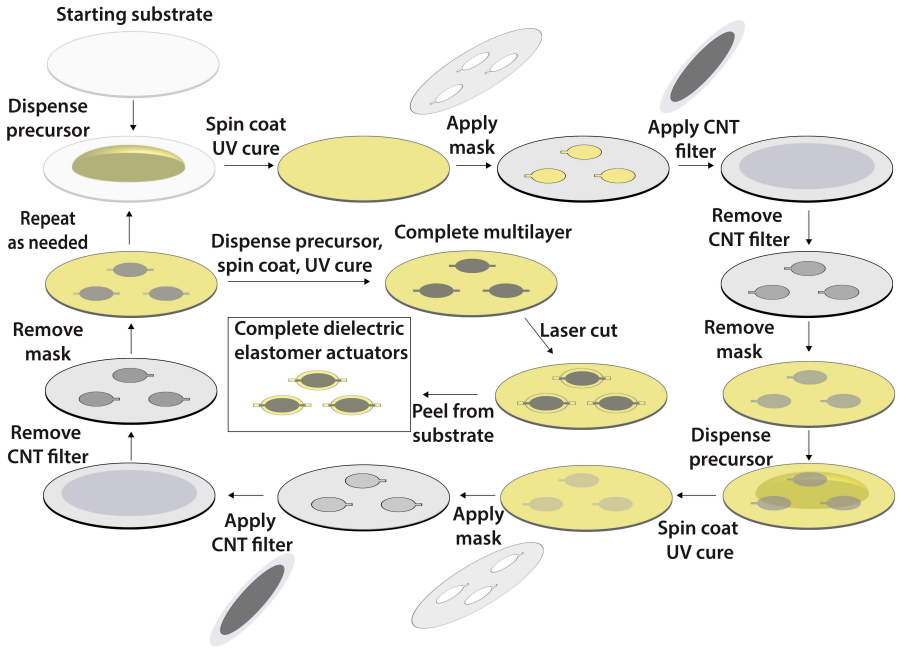


Figure 2.2: Multilayering process. Schematic of the steps in the assembly process for multilayer dielectric elastomers incorporating carbon nanotube electrodes.

layers to build mechanically robust multilayer devices.

2.1 Experimental details

The elastomer oligomers used (CN9021, CN9014, and CN9018) were obtained from Sartomer Company (Exton, PA) and the cross-linker HDDA was procured from Sigma-Aldrich (St. Louis, MO). The chemical structures of the oligomers are shown in Figure 2.1. Evaluation of the mechanical and electrical properties of the elastomer and electrodes was based on standards from the American Society for Testing and Materials (ASTM) or current DEA standards[46]. The CN9021 oligomer (A) was the basis for the composition reported by Niu et al.[38], while CN9014 (B) and CN9018 (C) are being presented for the first time. The oligomers were spin coated onto PETG-modified substrates in a Model WS-650MZ-23NPP/LITE spin coater from Laurell Technologies Corporation. UV curing was performed in an Ever Bright Printing Machine Fty. Ltd that has a peak output at 365 nm. The electrode mask was laser cut from Mylar silicone-coated to minimize adhesion to the elastomers.

The electrodes were made by filtering aqueous carbon nanotube (CNT) inks through PTFE filters. The inks were either purchased from commercial suppliers (NanoC, Westwood, MA) or made by sonicating CNT powders (P3, Carbon Solutions, Riverside, CA) in aqueous 1M solution of sodium dodecyl sulfate for 1 minute. The CNTs electrodes were then directly stamped onto the UV cured acrylic elastomers through the mask. The electrode size was limited by the size of available PTFE filters used to transfer the CNTs (70 mm inner diameter). The spin coat, cure, and electrode transfer process were repeated to produce the desired number of layers. The devices were laser cut (Versalaser, CO_2 60 W) from the multilayer stack. The heat-effect zone from the laser cutting was found to be approximately 0.5 mm, for cuts up to 1 mm thick.

To ensure good connections to all layers, the exposed edges of the tabs were coated with colloidal silver (Ted Pella, Redding, CA); the dried colloidal silver was protected by carbon tape and connected to the power source.

The layer thicknesses were measured in cross sections using a LEXT OLS4000 Olympus Confocal Microscope or using an Ultra 55 Scanning Electron Microscope (SEM, Zeiss, Oberkochen, Germany). For SEM imaging, the electrodes were transferred from the PTFE filters onto carbon tape (Electron Microscopy Sciences, Hatfield, PA). The cross-sections were prepared by laser cutting, blade cutting, or freezing in liquid nitrogen and fracturing the multilayer.

The unimorph actuators were fabricated by adhering the multilayers on a stiff sheet of Mylar (12.5 μm thick) in a cantilever configuration: 20 mm long and 5 mm wide. The thickness was 0.05-1 mm, depending on the number of layers coated and the spin coating conditions. Mylar was selected as it has a relatively large Young's modulus (1 GPa) and little thickness variability.

The actuation power source was a TREK Model 610E. The blocked force was measured with a Futek 50 g load cell in contact with the free end of the unimorph actuator. Similarly, images of flexural displacement of the end of the unimorph were recorded as a function of applied voltage. The end displacements were determined from photos or videos (180 frames/s) using ImageJ software. The actuation bandwidth was determined by applying an alternating current from a Wavetek 75 Arbitrary Waveform Generator and measuring the peak-to-peak time-averaged displacement.

2.2 Multilayering method

In this chapter, we describe a combination of materials and multilayer fabrication method that overcomes these existing limitations, namely the need for pre-stretch and the high actuation voltage. Moreover, the combination of materials and the method provides the opportunity to create novel actuator structures through the design and placement of the electrodes. These outcomes become possible when, as achieved in this work, the electrode thickness is sufficiently small that the electrodes do not significantly alter the thickness or the stiffness of the elastomer layers. Our approach is to start with an acrylic composition that can be spin cast as a liquid, and then UV cured. The base acrylic

composition has already been shown to be capable of actuation without prestretch[38] and several modifications are introduced in this work. The acrylic compositions also have sufficient inherent adhesion that an ultrathin mat of CNTs[47] can be transferred directly onto it through a mask to create compliant electrodes. A new elastomer layer can then be spin coated on top, UV cured and the process repeated to create the desired number of multilayers (Fig. 2.2). As shown in this work, the fabrication process can be modified to program complex actuator motions through simple geometric changes in electrode design, something that is not achievable using more traditional methods and materials.

To demonstrate the viability of this approach, unimorphs have been fabricated by building up the multilayers, then attaching a thin Mylar sheet, which serves as the passive strain-limiting layer. Evaluation of the mechanical properties of the elastomers, the adhesive strength of the layers, the electrcal properties of CNT electrodes on elastomers, as well as unimorph characteristics are described in the following sections. These include experiments of the unimorph frequency response, demonstrating how bandwidth can be controlled by composition. Improvements in actuator bandwidth are necessary for acrylic-based DEAs, to compete with silicone elastomers in terms of actuation response speed[33, 48].

An example DEA was fabricated via the method shown in Figure 2.2, then imaged in cross section using scanning electron microscopy. Crosssections of the multilayers indicated that there was good layer uniformity, as illustrated in the SEM image of Figure 2.3, for a 30-layer structure using elastomer C as the base and twenty eight layers of 10% HDDA cross-linked precursor C. In this example the average layer thickness was 30.5 ± 1.6 μm without CNT electrodes. For example **A**, the region on the left corresponds to the laser cut edge of the actuator and shows each layer has a thickness of 30 μm. The region on the right corresponds to the edge cut with a blade to make electrical connections. The darker regions every other layer correspond to areas in which CNT electrodes are placed. The CNT electrodes were difficult to discern because of electron scattering effects but they were estimated to be <100 nm thick

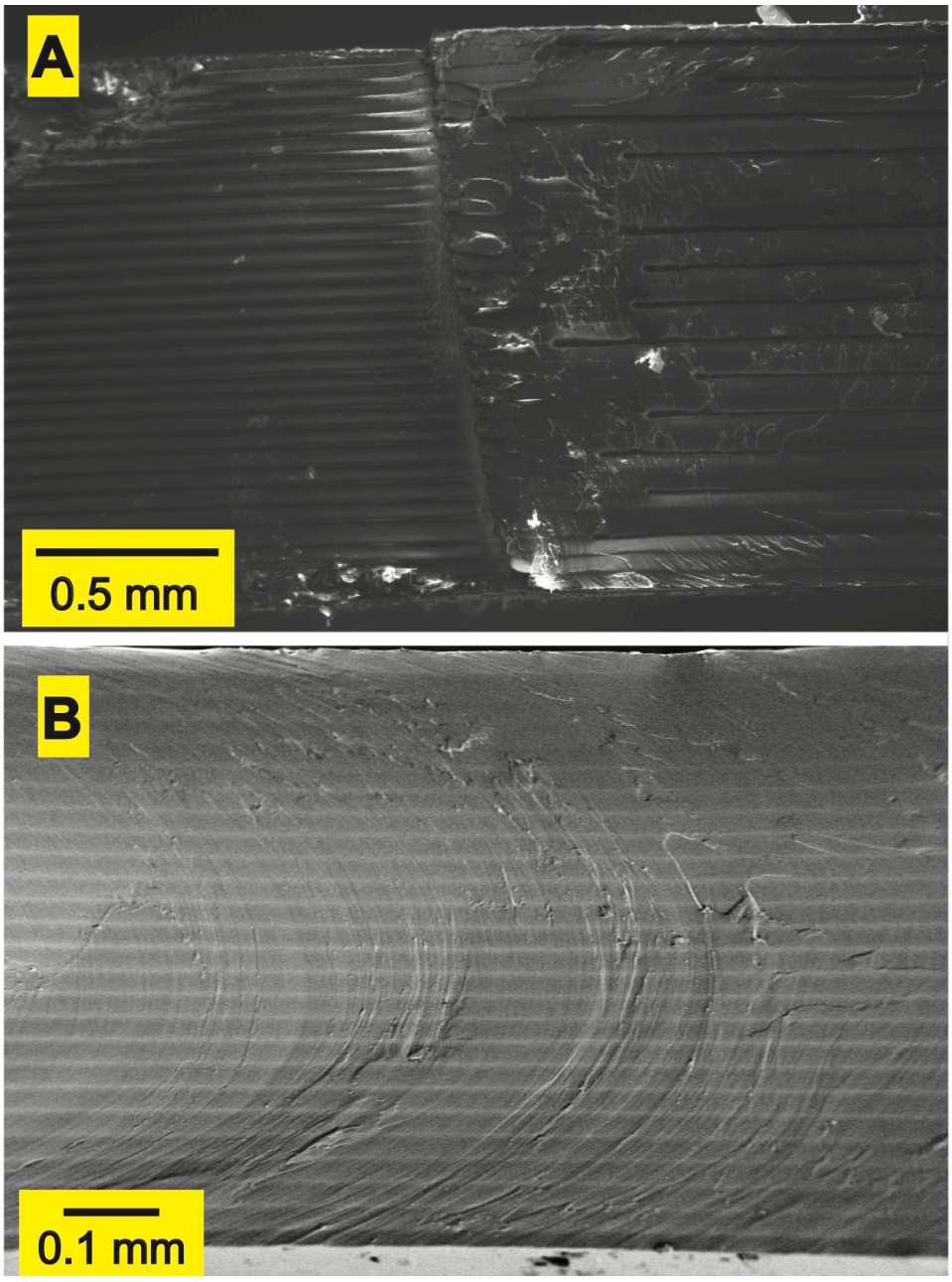


Figure 2.3: Cross section imaging of multilayers. **A**, SEM image of a disk actuator used in the fabrication of a linear contracting actuator. **B**, SEM image of a bending actuator used in the fabrication of a unimorph. The entire region corresponds to the laser cut edge of the actuator and shows each layer has a thickness of 13 μm.

2.3 Mechanical properties of multilayers

The mechanical testing was carried out using an Instron 5544A. For tensile testing, dog-bone samples conforming to the shape of the ISO 37 type IV standard were laser cut with a CO_2 60 W Versa Laser (630-680 nm, Scottsdale, AZ). The samples were stretched in uniaxial tension while measuring the force using a 10 N load cell and the change in length. The stretch, λ, is defined as the ratio of final to initial sample length. The measurements consisted of cycles of stretching to failure or stretching and returning the sample to the initial length. The maximum stretch for these cycles corresponded to 25 or 50% of initial length. This value is representative for the expected strain in an artificial muscle demonstration, since most natural muscles show linear strains of 10-30%[29].

Tensile testing of the elastomers, shown in Figure 2.4, indicated that all of them had similar nonlinear strain stiffening behavior. Elastomer B is significantly stiffer than either A or C, while C has higher elongation at failure than A. As expected, the effect of cross-linking is to increase the elastic modulus at the expense of the stretch to failure. More importantly, as shown in Figure 2.5, the stress–strain response is nearly identical for a single elastomer layer, compared to a multilayer absent any electrodes and a multilayer with CNT electrodes. The data clearly show that the presence of the electrodes in these multilayers neither increases the stiffness of the multilayers nor affects the attainable stretch to failure.

2.4 Adhesive properties of multilayers

The adhesive strengths were quantified in a pull-off test, conceptually similar to the ASTM D 4541 standard, in which the pristine PTFE layer (dimensions 60 mm $\times$ 55 mm) was pulled away from the elastomers in the perpendicular direction. To standardize the measurements, the PTFE layer was pressed into contact with the elastomer layers for 30 seconds under a 4 N compressive load. The adhesion between successively formed elastomer layers was measured

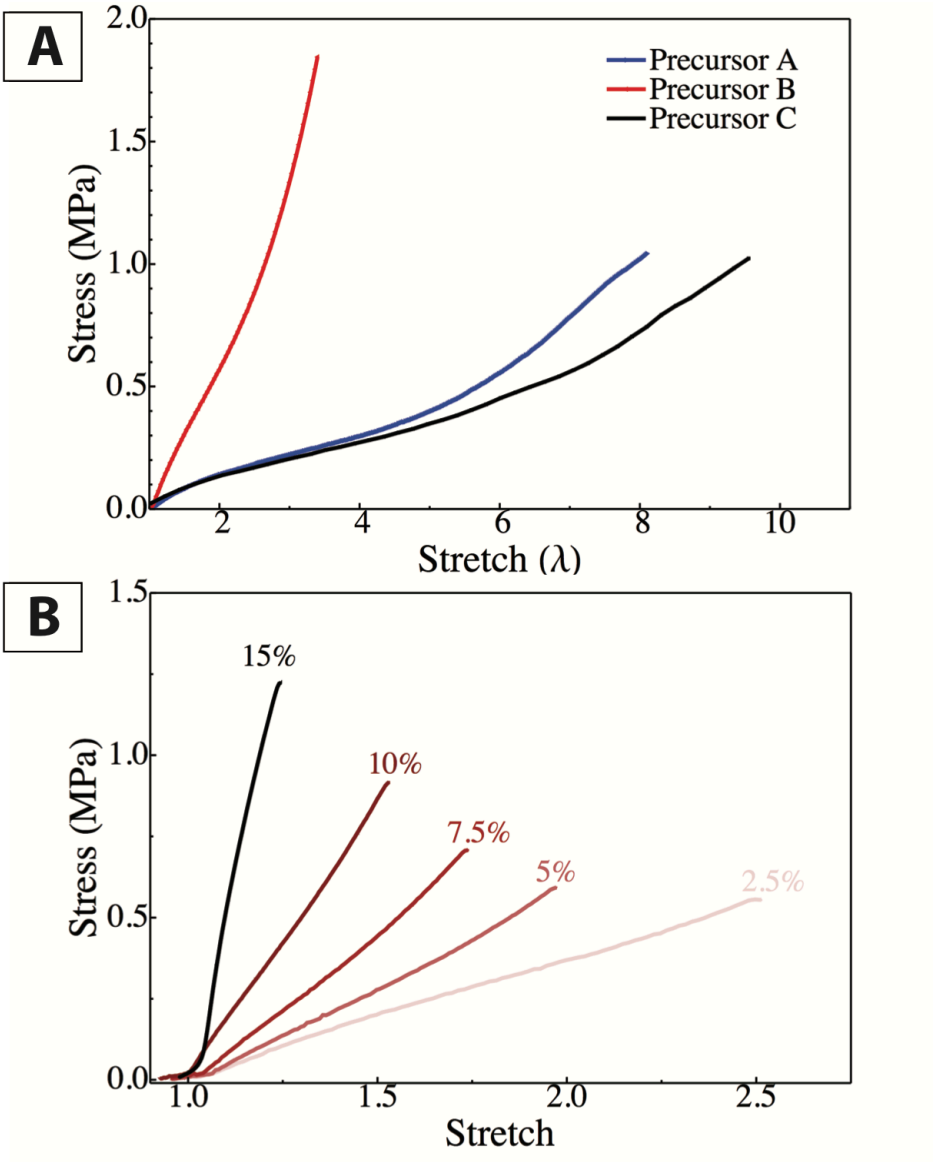


Figure 2.4: Stress vs. strain curves for pure elastomers

A, Stress vs. stretch curves for different elastomers without any HDDA cross-linker. **B**, Stress vs. stretch curves for elastomer A with the different cross-linker concentrations indicated.

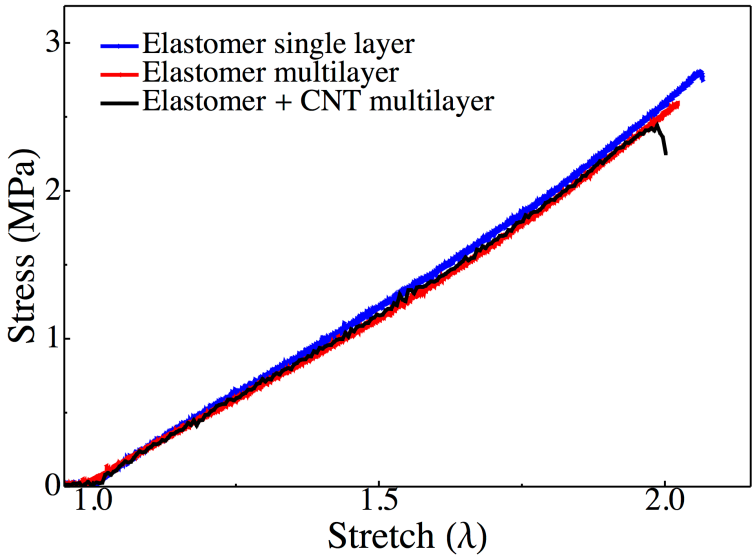


Figure 2.5: Mechanical properties of multilayers

Stress versus stretch curves for elastomer A with 10% cross-linker in three different configurations: single layer, six-layer multilayer, and six-layer multilayer with CNT embedded electrodes. The thickness of each test sample was the same (90 μm).

through a peel off test between two layers of 2 cm × 10 cm. The first layer of elastomer was coated and cured using the standard procedure. Samples three different concentrations (7.5, 15 and 22.5 mg/m^2) of CNT electrodes, as well as a control without any carbon nanotubes, were evaluated. The electrodes were directly transferred onto the first elastomer layer, then a second layer of elastomer was coated and cured on top of the electrode (or first elastomer in the case of the control test). A section of the first layer of elastomer was protected by a spacer on which the second elastomer was coated and cured. The spacer was then used to separate the two elastomer layers, connecting just the second layer to the top vise of an Instron 5544A. The bottom layer was secured perpendicular to the direction of pull. The top vise was raised until the layers were completely detached and the force was recorded throughout.

The presence of SWCNTs reduces the interlayer adhesion between successively cast elastomer films. Nevertheless, peel tests indicated the interlayer adhesion is strong, even at high nanotube loadings (22.5 mg/m^2) and for low adhesion elastomers. Furthermore, using multilayer probes, patches of conductive SWCNTs were found randomly distributed on both the separated surfaces. Other possible limitations of the fabrication method included drops in conductivity due to liquid elastomer shielding adjacent nanotubes, as well as poor bonding between elastomers through dense SWCNT networks, leading to delamination. Measurements of the electrode resistance before and after casting and curing a fresh layer of elastomer on top showed no significant changes in conductivity for the network.

Strong adhesion between the elastomer and electrode layers is an essential requirement for multilayer device fabrication. All the formulations investigated, over a range of 0–15% by mass of HDDA cross-linker, had sufficient adhesion to completely transfer CNT networks at concentrations as high as 22.5 mg/m^2. The adhesion strength, quantified using a pull-off test, was found to decrease slightly with cross-linker concentration (Figure 2.6 **A**). The most adhesive was elastomer A without any cross-linker. For this reason, it was used throughout this work as

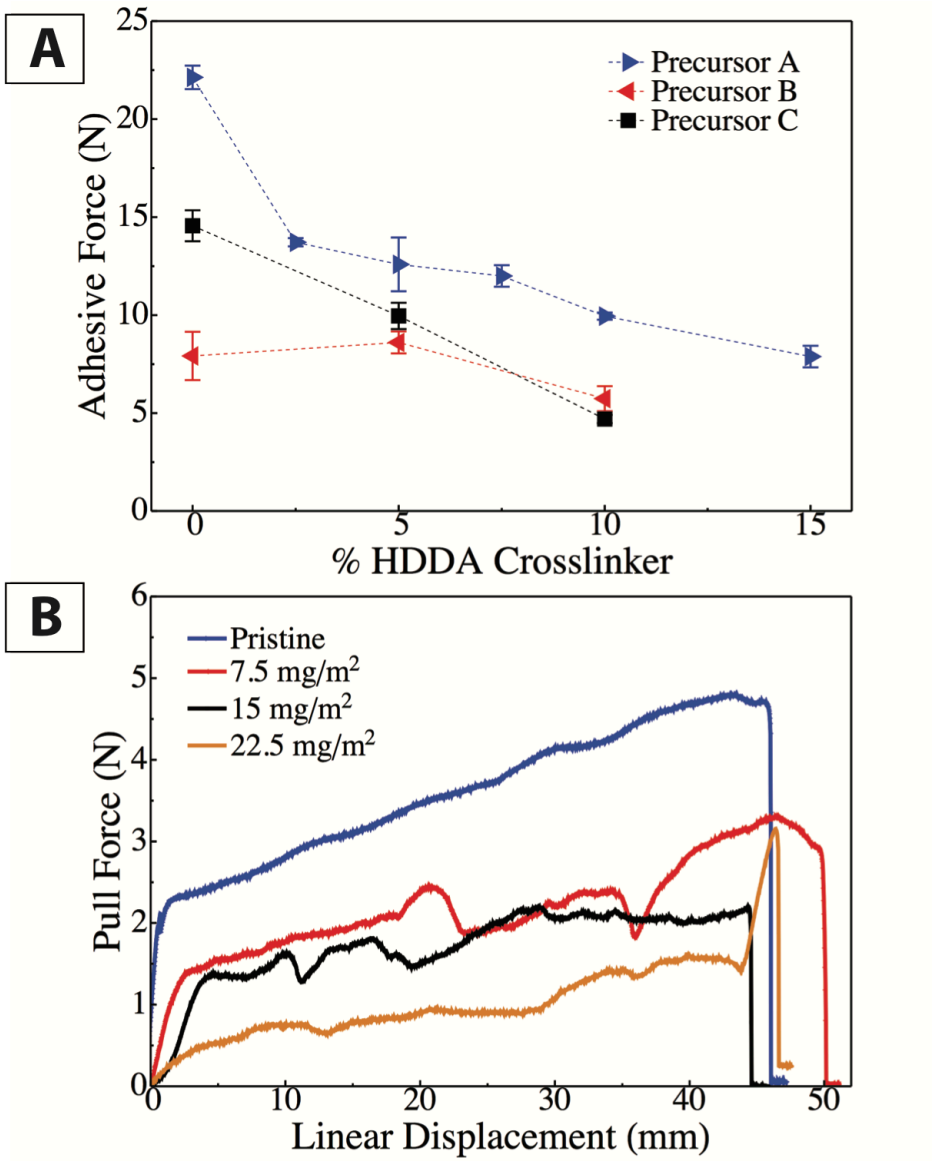


Figure 2.6: Elastomer adhesive properties

A, Adhesive force required to separate a flat sheet of polytetrafluoroethylene (PTFE) from a pristine layer of elastomer as a function of the type of oligomer and cross-linker concentration. **B**, Pull force required to separate layers of elastomer B with 10% HDDA as a function of different amounts of CNTs applied between the layers. For the layers without carbon nanotube electrodes, the second layer was formed by spin coating liquid oligomer on the UV cured elastomer. For the elastomer layers with a SWCNT electrode, the liquid oligomer was spin coated directly onto the electrode stamped on the preceding elastomer layer.

the base for building multilayers by spin coating on a polyethylene terephthalate glycol (PETG) support wafer. The presence of the CNT electrodes decreased the adhesive strength between the elastomer layers as the concentration of the CNT increased (Figure 2.6 **B**) but no delamination was observed in any of the unimorph tests. Furthermore, the adhesive failure always occurred within the elastomer impregnated CNT layer, leaving CNT on both of the separated surfaces.

2.5 Electrical properties of CNTs on elastomers

The electrode resistance of the electrodes as a function of strain was evaluated using a four-point probe in contact with the electrode material. The probe consisted of four equally spaced (3 mm), spring loaded metal probes. During the measurement, a DC current was applied on the outer probes from a Keithley 6221 AC and DC current source, and the voltage was measured across the inner probes using a Keithley 2701 Ethernet Multimeter. The electrode on the elastomer was stretched uniaxially and the resistance was measured at 5 or 10% increments of initial length until the sample failed or the resistance became too high to measure. The results are summarized in Figure S2 and show that the conductivity increases with larger amounts of SWCNTs. For repeated electrical actuation, the electrode conductivity needs to have minimal variation after stretch and release. Low variation in resistance as a function of stretch was observed for electrodes based on elastomer B with 0% HDDA (15 mg/m^2) and elastomer C with 0% HDDA (22.5 mg/m^2 CNTs) (Figure 2.7). Although only one cycle is shown, the small change (<5% on average) in resistance indicated that the network returns to its original conductive state after strain and release.

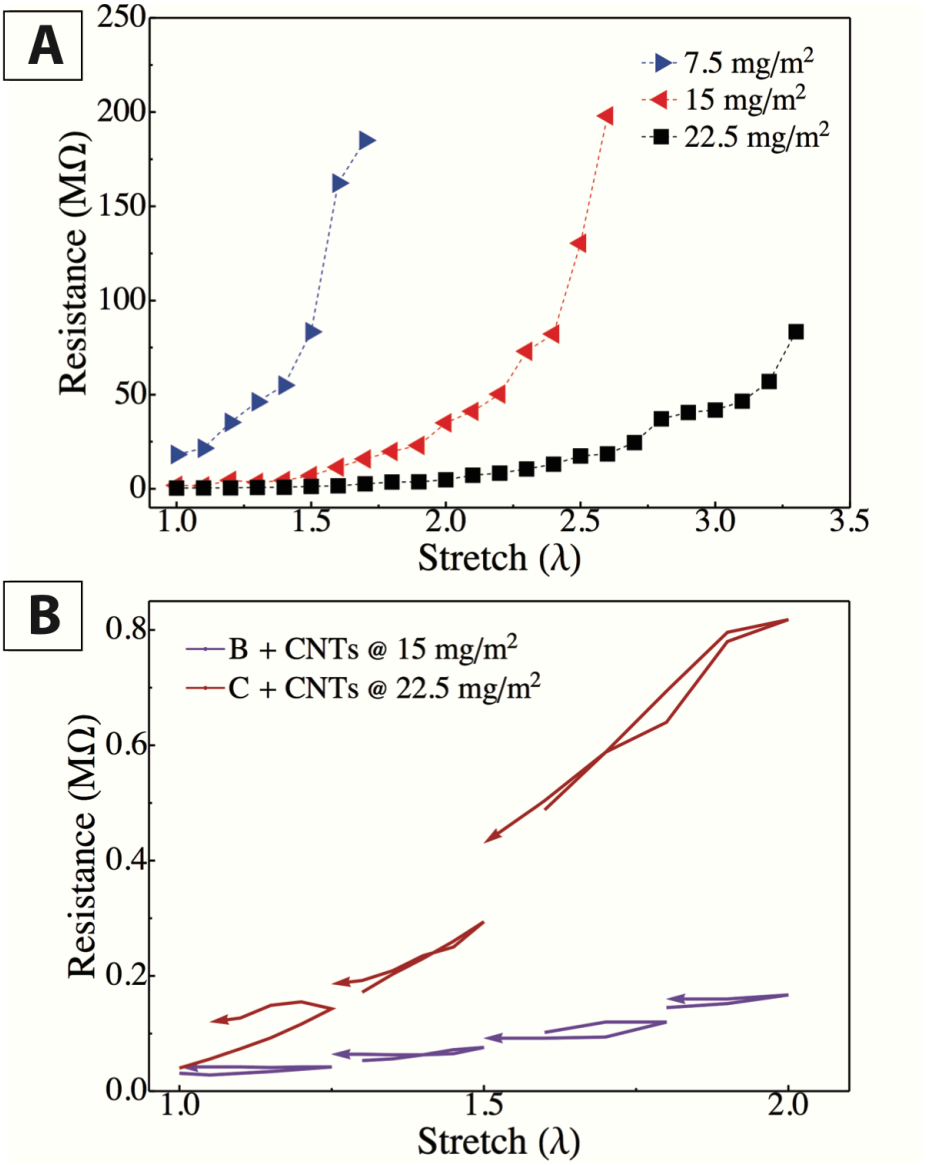


Figure 2.7: Sheet resistance of CNTs on elastomers under strain
A, Sheet resistance as a function of stretch for elastomer A with 0% HDDA at the three CNT densities indicated. **B**, Sheet resistance as a function of stretch for elastomer B, with 0% HDDA (using 15 mg/m² CNT) and elastomer C with 0% HDDA (using 22.5 mg/m² CNT). The materials were stretched in 25% or 50% increments of their initial length, then returned to evaluate if conductivity was regained. The last point in each stretching loop is indicated by an arrow to guide the eye.

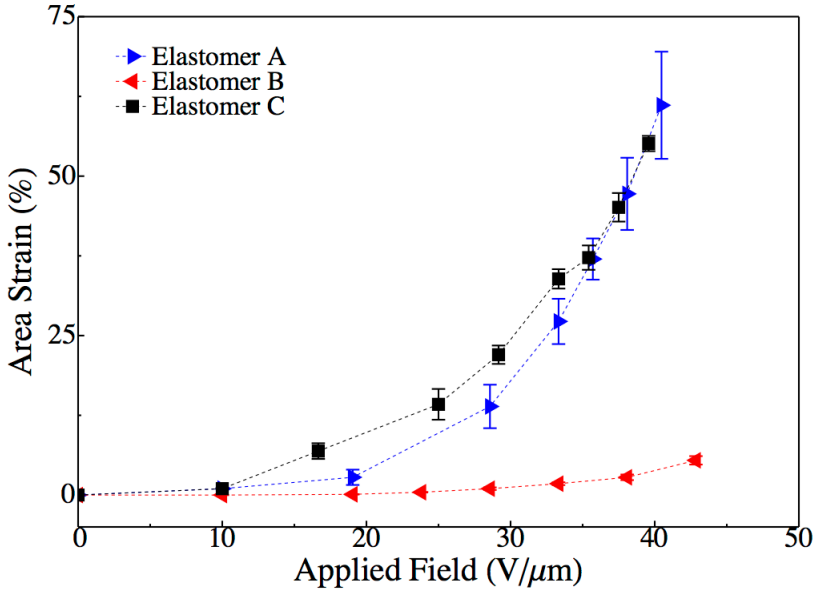


Figure 2.8: Actuation without pre-strain
Area strain for the non-prestretched elastomers with 0% HDDA cross-linker as a function of applied electric field.

2.6 Actuation performance of multilayers

As mentioned earlier, the work of Niu et al. showed that voltage-controlled actuation of elastomer A could be achieved without prestretching. We have found that all three of the elastomers studied also show actuation without prestretching. The results, obtained under biaxial conditions for single layer actuators, are shown in Figure 2.8.

To evaluate the actuation performance of the multilayers in a unimorph configuration, measurements were made of the blocked force (F_b), the free-end displacement (d), and the actuator bandwidth of unimorphs all having the same dimensions (20 mm long and 5 mm wide). The energy density of the actuators

was estimated as $u_e = F_b \times d/2m$, where F_b is the blocked force, d is the displacement, and m is the mass of the actuator. Similarly, the power density was estimated as the product of the energy density and the actuator bandwidth. The three different elastomers with 10% cross-linker were each made into 12 layer unimorphs consisting of individual layers each 30 μm thick. At low frequencies, the end displacement was independent of frequency but at higher frequencies, the peak-to-peak end displacement decreased. The frequency at which the peak-to-peak displacement decreased below 80% of the 0.1 Hz displacement was identified as the maximum bandwidth of the actuator. A more detailed model was later developed[49], and captures the behavior as a heavily damped system due to the high tangent δ of the acrylic elastomers.

Elastomers made with elastomer A had the highest energy density, while B and C had significantly higher bandwidths, and therefore higher power densities (Table 1). The specific dependence of displacement on actuation frequency is shown in Figure 2.9 **A**. From measurements of the electrical current during actuation, the time to charge each of the multilayers was found to be similar, being in the 1–10 ms range, suggesting that the bandwidth differences were due to different viscoelastic responses of the elastomers rather than being an electrical time constant for the RC circuit containing of a resistor (R) and a capacitor (C). The resistance is a combination of series resistance of the electrodes, and leakage through the dielectric. In addition, measurements of elastomer tan δ (made using a Bose ElectroForce 3200 Electromechanical Tester) confirmed that the higher power elastomers had correspondingly smaller viscoelastic losses (Figure 2.9 **B**).

A simple model can be used to explain the relative performance of cantilever beams made with the three different elastomers. Since the cantilevers supported at one end, and are made from viscoelastic materials, we expect a damped cantilever beam behavior, where the natural frequencies are given by:

$$f_{res} = \frac{1}{2\pi}\sqrt{\frac{\lambda_n^4}{L^4}\frac{EI}{\rho A}} \tag{2.1}$$

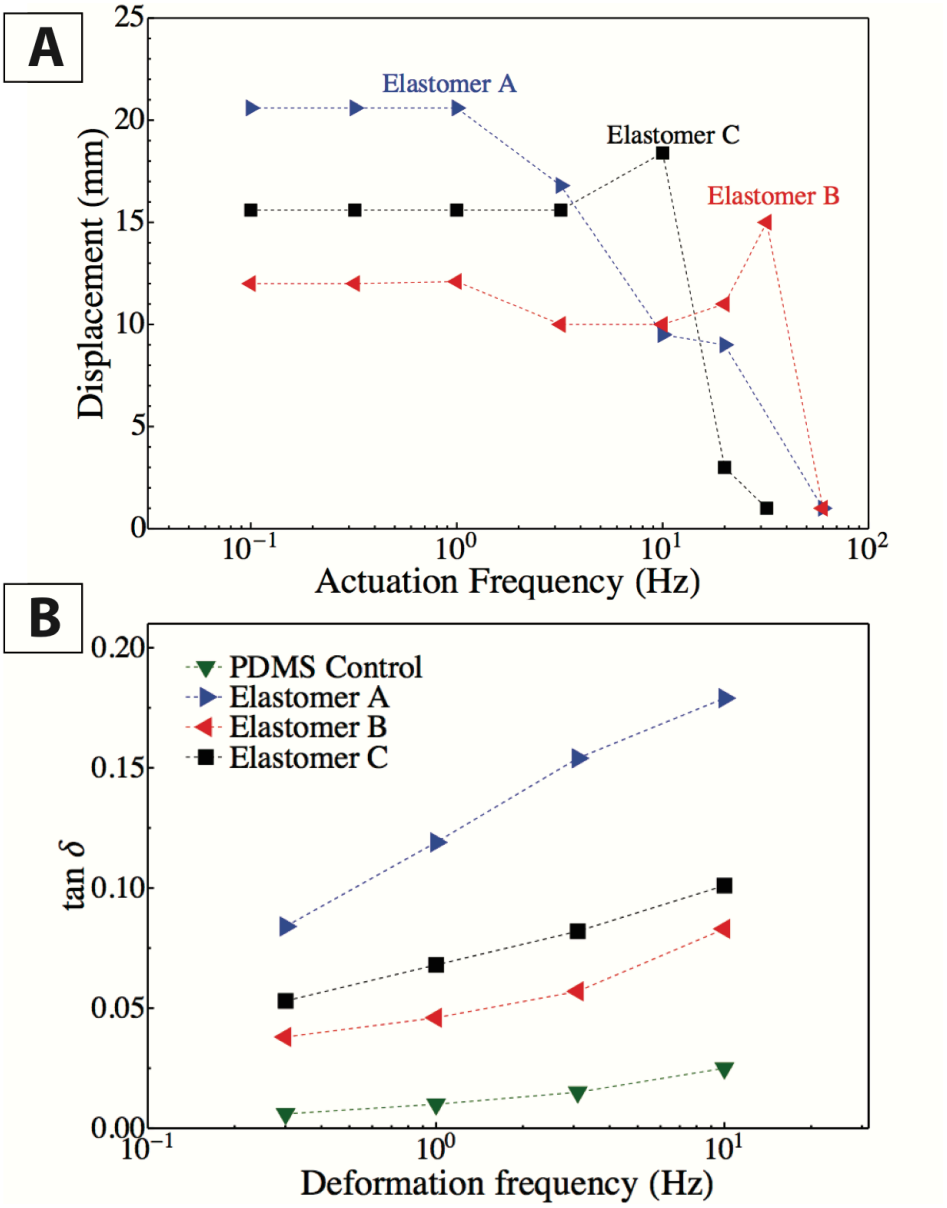


Figure 2.9: Actuator bandwidth and viscoelasticity of elastomers
A, End displacement of the unimorph as a function of frequency when actuated at 4 kV. **B**, Tangent δ for the pure elastomers made with oligomers A, B, and C, compared to a silicone control (Sylgard 184, 10:1 ratio oligomer to crosslinker).

Table 2.1: Unimorph[1] characterization results.

Elastomer type	Blocked force [mN]	Maximum displacement [mm]	Maximum bandwidth [Hz]	Energy density [J/kg]	Power density [W/kg]
A	16.9±1.0	12.0±0.3	1	2.04±0.12	2.04±0.12
B	12.5±0.9	15.6±0.4	10	1.95±0.10	19.5±1.01
C	11.1±0.6	12.6±0.4	30	1.42±0.08	42.6±2.42

[1] For each elastomer, three unimorphs were tested, each for five consecutive tests. Each unimorph consisted of 12 layers of 40 μm each. The unimorph length was 20 mm, and the width was 5 mm. The fastest actuator for each elastomer type was used to determine the resonant frequency.

where λ_n^4 is a constant, L is the length of the cantilever, E is the Young's modulus of the elastomer, I is the area moment of inertia of the beam, ρ is the density of the elastomer, and A is the beam cross-sectional area.

Accounting for damping effects, the damped resonant frequency of the beam can be found from

$$f_{damped} = f_{res}\sqrt{1-\zeta^2} \tag{2.2}$$

where ζ depends linearly on the $tan\delta$ of the elastomer. Given the decrease in $tan\delta$ from elastomer B, to C, to A (as seen in Figure 2.9 B), we expect the inverse trend of increasing damped actuator resonant frequency as exhibited in Figure 2.9 A. This simple model can also be useful in comparing amplitude and frequency of actuation for simple robots made from cantilever beams, as will be described in Chapter 3.

2.7 Low voltage actuation

Having demonstrated linear contraction and expansion, we modified the multilayering process to make bending actuators. In this demonstration we were also able to significantly lower the actuation voltage to below 800 V. One of the

major integration challenges for dielectric elastomer actuators has been the need for high voltage sources (>1 kV), which are usually large, heavy, and inefficient. Our goal was proof of actuator performance in the voltage range accessible to miniature power supplies[50, 51] (<600 V) that can be more easily integrated with other imperceptible electronics[52]. To reach both the deformation mode and actuation voltage goals we made bending actuators with thinner layers (13 μm each) and measured the tip displacement when actuated at a range of frequencies below 800 V. A 2 cm long beam, 30 layer actuator showed tip displacements comparable to its length at 600 V. When applying 600 V at increasing frequencies between 1 and 20 Hz we observed a peak in tip displacement (Figure 2.10 **A**), as expected, at resonance of the bending beam. When applying a 10 Hz signal at increasing voltages between 100 and 800 V, we observed an increase followed by saturation of the tip displacement (Figure 2.10 **B**), as expected in a clamped-free cantilever.

2.8 Multimorph demonstration

The fabrication method also enabled us to devise more complex, and programmable, motions into a single device. A multimorph actuator was made as shown in Figure 2.11: the power electrode was separated into two segments, as was the ground electrode. By rotating the power electrodes by 90° relative to the ground electrodes it was possible to create four zones that could be actuated independently. In this fashion, we created a multimorph actuator capable of nine different deformation modes when different electrodes were powered. The multiple degrees of freedom were built in by controlling the geometries and electrical connection paths of each of the four electrodes. While the multimorph presented is quite basic, the principle behind it can be used to create much more complex motion, beyond traditional DEA architectures.

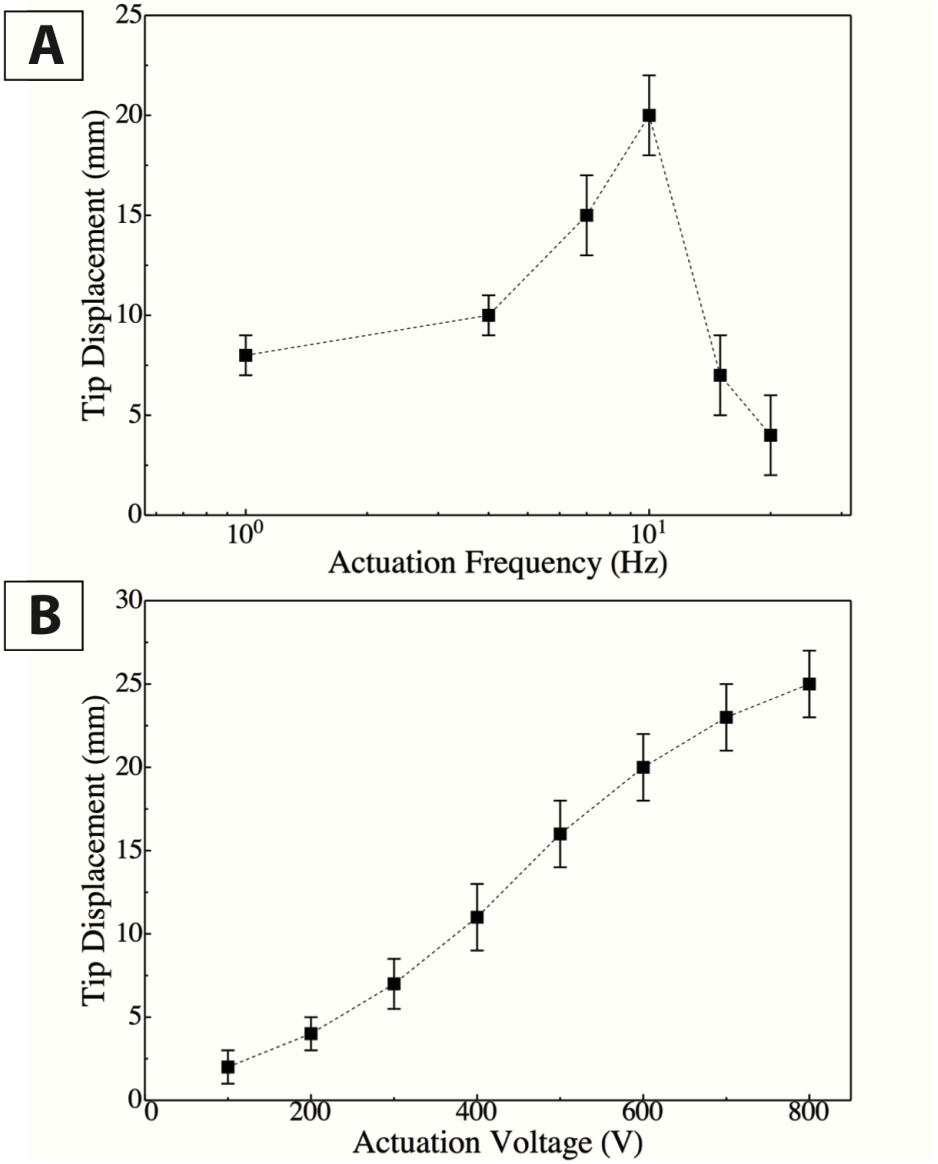


Figure 2.10: Low voltage actuation

A, Tip displacement of a unimorph bending actuator which incorporates rigid beams to control deformation in a single direction at 600 V as a function of actuation frequency. **B,** Tip displacement at 10 Hz as a function of applied voltage. Both sets of results indicate actuators can be powered at low voltage, by lightweight, small footprint power supplies. The resonance does not change as a function of the applied electric field, suggesting the motion is limited by the viscoelasticity of the elastomer, not the RC constant of the circuit.

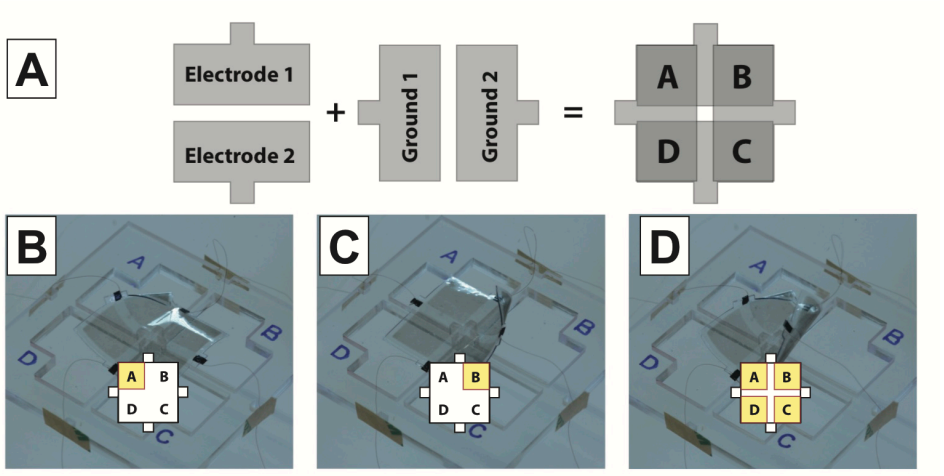


Figure 2.11: Multimorph demonstration

A, Schematic of electrode patterns used to make a simple 2 × 2 multimorph actuator. **B**, Photograph of an eight layer, elastomer A with 10% HDDA multilayer unimorph with voltage applied to segment A, **C** voltage applied to segment B, and **D** voltage applied to all segments. Actuation voltages are 3.75 kV.

2.9 Summary

In this chapter we have demonstrated that the performance of DEAs (maximum strain, energy density, and actuator bandwidth) can be tuned by controlling both the choice of elastomer precursor and the cross-linker concentration. The cross-linking concentration increased the stiffness, reduced the maximum elongation before failure, and decreased the adhesive strength of the elastomers. The Young's modulus for elastomer B without any HDDA cross-linker (0.66 MPa) was almost an order or magnitude higher than elastomer A (0.1 MPa). Meanwhile, precursor C had similar stiffness, but slightly larger extension range, without being as adhesive. Between the three precursors and the ability to vary cross-linker density, the range of mechanical properties for acrylic elastomers that actuate without prestretch is greatly expanded. The unimorph actuator testing revealed that the novel oligomers, elastomers B and C, offered additional advantages over previous compositions. The increase in resonant frequency from

1 (for A) to 30 Hz (for B) confirmed that tailoring the material composition could overcome some of the known drawbacks of acrylic elastomers such as slow actuation speed[53]. The energy densities were comparable to other multilayer geometries[23], but the power densities reported here broaden the range of potential applications.

The combination of liquid acrylic oligomers, UV curing, and the intrinsic adhesiveness of the acrylics together with standard spin coating, patterning, and dry transfer of CNT by stamping enables the fabrication of multilayer dielectric elastomer devices. This is exemplified in this work by the fabrication of multilayer unimorphs. The significance of this work is that the combination of materials and processing enables two of the current technical limitations of DEAs to be overcome. Specifically, the compositions studied remove the requirement that the elastomer has to be prestretched. The use of a liquid precursor that can be UV cured after each layer enables thinner elastomer layers to be obtained, decreasing the voltage required for actuation. The thickness of the individual layers can be determined by control of the spin coating process and the viscosity of the liquid. Thinner CNT electrodes decrease the effective electrode stiffness that, in turn, increases the attainable actuation strain for a given applied voltage. The natural adhesion of the acrylics increases the reliability of the stamping of the CNT as well as adhesion to a wider range of substrate materials.

Furthermore, the ability to create the electrodes by stamping (or spraying) facilitates patterning of the electrode geometries, including doing so at different positions in the multilayer structure. Unimorphs fabricated exhibit similar blocked forces and energy densities as have been reported but at lower actuation voltages. A simple 2D actuator is demonstrated illustrating the potential of electrode patterning. Overall the process can be tuned to fabricate versatile devices, in which the number, thickness, planar geometry, electrode coupling, and chemical nature of the layers can be manipulated to design actuators for specific applications. The multimorph actuator highlights a novel approach to creating smart programmable materials capable of multiple degrees of freedom from limited inputs. Beyond improving DEAs, we consider the combination of

acrylic elastomers and stretchable carbon nanotube network electrodes to be a materials platform technology, applicable to other areas, such as stretchable sensors, soft sensor-actuator combinations, soft electroadhesives[54] to name a few.

3

Optimized carbon nanotube electrodes for high energy density actuators

A fundamental challenge in developing soft robots, is the creation of effective actuators to deform a soft body to achieve locomotion, manipulation, or other tasks[6, 55]. The gold standard for actuation in a soft body is natural muscle[56], which exhibit high energy density (0.4-40 J/kg), a broad range of frequencies (1-200 Hz), and large strains (5-30%). In this chapter we realize a long standing vision for DEAs as fully soft, electrically driven, energy dense artificial muscles (Fig. 1 A,B). Single film dielectric elastomers are usually thin, to minimize the actuation voltage, which leads to small force outputs ($<$10 mN) and limited applications. To reach both the desired forces ($>$10 N) and displacements ($>$1 cm), we need to stack multiple layers.

Here we build upon the work from Chapter 2 which combined UV curable strain stiffening elastomers[38] with ultra-thin carbon nanotube (CNT) based electrodes[57] to make multilayered, robust, completely soft actuators. The use of strain-stiffening elastomers in a multilayered configuration bypasses the need to prestretch the elastomer[58], which otherwise negates the advantages of a soft actuator by surrounding it with a rigid frame. Without stiff constraints, DEAs can be made into linear contracting and expanding actuators[59] to mimic the function natural muscle fibers[60] and muscular hydrostats[61], respectively. These linear actuators also serve as simple, yet reliable tools to measure mechanical deformation, and therefore quantify energy density, as well as other physical and electrical properties. The range of strains across different animal muscle types is fairly constant (5-10%), but power and energy densities depend on the type of locomotion[29]. For example, the energy density ranges from 0.4 J/kg for a swimming bass at 4 Hz, to 6 J/kg at 25 Hz for the flight muscles in a locust, to 40 J/kg for a running rat at 7.5 Hz[62–64]. With the goal of dielectric elastomer artificial muscles that achieve similar energy densities and bandwidths as natural muscles, we aimed for the following combination of actuator capabilities: (i) demonstrate linear contraction or expansion in fully soft DEAs, (ii) match the strain capability and energy density of natural muscle, and (iii) maximize the speed of deformation to reach the viscoelastic limits of the elastomer material.

To achieve these goals, we optimized the electrode composition and multilayer processing to sustain high applied electric fields, without the onset of destructive dielectric breakdown. To understand this motivation in quantitative terms, for small deformations, on par with the strains observed in natural muscles ($<$20%), the strain in a linear DEA can be approximated as $s = \varepsilon E^2/Y$, where ε is the permittivity of the elastomer, Y is the Young's modulus of the elastomer and E is the applied electric field. The elastomers used in this work exhibit linear behavior in the range of strains of interest, as demonstrated earlier[57]. To a first order, the elastic energy density of the deformed elastomer can be approximated as $U_e = s^2Y/2$ leading to $U_e = \varepsilon^2E^4/2Y$, meaning energy density is highly

sensitive to the applied electric field. In addition, we desire thin electrodes, to maximize the volume occupied by the elastomer in the final device.

Carbon nanotubes meet the requirement for high conductivity at low thickness[41, 45], and could be easily integrated into a multilayer actuator. Other electrode materials considered were too thick (e.g., hydrogels[65], ionogels[66, 67]), insufficiently conductive (e.g., crumpled graphene[68]), or difficult to integrate in a multilayered actuator (e.g., crumpled metal[69]). The main drawback of carbon nanotubes is the early onset of dielectric breakdown[44] compared to more conventional electrodes, such as carbon grease. Earlier work[70] showed that dielectric breakdown occurs at low strains ($<20\%$), before the onset of strain stiffening in the elastomer. We hypothesized that the reason for early dielectric breakdown is due to an excess of carbon nanotubes causing high electric field concentrations at the nanotube ends. Based on this hypothesis, we studied the relationship between CNT areal density and onset of dielectric breakdown.

Lower areal densities of carbon nanotubes in the electrodes may increase the sheet resistance, which in turn increases the actuator RC time constant. The response speed of DEAs is limited either by how quickly the compliant capacitor is charged, or by how rapidly the elastomer can deform in response to the generated Maxwell stress between the electrodes. We aimed to find electrodes with sufficiently low sheet resistance such that the deformation was limited by the elastomer viscoelasticity. As a result, the key actuator performance metrics (i.e., energy density and bandwidth) could be systematically varied by tuning different material properties (i.e., breakdown field and elastomer viscoelasticity, respectively).

3.1 Experimental methods

The multilayering method was adapted from our earlier work[57]. We used the Gent model[71] to select which elastomer formulation to use in our multilayers. The model takes into account the strain hardening behavior of elastomers. In the

Gent model, the strain energy density function is given by

$$W = -\frac{\mu J_m}{2} ln\left(1 - \frac{I_1 - 3}{J_m}\right) \tag{3.1}$$

where μ is the shear modulus of the elastomer and $J_m = I_m - 3$. The I value corresponds to the first invariant of deformation tensor at which the strain hardening occurs. The dielectric elastomer must undergo rapid strain stiffening to avoid the electromechanical instability[36]. For the Gent model, strain stiffening occurs in materials with I values lower than seven in the model parameter fit. In order to obtain large actuation strain, we searched through different oligomers and crosslinker concentrations for the elastomer with the lowest modulus that could demonstrate the desired strain stiffening behavior. The elastomer of choice used CN9018 as the oligomer base with 5% hexanediol diacrylate (HDDA) crosslinker, with parametric model fits of I=6.97, and μ=207.4 kPa. On one occasion we made elastomers with different crosslinker concentrations (0, 5, 7.5, 10, and 12.5% HDDA) to increase the Young's modulus of the elastomer (50, 200, 300, 450, and 660 kPa, respectively), to evaluate the onset of dielectric breakdown as a function of elastomer stiffness. The electrodes were made using carbon nanotube (CNT) inks A of P3 carboxylic acid-functionalized CNTs from Carbon Solutions Inc. (Riverside, CA) and ink B of surfactant-coated CNTs from NanoC (Westwood, MA). The P3 CNTs were received as powders and suspended in water by ultrasonication (10 minutes at 65% amplitude using an ultrasonic horn, Cole Parmer 500 W Processor, Vernon Hill, IL). All inks were diluted to to 17% transmittance at 550 nm (measured in a 1 cm cuvette using a USB2000+ spectrometer from Ocean Optics, Largo, FL) and used as prepared. The diluted inks were mixed with isopropanol then filtered through polytetrafluoroethylene (PTFE) filters (9.62 cm^2, 0.2 μm pore diameter from Spectrum, New Brunswick, NJ). The electrode sheet resistance was measured using an Inline Non-contact Sheet Resistance Meter Model 20J3 (Delcom Instruments, Prescott, WI).

Every device was made with two inactive outer layers to avoid dielectric

breakdown from exposed electrodes. The complete multilayer was laser cut to incorporate a 1 mm passive edge and peeled off the PETG wafer. For contraction actuators, multiple disks (between 5 and 50, depending on the experiment) were stacked on top of each other perpendicular to the electrode plane. Passive tension elements (rubber bands) were added on 3D printed connection elements to keep the stack under compression and avoid delamination under large forces. There were no observable differences between the displacement of the actuators powered to high voltage with or without tension elements. For expanding actuators the multilayer rectangle was rolled along the longer edge to create a roll. Electrical connections were made by cutting the multilayer to expose the electrodes. Colloidal silver (Ted Pella, Redding, CA) was applied to the exposed nanoconductors, then carbon tape (also Ted Pella) covered the silver and connected to wires leading to a high voltage power supply.

Mechanical properties of the materials are determined following previously established guidelines[46]. The dielectric breakdown limit of disk actuators was determined by powering the devices using a Trek 610E power supply and amplifier (Lockport, NY). The current limit was set to 2 mA and voltage was applied as a step function of increasing amplitude, starting at 1 kV and increasing in 0.25 kV increments until breakdown was observed. Additionally, the linear actuators were used to determine the current and displacement responses during early testing at high voltages. The linear expanding actuators were secured at the bottom of the roll and powered using the high voltage power supply. The current at the power supply was recorded and the upward displacement was measured using an MTI 2100 Fotonic Sensor (MTI Instruments, Albany, NY). Similarly, the blocked force was measured using a Nano 17 load cell (ATI, Apex, NC) load cell mounted above the actuator. Linear contracting actuators were characterized in an Instron force tester (Norwood, MA). The pull force was measured for a clamped actuator, powered to high voltage. The bending hydrostat actuators were powered using the high voltage power supply and imaged using a Nikon camera. The photographs were analyzed using image processing software (imageJ) to determine tip displacement.

Electrodes were imaged using an Ultra 55 Scanning Electron Microscope (Zeiss, Oberkochen, Germany). The electrodes were transferred from the PTFE filters onto carbon tape (Electron Microscopy Sciences, Hatfield, PA). The micrographs were analyzed using imaging processing software (imageJ) to obtain numerical data for area coverage. Photographs and supporting videos are acquired with a digital DSLR camera (Nikon D7500, Nikon Corp, Japan). Video sequences are clipped from raw footage and exported using iMovie (Apple Corp, Cupertino, CA, USA).

3.2 Electrode composition impact on dielectric breakdown

To test the hypothesis that breakdown field depends on nanotube areal density, we fabricated multilayered disk actuators with different CNT areal densities, and measured the dielectric breakdown field in each. A schematic of a disk actuator and the multilayering procedure is shown in Fig. 2.2. The disk actuators were made by repeated spin coating and UV curing of acrylic elastomer precursors, alternating with stamping of electrodes from a supporting carrier film. The electrodes were made by filtering water-based CNT inks, diluted with isopropanol, through polytetrafluoroethylene (PTFE) filters, used as carrier films. We kept constant the area of the filter (9.62 cm^2) and ink concentration (determined by optical transmittance to be 17% at 550 nm). To systematically modify the CNT areal density, we varied the amount of ink used (50-600 μL), leading to areal densities ranging from 5.19 to 62.37 $\mu L/cm^2$. We used two different inks: 'A' contained functionalized CNTs dispersed in water (average diameter = 5 nm), while 'B' contained surfactant-coated CNTs dispersed in water (average diameter = 10 nm). The surfactants used for the stable dispersion of purified CNT in ink B at high concentrations in water can be removed at low temperatures by a heating process (2 hours at 120° C), post deposition. The multilayering fabrication process allowed for the electrodes to be heated while on the PTFE carrier films, thus eliminating the need to expose the elastomer to high

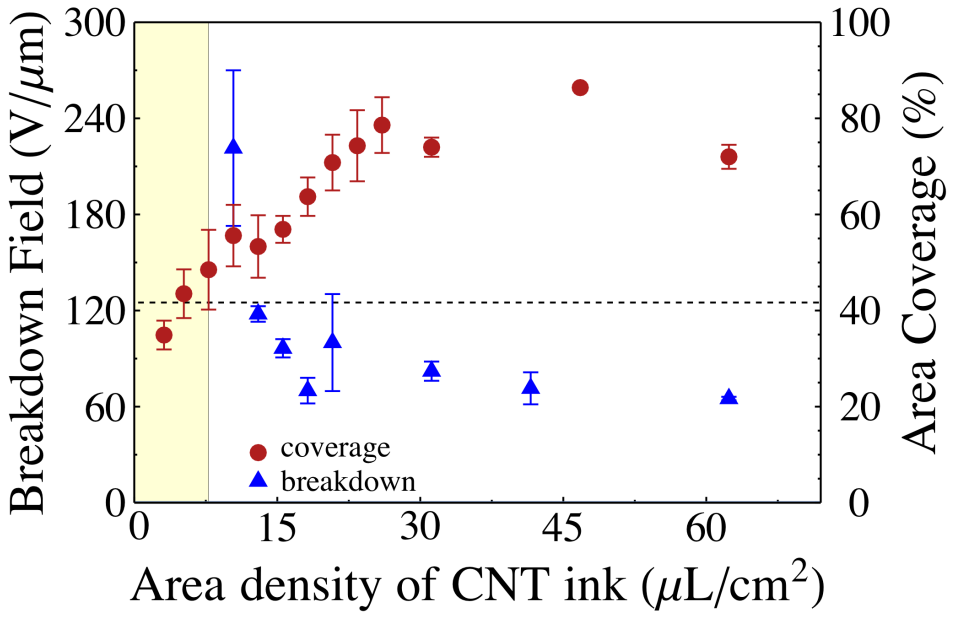


Figure 3.1: Breakdown fields vs. area coverage

(left y-axis) Breakdown field of the disk actuator as a function of areal density of ink A used. (right y-axis) Estimated area coverage of carbon nanotubes as a function of the areal density of ink used, based on SEM imaging. The results indicate that lower areal densities of CNTs reduce the chance of dielectric breakdown. The shaded region left of the 9 μL/cm^2 mark indicates no deformation was observed at any applied field. Dashed line corresponds to the breakdown field when using conventional carbon grease as an electrode determined in house.

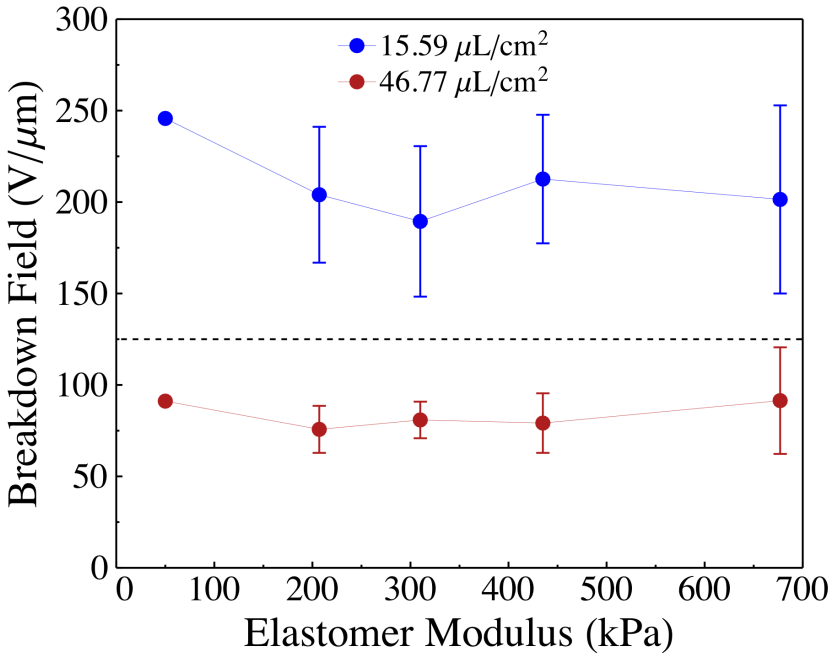


Figure 3.2: Breakdown fields vs. elastomer modulus
Breakdown field as a function of elastomer Young's modulus, at two different CNT areal densities, for electrodes made with ink A. The results indicate that the areal density of CNTs dictates the onset of dielectric breakdown, and not the elastomer stiffness.

temperatures. The actuators made with the two inks at varied amounts were tested at increasing electrical fields until dielectric breakdown occurred.

The results showed that, for both inks, there is a desirable, low CNT areal density region (7.79-15.59 μL/cm^2) in which the breakdown occurs at high electric fields. Reducing the areal density of CNTs increased the dielectric breakdown field to levels higher than more conventional carbon grease electrodes (Fig. 3.1). Similar effects were observed for both types of ink used. The onset of

dielectric breakdown was found to be approximately inversely dependent with the area coverage. Scanning electron microscopy (SEM) of the CNTs as dispersed on PTFE filters (Fig. 3.3) showed that as the areal coverage of the electrode increases from 30% at an areal density of 5.59 μL/cm^2 to around 70-90% above 20.79 μL/cm^2. However, the electrodes are not homogenous: patches of dense carbon nanotubes form around 10.39 μL/cm^2, while some regions remain almost free of CNTs. To our surprise, increasing the elastomer modulus by a factor of 10$\times$ (through additional crosslinker in the elastomer precursor), did not impact the likelihood of breakdown as much as increasing the areal density of CNTs by a factor of 3$\times$ (Fig. 3.2). SEM imaging of the electrodes on the transfer PTFE films show that the non-homogeneity may be due to aggregation at the filter pores (Fig. 3.4 A and C). The microstructure is retained after the electrode is transferred onto the elastomer (Fig. 3.4 B and D). Overall, the results indicate that the process gives control over the areal density of the CNTs, which in turn allows the actuators to be powered to higher electric fields than previously demonstrated.

3.3 Ink selection process

Although a low areal density of CNT electrodes reduces the likelihood of early breakdown, this can lead to poor electromechanical performance due to a low area coverage of the elastomers. To quantify the effect of CNT areal density on mechanical performance, we built roll actuators[49] and measured their linear displacement in the axial direction (Fig. 3.5). The expanding actuator consisted of fifteen layers of elastomer (6 cm $\times$ 1 cm), and electrodes with both low (15.59 μL/cm^2) and high (46.77 μL/cm^2) areal densities of ink B. The actuators were tested by applying increasing voltage steps, while measuring the actuator displacement and current drawn. In the initial test to 2 kV, the higher areal density electrodes drew higher currents than the low areal density electrodes (Fig. 3.6 A-C), while showing smaller displacements. In the subsequent test, the

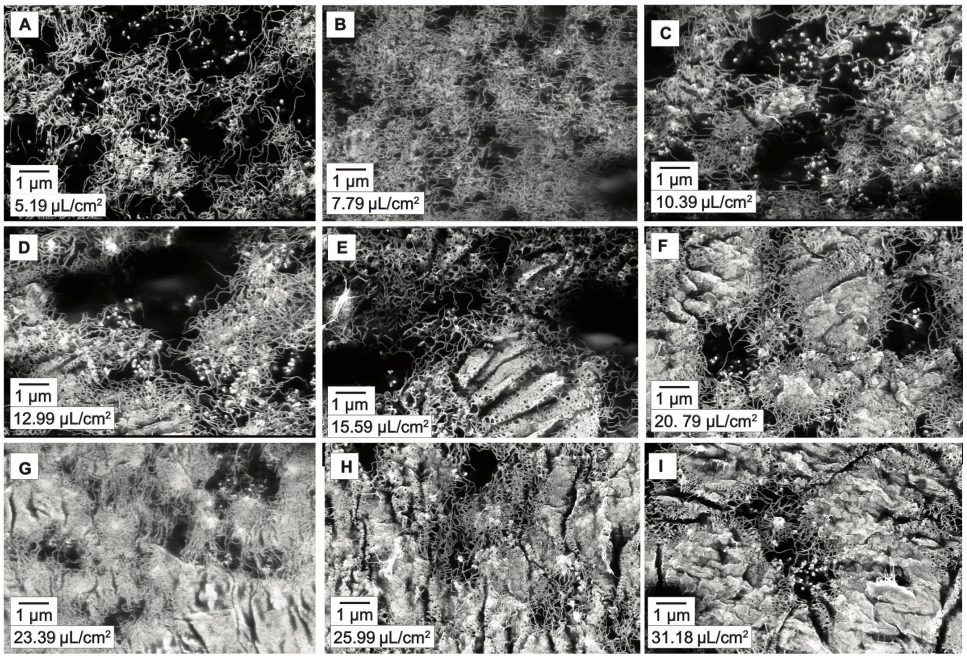


Figure 3.3: Scanning electron microscope images of electrodes
A-I, SEM images of ink B CNTs transferred onto carbon tape directly from PTFE filter (without any thermal treatment), with areal densities labeled for each. The lighter regions correspond to carbon nanotubes and show that dense patches of CNTs form at loadings higher than 15.59 μL/cm², which may correspond to localized high field areas that cause early dielectric breakdown.

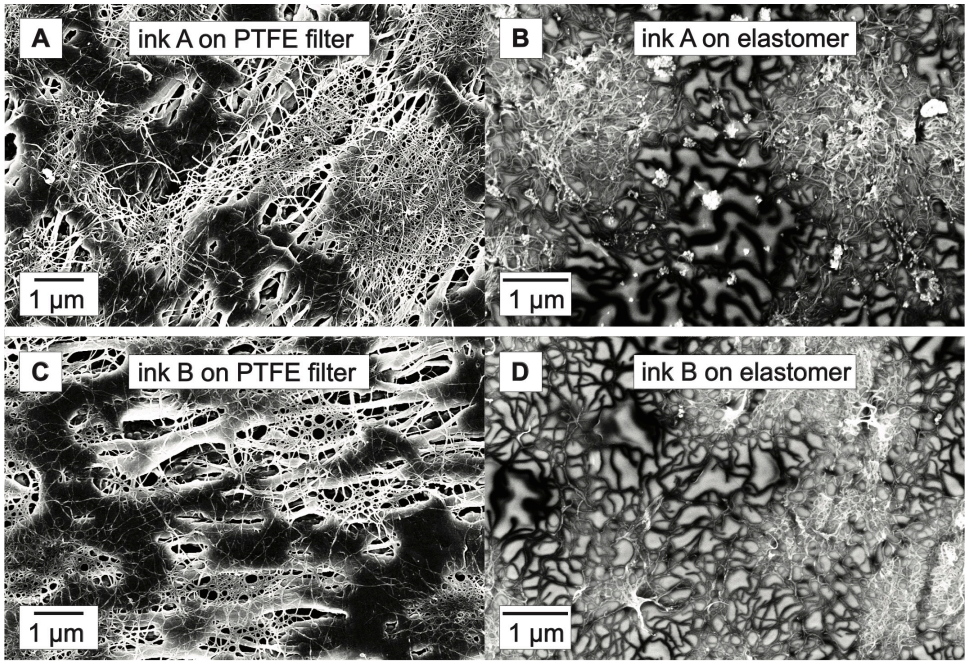


Figure 3.4: Electrodes on PTFE and elastomer substrates

A, SEM image of carbon nanotubes at 15.59 μL/cm^2 (ink A, post thermal treatment) on the PTFE transfer filter. The image shows aggregation of the carbon nanotubes is more prevalent near the filter's pores. **B**, SEM image of carbon nanotubes at 15.59 μL/cm^2 (ink B, post thermal treatment) on the PTFE transfer filter. The image shows aggregation of the carbon nanotubes is more prevalent near the filter's pores. **C**, SEM image of carbon nanotubes at 15.59 μL/cm^2 (ink A, post thermal treatment) on the acrylic elastomer. The image is distorted due to the non-conductive substrate, but overall shows a similar pattern of disperse and concentrated patches of carbon nanotubes. **D**, SEM image of carbon nanotubes at 15.59 μL/cm^2 (ink B, post thermal treatment) on the acrylic elastomer. The image is distorted due to the non-conductive substrate, but overall shows a similar pattern of disperse and concentrated patches of carbon nanotubes. The electrodes on PTFE were sputter coated with copper (10 second deposition, 600 mA, 400 V) using a Denton Vacuum Pro Desktop Coater (Moorestown, NJ).

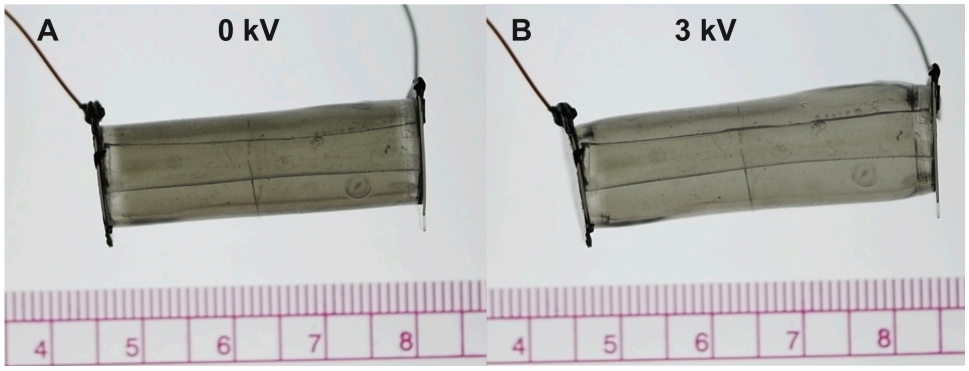


Figure 3.5: Example roll actuator

A, Example of an axial extending roll actuator in its relaxed state. **B**, Roll actuator powered to 3 kV.

same behavior is observed only when the applied voltage is the highest ever applied to the device (2-2.5 kV region, Fig. 3.6 D-F). The behavior is repeated when the actuators are charged to 3 kV for the first time (Fig. 3.7 B, D, F). By comparison, the current draws are similar at the twentieth cycle (Fig. 3.7 C, E, G), while the displacement is significantly smaller for the high areal density CNT electrodes. The leveling off in the current drawn suggested a self-clearing mechanism was occurring during the initial charge of the actuators[72]. Based on our observations and interpretation, the spikes in current cause localized heating and, therefore, partial damage to the electrode network. We expect that the same mechanism is responsible for the complete dielectric breakdown described in Fig. 3.1. Given that higher current spikes are correlated with higher areal density electrodes, it is likely that the CNT electrode morphology plays a significant role (Fig. 3.3). The cause of the current spikes is still unclear: one hypothesis is that the ends of the carbon nanotubes enhance the local electric field. Alternatively, the denser CNT patches may cause excessive heating relative the the more uniform network nearby, or poor bonding between adjacent layers. However, given our focus on maximizing actuator performance, we focused on the more robust electrodes made with low areal densities of ink for the remaining

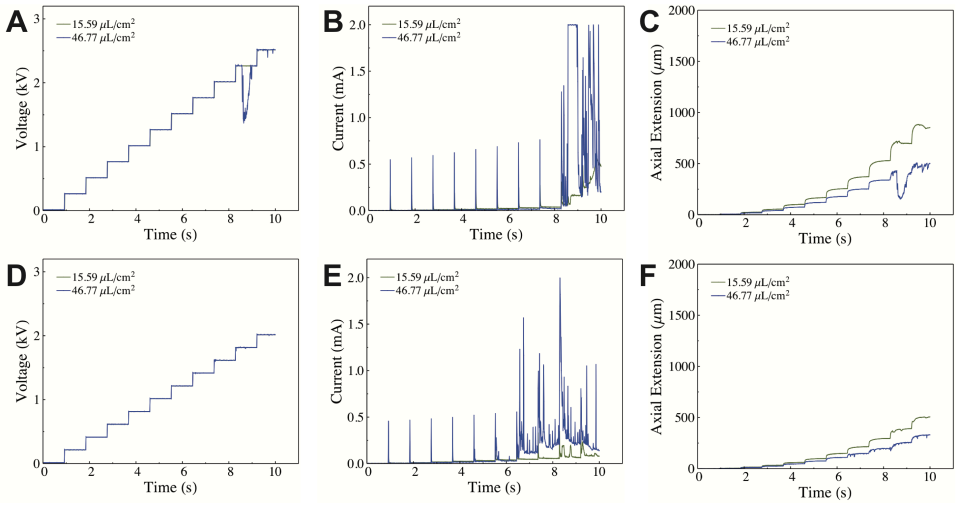


Figure 3.6: Early testing current peaks

A, Voltage applied to two axial extending roll actuators up to 2 kV. Actuators using two different ink B carbon nanotube area densities (15.59 and 46.77 μL/cm^2) **B**. Current response to applied voltage in **A**. **C**. Displacement of the actuators recorded in response to applied voltage in **A**. **D**. Voltage applied to two axial extending roll actuators up to 2.5 kV. Actuators using two different ink B carbon nanotube area densities (15.59 and 46.77 μL/cm^2) **E**. Current response to applied voltage in D. **F**. Displacement of the actuators recorded in response to applied voltage in D.

Table 3.1: Sheet resistances of different inks measured on PTFE support (all in kΩ/sq

Areal density of CNT ink (μL/cm^2)	Ink A not treated	Ink A treated	Ink B not treated	Ink B treated
10.4	>100	>100	>100	>100
20.8	>100	100	90	40
41.6	30	20	10	9.4
62.4	7.3	6.7	4.4	4.0
103.9	2.5	2.2	1.7	1.5

demonstrations.

To complete the electrode optimization we considered the impact of thermal treatment on the two ink types, for a constant CNT area density. In addition to measuring the displacement of linear expanding axial actuators, we also quantified the electrode sheet resistance, and the actuator capacitance at low voltage (Fig. 3.8). We expected that high sheet resistance electrodes will not be able to physically cover the entire elastomer surface effectively, leading to lower than calculated capacitance values, and lower actuator displacement. As expected, the actuators which exhibit the highest displacement also had the highest measured capacitance (Fig. 3.9). The best performing material was ink B after thermal treatment (vacuum for 2 h at 120C), suggesting that the removal of surfactant molecules yields the most effective CNT network. SEM imaging of ink B electrodes showed no significant change in the microstructure before and after thermal treatment (Fig. 3.10). Sheet resistance measurements of the inks on PTFE supports are in agreement with this trend (Table 1). Given the high breakdown fields ($>$ 100 V/μm) and large actuator displacements, we selected ink B, after thermal treatment, as the optimal electrode for our artificial muscles.

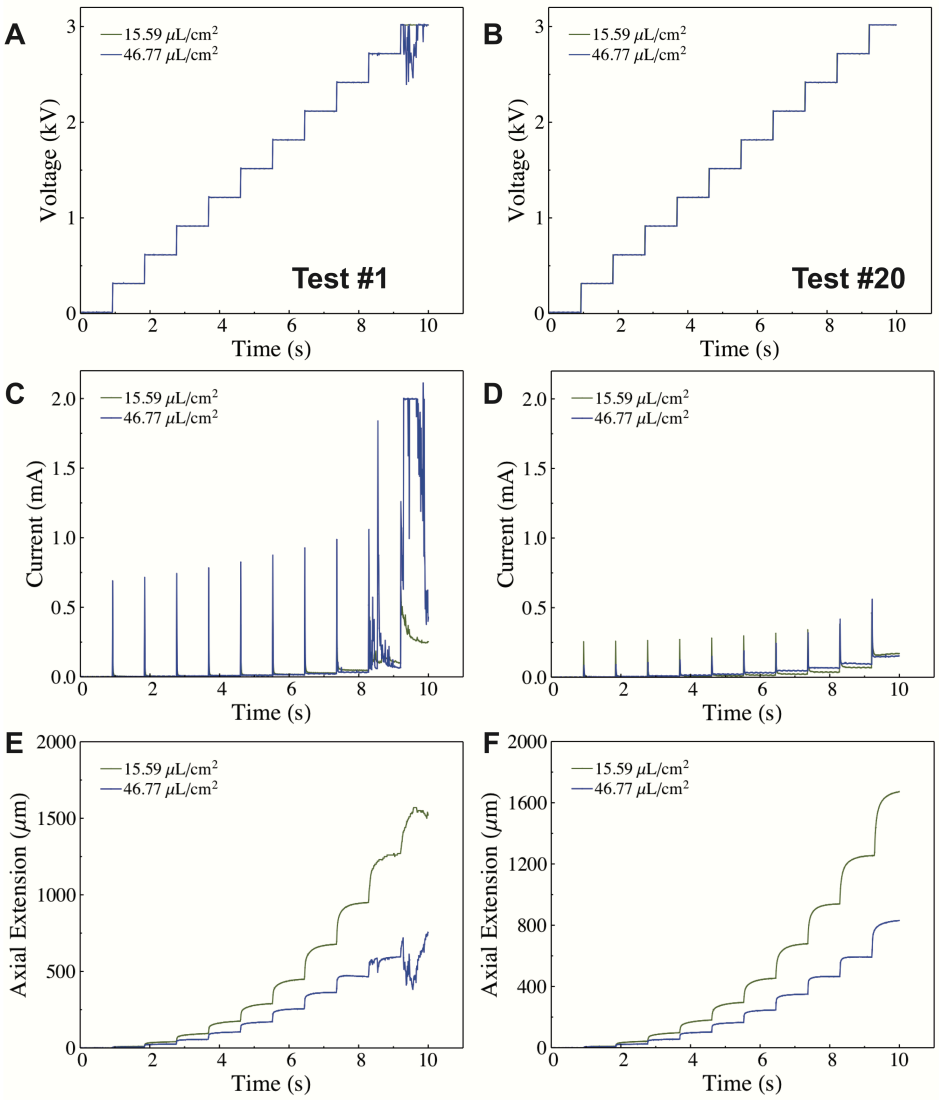


Figure 3.7: Self-clearing behavior

A, Applied voltage in 0.3 kV steps every 1 s for two roll actuators using ink B, after thermal treatment, at areal densities of 15.59 and 46.67 μL/cm^2, during the first test of the device. **B,** Corresponding applied voltage during the twentieth test of each device. The noise in the voltage applied to the actuator made with the higher ink areal density is due to high current peaks that reached the 2 mA safety limit of the power supply. **C,** Current response to applied voltage from **A**, during the first test. **D,** Current response to applied voltage from **B**, during the twentieth test. **E,** Actuator axial extension corresponding to **A**. The actuator heights are 1.1 cm for each device. **F,** Actuator axial extension corresponding to **B**. The largest displacement is measured in electrodes made with low areal density of CNT ink, indicating these materials are most suitable for building high performance artificial muscles.

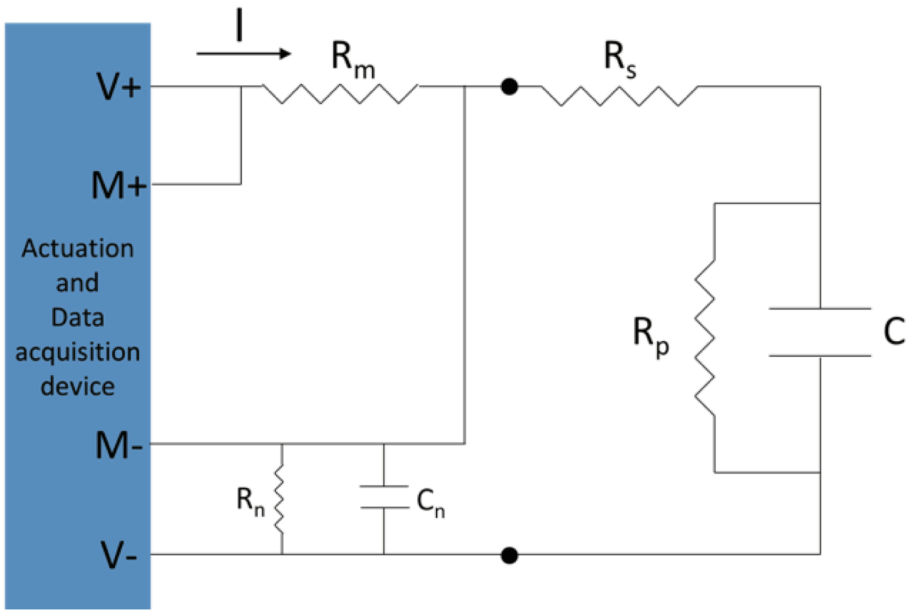


Figure 3.8: Capacitance measurement setup

Schematic of the circuit used to measure low voltage (10 V) capacitance of the linear expanding actuators for CNT ink selection. To measure the current input into a capacitance, we employ a known series resistance of 1 MOhm. The voltage across this measurement resistance (R_m) is monitored to obtain series current going to the capacitance. An algorithm is implemented to switch on V_{in} and monitor the instantaneous current through R_m, such that the leakage current and accumulated charges can be obtained. The capacitance value is measured for the no-load case, while keeping the leads of the measurement circuit disconnected. The measured capacitance for this case is denoted as C_n and the leakage resistance value is denoted as R_n. These measured values are the resistance and capacitance associated with the connector leads and internal circuit of the measurement setup. Once these values are obtained, the capacitance system in question is connected and the experiment is repeated. The noise values are subtracted from the experimental measurements and the capacitance values are corrected for series and parallel resistance.

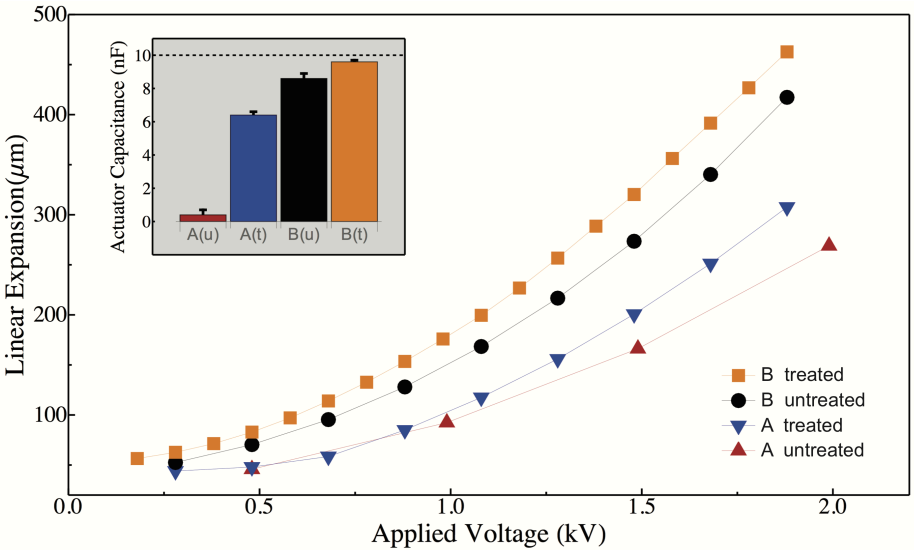


Figure 3.9: Impact of electrode heating on actuator performance
Actuator axial extension as a function of applied field for devices made with four different ink types. The dependence is parabolic: the displacement is proportional to the square of the applied electric field. Inset graph shows the measured actuator capacitance for each ink type. The dashed line corresponds to the calculated capacitance of the device based on geometry and material parameters. The results indicate that ink B after thermal treatment creates the most effective CNT electrode, and should be used in building artificial muscles.

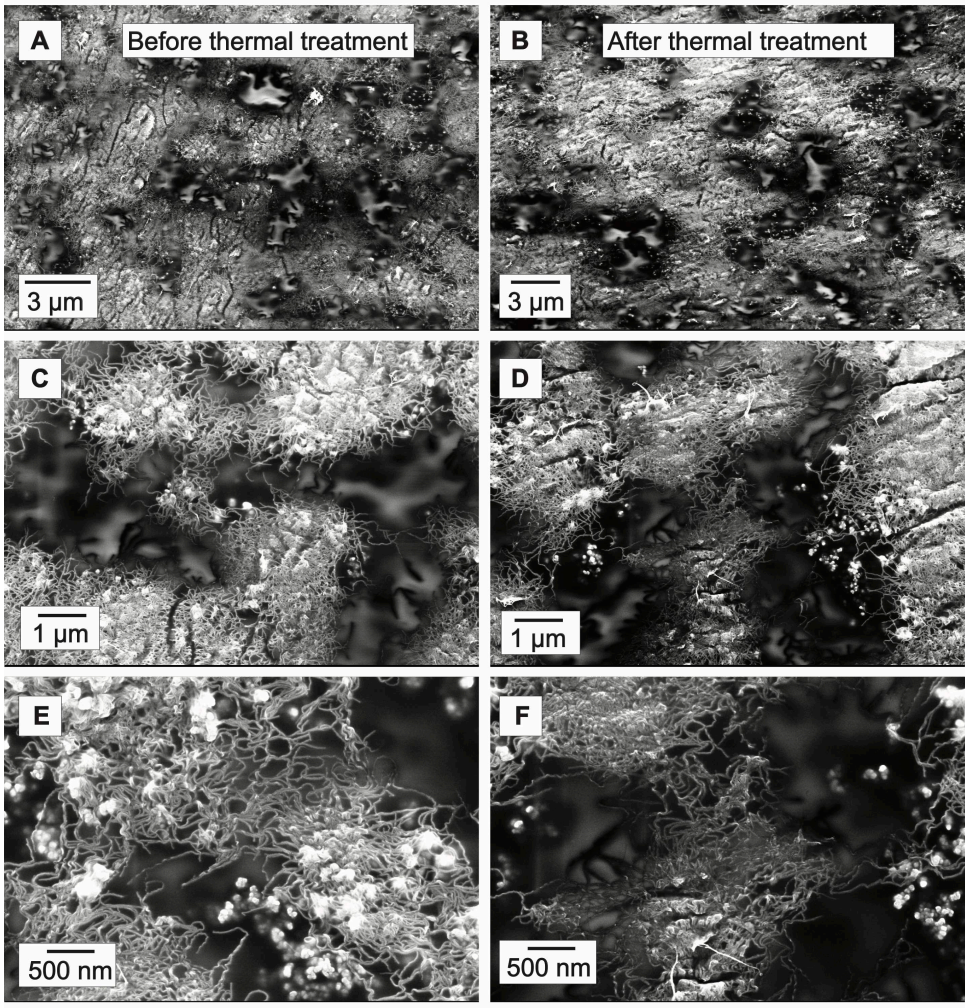


Figure 3.10: Impact of thermal treatment

A, C, E, SEM images of ink B CNTs transferred onto carbon tape directly from PTFE filter, at 12.99 μL/cm^2 before thermal treatment. The three images correspond to magnifications of 10k, 30k and 60k $\times$. **B, D, F**, SEM images of ink B CNTs transferred onto carbon tape directly from PTFE filter, at 12.99 μL/cm^2 after thermal treatment (120C for 2 hours under vacuum). The three images correspond to magnifications of 10k, 30k and 60k $\times$. The similarity between the untreated and treated samples suggests the increase in conductivity is not due to changes in morphology.

Table 3.2: Performance of dielectric elastomer actuators in comparison to natural muscles.

Electrode material	Natural muscle[29]	CNTs (this work)		Carbon powder[23]	Dispersed carbon [59]	Hydrogel[74]	Corrugated metal[75]
Action upon stimulation	Contract	Contract	Expand	Contract	Contract	Contract	Expand
Pre-strain (x × y)	N/A	1 × 1	1 × 1	1× 1	1 × 1	3 × 3.5	1 × 1
Electrode thickness (μm)	N/A	<0.1	<0.1	0.5-5	3-30	100-200	0.1-0.2
Applied Field (V/μm)	N/A	100-150	100-150	62	12	33	35
Applied Voltage (kV)	N/A	3.75	3.75	4	6	24	2.8
Actuation Strain (%)	10-30	24	22	30	16	69	2.5
Bandwidth (Hz)	2-180	1-10	1-10	N/A	N/A	20	10-100
Max power output (W/kg)	9-280	30-80	30-80	N/A	N/A	60-600[1]	5-50
Energy density (J/kg)	0.2-40	19.8	13.75	13	10	7-70[1]	0.5

[1] Lower bound includes estimated weight of fixtures required to maintain pre-stretch.

3.4 Artificial muscle demonstrations

By multilayering our UV curable elastomers and the optimized ink B electrodes, we built a linear contracting DEA to realize our goal of a fully soft, electrically-driven artificial muscle (Figure 3.11). We adapted our process to that of others[23, 59] and consisted of stacking 45 disks each of 26 layers to create a 1170 layer cylinder (Fig. 3.12). To characterize the usable energy density, we measured the weight (w), pull force in a mechanical tester with no displacement (F_b), and free displacement (d) against gravity of the actuator as a function of the applied electric field (Fig. 3.13). At high electric fields the energy density ($= F_b \times d/2w$) reached 19.8 J/kg (Fig. 3.14 **A**), while the displacement corresponded to 24% strain, covering a large segment of the performance envelope of natural muscles[73]. For mammalian muscles, the typical energy density is 8 J/kg, while the typical strain is 20%. Compared to earlier demonstrations of stacked DEAs, our devices have higher energy density, thinner electrodes (Table 2). Furthermore, our fabrication process allows independent tuning of the properties and processing of the elastomer together with the electrode.

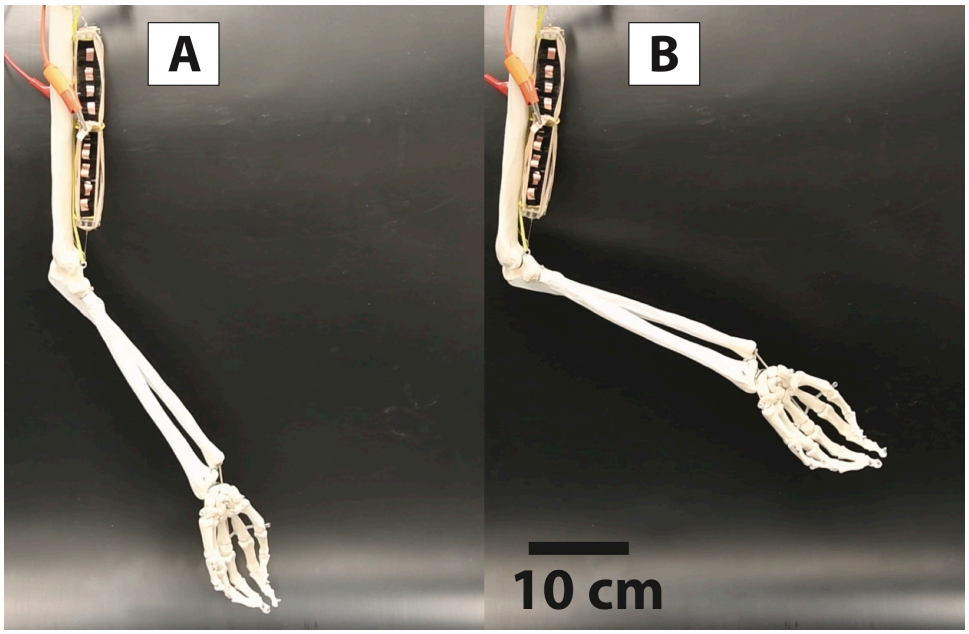


Figure 3.11: Artificial bicep demonstration

A contracting DEA is used to actuate a polymer replica of the bones of a human arm, with mechanics similar to a human bicep muscle. Metal wires serve as rigid links to connect the DEA to the bone. **A**, Relaxed. **B**, Contracted.

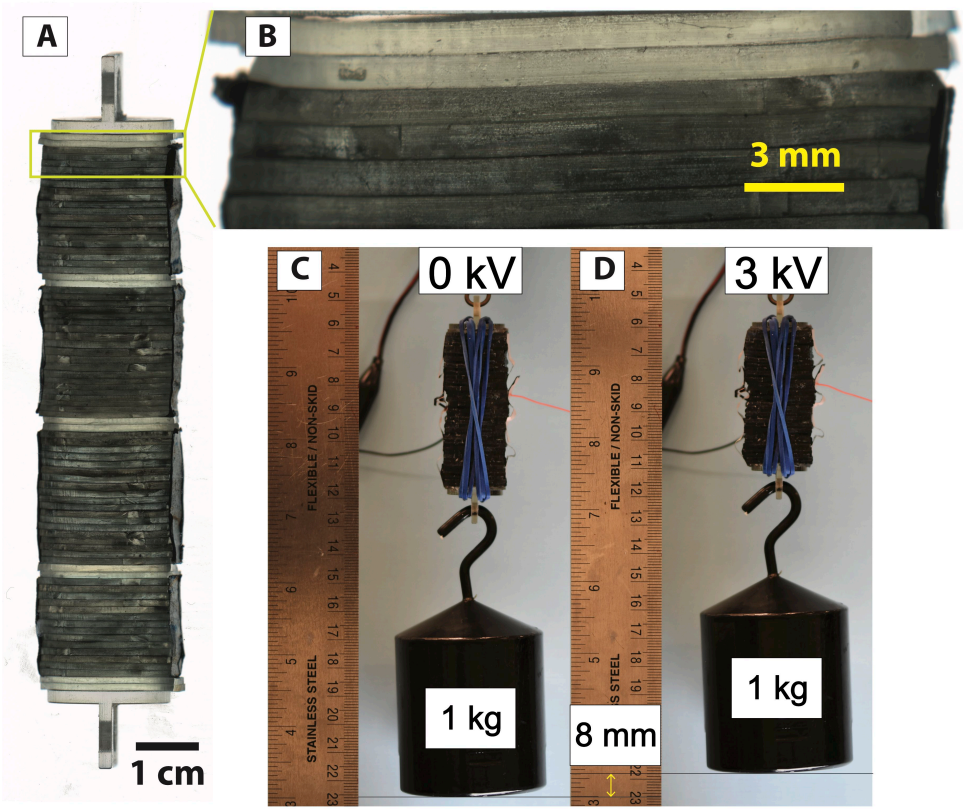


Figure 3.12: Linear contracting actuators

A, A contracting actuator showing multiple stacks of active elements (dark grey) alternating with passive elements (light grey) for enhanced adhesion. **B,** Zoomed in image of the top six stacks in the contracting actuator. Each stack consists of twenty five individual dielectric elastomer layers, each approximately 30 microns in thickness. **C,** Contracting actuator attached to a 1 kg weight without electrical power applied. **D,** Same actuator powered to 3.5 kV lifting a 1 kg weight by 8 mm.

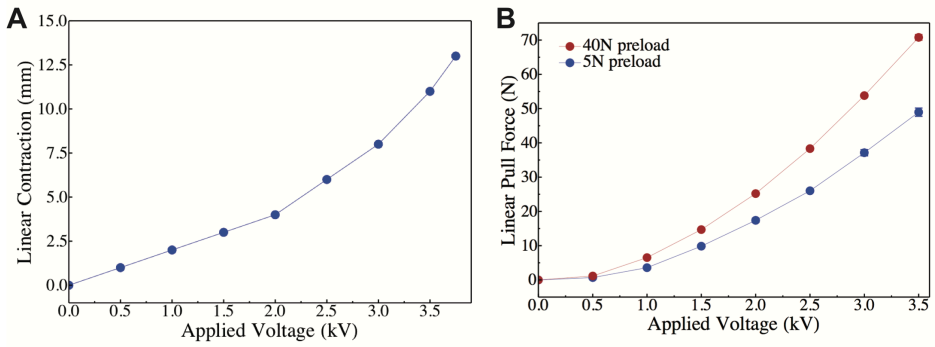


Figure 3.13: Linear contracting actuator performance

A, Measured free linear contraction as a function of applied voltage for a 20 g actuator with 30 μm layers. **B**, Measured pull force as a function of applied voltage for a 20 g actuator with 30 μm layers starting with either 5 or 40 N of compression.

The same building blocks can be used to demonstrate high energy density in linear expanding actuators. A similar performance evaluation of the expanding actuators (low ink areal density actuators from Fig. 3.7, using blocked force instead of pull force) demonstrated a peak energy density of 13.75 J/kg, while the displacement corresponded to 22% strain (Fig. 3.14). The lower energy density exhibited by the roll actuators compared to the contracting cylindrical actuators ones may be due to the mechanical energy lost to expanding the actuators radially. Relative to earlier examples[75], these linear actuators achieve a factor of almost 30$\times$ higher energy density, primarily due to the higher attainable applied electric field without dielectric breakdown. Despite the different geometry, both the expanding and contracting actuators exhibit similar bandwidth, by comparing displacement relative to the actuator length (Fig. 3.15 **B**). The results indicate that the device performance is not dictated by the final actuator geometry, but by the properties of the materials used as the building blocks.

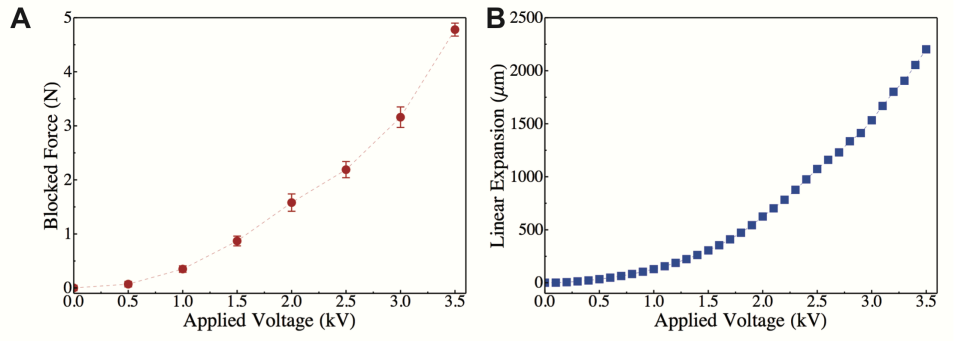


Figure 3.14: Roll actuator performance

A, Measured blocked force as a function of applied voltage for a 0.4 g actuator with 30 μm layers. **B**, Measured axial extension as a function of applied voltage for a 0.4 g actuator with 30 μm layers.

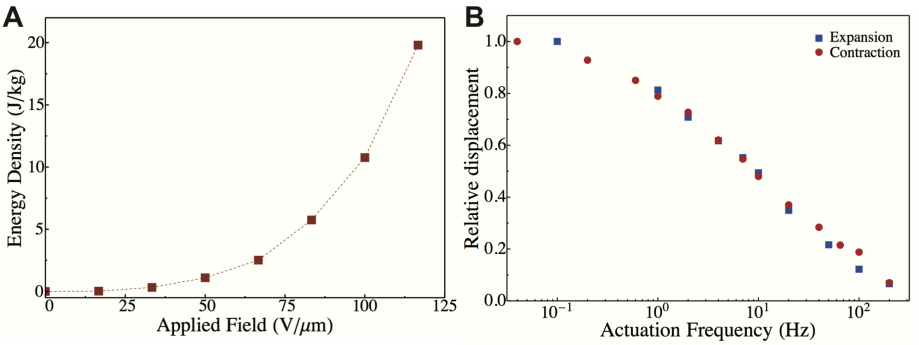


Figure 3.15: Actuator energy density and relative bandwidth

A,, Energy density of a 6 cm long, 20 g actuator increases as a function of the fourth power of the applied electric field. At the highest applied field, the actuator exhibits a peak energy density of 19.8 J/kg, on par with natural muscle. **B,** Comparison of relative displacements of contracting cylinder and expanding roll actuators as a function of actuation frequency at 3 kV. The similar performance of the different actuator types indicates the actuator response speed is limited by the viscoelasticity of the elastomer and not the geometry of the device.

Table 3.3: Comparison of actuator types

Areal density of CNT ink (μL/cm^2)	Area coverage (%)	Sheet Resistance (kΩ/sq)	RC time constant (ms)
15.59	55.8	60	20
46.67	85.9	9.4	5

3.5 Actuator bandwidth and cycle life

To understand the electronic and viscoleastic limits of the device, we characterized the actuator bandwidth (i.e., response time) and electrical properties. To this end, we compared the impact of two areal densities of ink B after heat treatment (15.59 and 46.67 μL/cm^2) on the actuator's linear expansion at a range of frequencies between 0.1 and 200 Hz. The test consisted of applying a sinusoidal voltage of 3 kV at a given frequency for 1-100 s, and measuring the free displacement. We observed no significant difference in displacement between the two actuators made with 15.59 and 46.67 μL/cm^2 ink electrodes, despite the 3$\times$ change in CNT concentration and corresponding 4$\times$ change in sheet resistance. For comparison, the capacitances of the two actuators were similar: 9.6 and 9.9 nF, for the low and high areal densities, respectively. The resistances were 0.6 and 2.2 MΩ, respectively. Both the bandwidth data and the RC time constants (5-20 ms) indicate the response was limited by material viscoelasticity (Fig. 3.16 **A**). These actuators did not reach full displacement at frequencies higher than 10 Hz, resulting in a power density on the lower end of the power density in mammalian muscles (100-400 W/kg). Increasing the power density further will require an increase in bandwidth, and thus materials with lower viscoelatic losses.

For completeness, a 0 to 3 kV 10 Hz frequency signal was applied continuously to explore device robustness. We observed no measurable degradation in performance for actuators made with the 15.59 μL/cm^2 ink B (Fig. 3.16 **B**) over the course of 100,000 cycles of continuous testing. The displacement of the actuators dropped to nearly half the initial value after 300,000 cycles. The

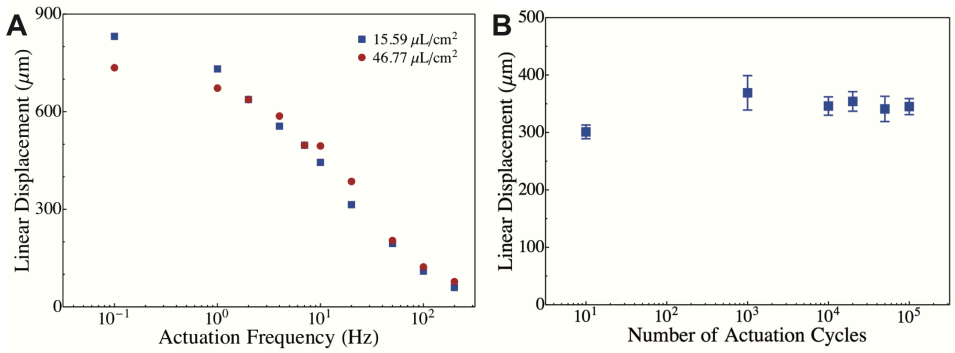


Figure 3.16: Limits of actuator performance

A. Roll actuator extension as a function of actuation frequency at 3 kV for two different CNT ink compositions. Both expanding actuators were cylindrical: 1.2 cm long, with a 1 cm diameter, made with ink B electrodes, after thermal treatment, at 15.59 and 46.77 μL/cm^2. The similar performance of different areal densities CNT inks indicate the actuator response is limited by the viscoelasticity of the elastomer and not the RC constant of the circuit. **B,** Roll actuator expansion as a function of number of cycles during continuous testing under a sine wave signal with 10 Hz frequency and 3 kV peak. The expanding actuator was a cylinder: 1.2 cm long, with a 1 cm diameter, made with ink B electrodes, after thermal treatment, at 15.59 μL/cm^2. The device is robust and can withstand 100,000 cycles without measurable degradation in mechanical performance. Each datapoint corresponds to the average displacement of the same device tested five times. The error bar corresponds to the standard deviation of the dataset.

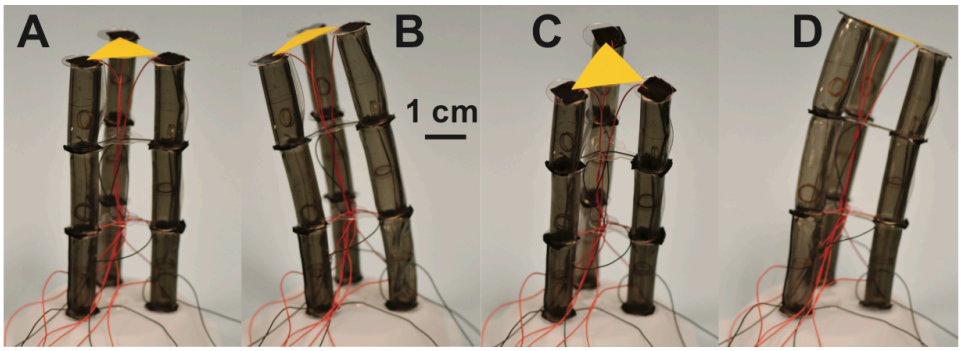


Figure 3.17: Artificial muscular hydrostat
Complex actuators made from simple bulding blocks: a muscular hydrostat replica made from linear expanding actuators powered to 3 kV. **A** relaxed state, **B** column 1 actuated, **C** column 2 actuated, **D** column 3 actuated.

exhibited fatigue may be due to damage to the carbon nanotube network, which could be reduced by blending with different nanoscale conductors, such as silver nanowires[76]. To match the robustness of natural muscles (10^9 cycles), we will need a better understanding of the device degradation.

3.6 Artificial muscular hydrostat demonstration

In addition, we used the established simple building blocks (expanding and bending actuators) to create more complex systems with additional capabilities. One example of these complex systems is as a muscular hydrostat replica made from linear expanding actuators, capable of both bending (tilt angles of 30° in three independent directions) and expansion (10% strain) (Fig. 3.17). We envisioned optimized versions of these types of enhanced actuators could find use in manipulation of delicate objects or other complex manipulation tasks.

3.7 Summary

The DEAs presented in this chapter exhibit the highest peak energy density to date, while still being soft and stretchable. By carefully selecting and processing

ultrathin nanoscale conductors we were able to apply high electric fields without risking premature dielectric breakdown. At high fields, the actuators show strain capability and energy density on par with natural muscles. We found that the actuator speed was limited by the elastomer viscoelasticity, not the electrode sheet resistance. This work represents a major step towards the realization of fully stretchable, electrically driven, strong, and fast artificial muscles to be implemented in a variety of soft machines that can interact with, enhance, or restore the function of the human body.

4

Swimming and crawling robots powered by multilayer DEAs

DEA-powered robots suffer from multiple limitations, primarily due to the need for pre-stretch and the high voltage required for actuation. In this chapter I present how multilayered dielectric elastomers can be used to overcome these limitations to acheive fast locomotion in crawling and swimming robots. The advantages of the multilayered actuators are highlighted by significant advances relative to the state of the art, including locomotion speed, ability to carry a power supply, and autonomy.

The most significant limitations of DEA-powered robots are below:

1. The pre-stretch of the elastomer increases the rigidity of the system, making DEAs less suitable for soft robotic applications. Moroever, the

rigid frame used to maintain pre-stretch limits the range of displacement of the actuator significantly[26, 32, 77].

2. Related to the small range of displacement is the fact that the actuators are not modular. Most often, the robot body consists primarily of the actuator, reducing the robot's functionality[78–80].

3. Some elastomers (primarily VHB) used have large viscoelastic losses which lead to slow locomotion[28, 81].

4. The actuation voltages require large power supplies causing most robots to operate in a tethered fashion[82].

5. No DEA-powered robots have been shown to respond to their environment and operate autonomously. Even systems which carry their own power supplies[79, 83] have limited on board sensing and computing capabilities.

6. The actuator energy density is low, limiting the use of DEAs to swimming and crawling robots. For other types of robots, DEAs cannot provide sufficient power for locomotion and are limited to auxiliary tasks, such as steering[30].

In this chapter we describe how multilayer DEA unimorph actuators can be made into an inchworm robot, a multi-legged crawling robot, and an autonomous swimming robot. Unimorphs are shown to be versatile building blocks that can be used independently or jointly, as a bimorph, to produce rapid movements.

4.1 Unimorphs as inchworm robots

Simple, soft robots hold tremendous promise for exploration and use in challenging environments. Locomotion in soft robots is typically achieved using pneumatic or hydraulic actuators, and are limited by both the viscoelasticity of the constituent materials, and the rate at which fluid can be pumped to the

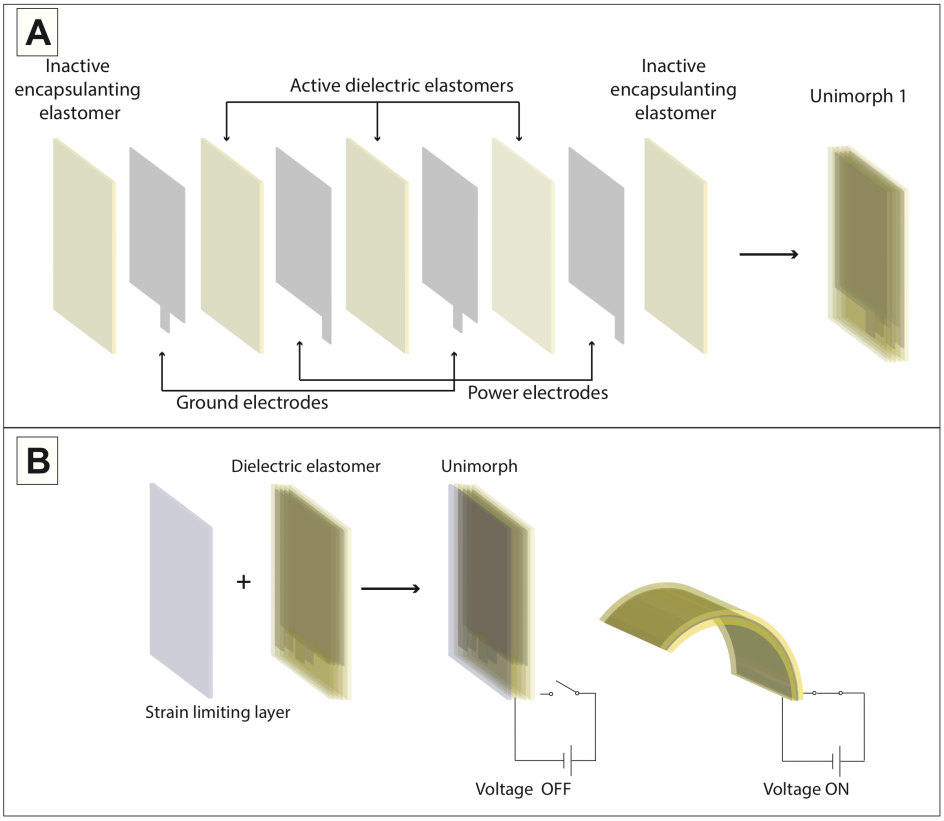


Figure 4.1: Unimorph fabrication and operation
A, Components of a multilayer unimorph actuator made using the established process. **B**, Bending of a unimorph due to a strain limiting layer.

device[84]. Alternative solutions include inchworms powered by shape memory alloys (SMA)[85] or electrical motors[86], as well as peristaltic "meshworms" driven by NiTi alloys[87]. Both SMAs and motors are driven electrically, which avoids the need for additional energy conversion sytems (i.e., from battery to compressed gas) and offsets the inherent disadvantage of using rigid actuators.

Alternatively, other groups have explored using the expansion mode of a DEA to create motion in simple robotic systems with unimorph or bimorph actuators. One method to increase the force output is to increase the thickness of the

elastomer[45]; however, thicker elastomers require larger voltages to deform (>15 kV) making power conversion a challenging task. For DEAs which use the expansion mode, the solution to increase force at low operating voltages is to create multilayer devices, stacking electrodes and elastomers[42]. Targeting soft robots capable of rapid locomotion, we created single and multi-actuator robots based on a simple unimorph geometry using our multilayer fabrication method (Figure 4.1).

Simple inchworms and four legged robots were created using the methods outlined above. The inchworm robots were selected because of their simplicity of fabrication, as well as the many similar examples available in literature to compare crawling speeds. Conversion of unimorph bending to effective inchworm forward motion requires sufficient deformation of the actuator, as well as directional friction to the surface the robot is walking on. These conditions apply to single degree-of- freedom (DOF) actuation, as inchworms can also be assembled in series to create undulatory motion that is less dependent on friction.

Effective directional friction was essential for maintaining a consistent crawling direction (Figure 4.2). Satisfactory locomotion was obtained using aligned sharp needles or hooks on the posterior end. This differential friction mechanism, inspired by earlier work on microspines[88], was considered the simplest and most efficient method for such a simple and lightweight (<200 mg) crawler. Robots outfitted with these straight needles were extremely effective and exhibited high crawling speeds of up to one body length per second (BL/s). Multiple types of crawling surfaces were tested, including paper, soft silicone elastomer, and sandpaper of varying roughness.

Speeds for crawling on paper, and silicone elastomer substrates are presented in Figure 4.3. At low frequencies all steps are effective and little slip is observed, therefore the crawling speed is directly proportional to the driving frequency. As the driving frequency is increased, some slipping begins to occur and the speed reaches a plateau. At high frequencies the DEA cannot deform quickly enough

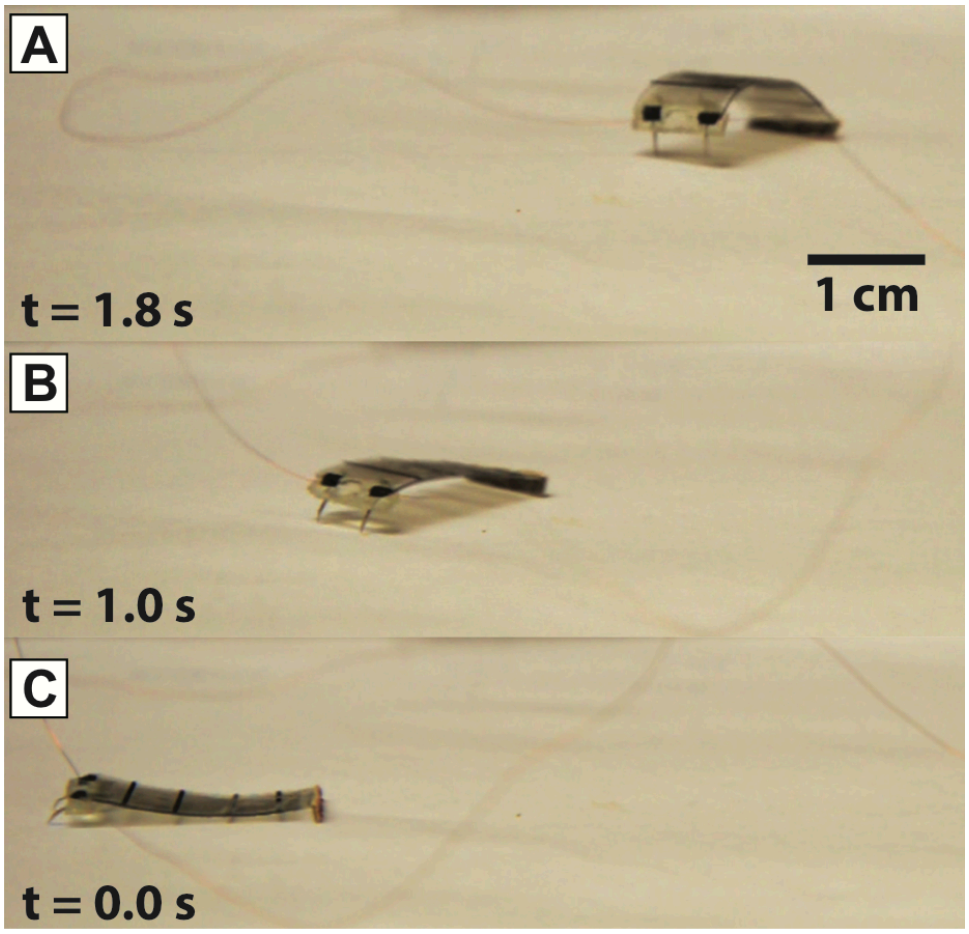


Figure 4.2: Crawling inchworm robot

A,B,C Crawling inchworm robot made using elastomer C at three points in time. The actuator was driven by a 2 kV, 10 Hz sinusoidal signal.

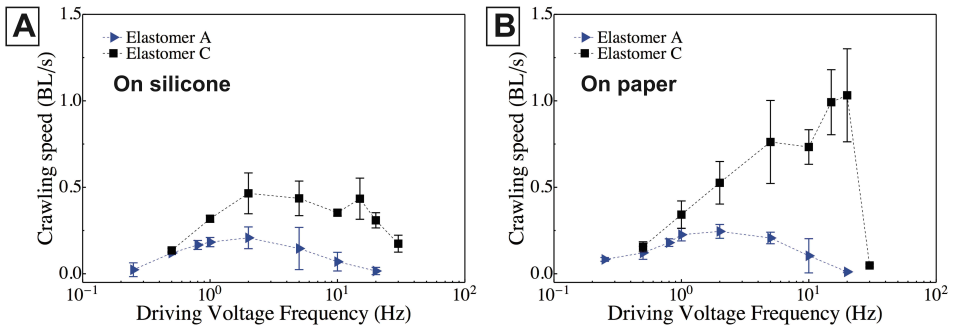


Figure 4.3: Inchworm robot crawling speeds
Crawling speeds for the five active layer inchworm actuators made using elastomers A and C on **A**, silicone elastomer and **B**, paper surfaces. The error bars correspond to the standard deviation from five separate trials on the same robot.

and the robot does not move. A demonstration of their crawling ability shows the unimorph robots capable of faster locomotion due to the elastomer used, but worse directional control (Figure 4.2). The actuator control was open loop, as voltage was applied as a square wave of varying frequency using a Trek 610E power supply and a Wavetek 75 Arbitrary Waveform Generator. The behaviors match earlier results that show elastomer C to be capable of actuation at higher driving frequencies than A, due to viscoelastic effects. The relative performance to other DEA-powered and soft robotic systems is compared in depth in Table 1.

4.2 Multi-legged crawling robot

To demonstrate the versatility of our fabrication method, we also made four-legged crawling robots combining multiple inchworm actuators (Figure 4.4). While they are considerably slower than the simpler inchworms (Figure 4.5), they are more complex, capable of multiple actuation modes, including different crawling gaits. Moreover, four legged robots have greater directional control and could more readily accommodate an energy supply, power converter,

Table 4.1: Comparison of robot speeds.

Robot type	Actuator type	Maximum speed [BL/s]
4 legged multigait[5]	Pneumatic	0.0077
Annelid[32]	12 layer DEA[1]	0.05
Inchworm[28]	Single layer DEA	0.028
Hexapod[89]	Multilayer DEA[1]	0.64
Inchworm[89]	Multilayer DEA	0.60
Inchworm[70] - elastomer A	Multilayer DEA	0.25
Inchworm[70] - elastomer C	Multilayer DEA	1.03
4 legged[70] - elastomer A	Multilayer DEA	0.115

[1] These robots have a primarily rigid body.

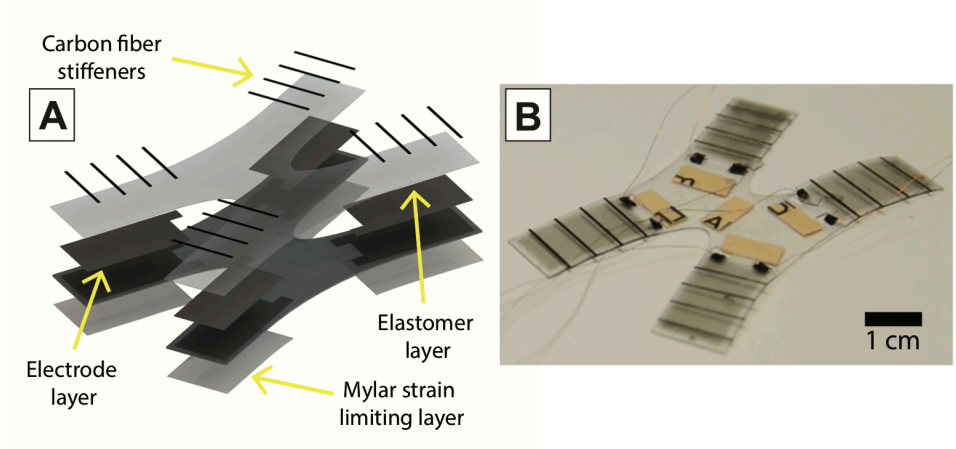


Figure 4.4: Multi-legged robot construction

A, Diagram of components of a four leg crawling robot based on multilayer actuators. **B**, Photograph of robot built from those components.

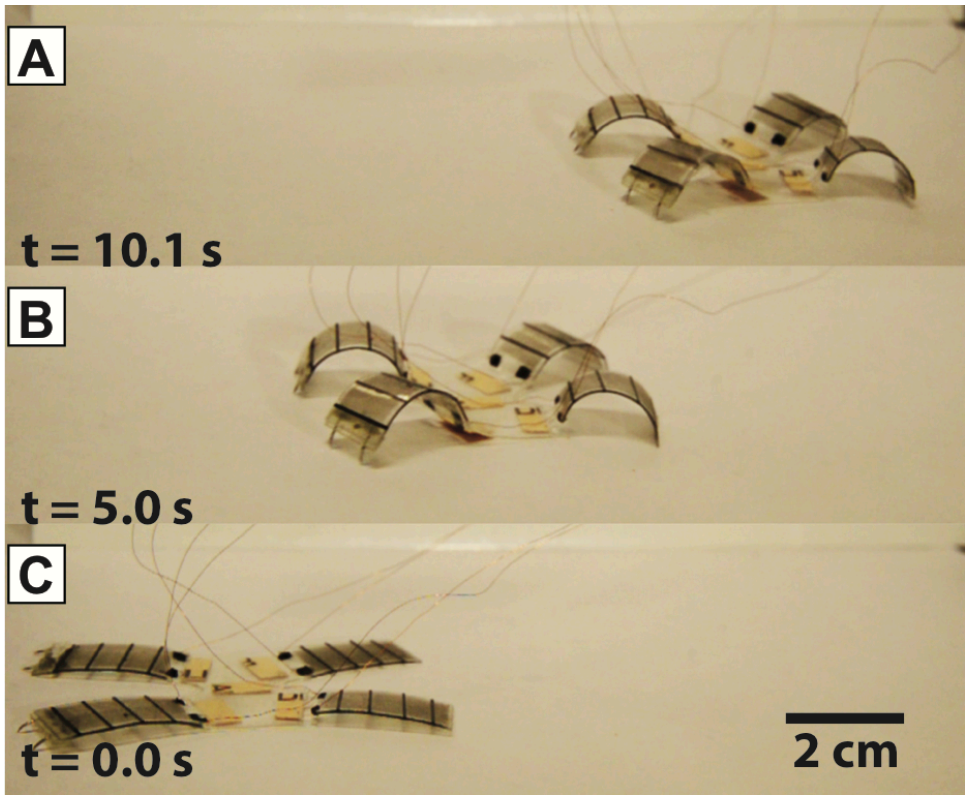


Figure 4.5: Multi-legged robot locomotion
A,B,C Crawling inchworm robot made using elastomer C at three points in time. All four actuators were driven by a 2 kV, 10 Hz sinusoidal signal.

and control unit in future efforts.

By building upon our multilayer fabrication method we were able to create devices with fast response times while requiring just five dielectric elastomers layers resulting in actuation at lower voltage and and with higher energy density than previously demonstrated DEA-based unimorphs, for one specific elastomer type. While the current four-legged robot is relatively slow, incorporation of elastomer C, as well as studies of the optimal actuation pattern may increase its speed considerably. Moreover, this novel design can serve as a test bed for creating fast, compliant and untethered DEA-based robots to continue to push the boundaries of soft robotics. Overall, the multilayer crawling inchworms have

been shown to overcome the issues due to limited range of motion (1), and lack of modularity of the DEA relative to the rest of the robot body (2), while crawling relatively fast (3).

4.3 Motivation for swimming applications

When actuators are small, easy to manufacture and require small power supplies, they become suitable for cooperative robotics using swarms of untethered robots [90]. Given the need for better soft actuators at the mesoscale, our goal was to build an untethered DEA-powered swimming robot to serve as a stepping stone in two directions: towards fully soft swimming robots and towards cooperative swarms of mesoscale robots. To this end, we built a modular multilayer DEA capable of powering a miniature underwater vehicle (Figure 4.12). Our contribution is the integration of a soft and powerful actuator into a small and fully self-contained package that can be easily mounted on autonomous underwater vehicles (AUVs) of various shapes. The fabrication of the actuator is straightforward as no pre-stretch of the elastomer is required. The sealing requirements are minimal as only four wires per actuator penetrate the vehicle's body. Several actuation layers can be stacked to increase the total actuator power output. Design guidelines for the development of powerful fin-like DEAs are detailed in Section 4.6. The reconfigurable and miniature AUV is shown in Section 4.7. Results including measurements of thrust and speed as well as planar swimming and vertical diving are discussed in Section 4.6, 4.8, and 4.9.

For swimming robots powered by DEAs, the only untethered example is an electronic fish by Li et al. [79], which reaches speeds of up to 6.4 cm/s (= 0.69 BL/s). The robot uses a pre-stretched membrane at the center of the body to power passive fins in a sting ray inspired configuration. Their 93 mm long robot uses the surrounding medium (water) as ground in order to facilitate the insulation of the high voltage actuators. The robot is therefore coupled with its environment; several such robots in a single tank of water might cause unsafe voltages. Shintake et al. [82] presented tethered biomimetic underwater robots,

which are capable of either vertical or horizontal motion, depending on how the robot is built. The DEA in the fish-like design is spread over a thin and bendable 120 mm long body. Their fish-like robot achieved top speeds of 8 mm/s (= 0.07 BL/s). Other work includes a jellyfish inspired dive-capable robot [78] which also makes use of a pre-stretched dielectric elastomer membrane.

Dielectric elastomer actuators have unique advantages in an untethered swimming demonstration compared to other soft actuation technologies. Since DEAs are electrically powered, their power supplies could be smaller, with fewer components than those used by fluidic elastomer actuators [91]. Other electrically powered actuators, such as ionic polymer-metal composites (IPMCs) are generally slower [92] (0.1 BL/s), [93] (0.05 BL/s) due to limitations of ionic diffusion compared to fast switching of electric fields. Lastly, shape memory alloys (SMAs) can be driven to swim fast by relatively compact power electronics [94] (0.2 BL/s), [95] (0.95 BL/s), but require more complex fabrication and integration of rigid and soft components, yielding a system with very low energy efficiency. With our approach, DEA-powered swimming robots could be made as fast as fluidic or SMA-powered robots, while maintaining a small footprint of the power electronics and a simple fabrication process of the actuator.

Our multilayered actuator differs from the existing body of work on DEAs due to: (i) our actuator is modular and independent of the robot body as opposed to other examples [78, 79, 82, 83]; (ii) the low footprint power supply makes our robot autonomous compared to [78, 82]; (iii) the size, initial shape, and final deformed shape of the actuator can each be independently tuned to match a desired target of thrust, speed, etc. Beyond these major advances, our actuator is sealed and safe to operate in water which allows for collective operation of multiple DEA-powered robots. Moreover, the fins are active, meaning the soft material deforms to propel the robot in a similar fashion to how biological systems swim. Such soft and tunable actuators could be used for robotics-inspired biological studies to better understand underwater locomotion. We present the design and working principle of our DEA in the following section.

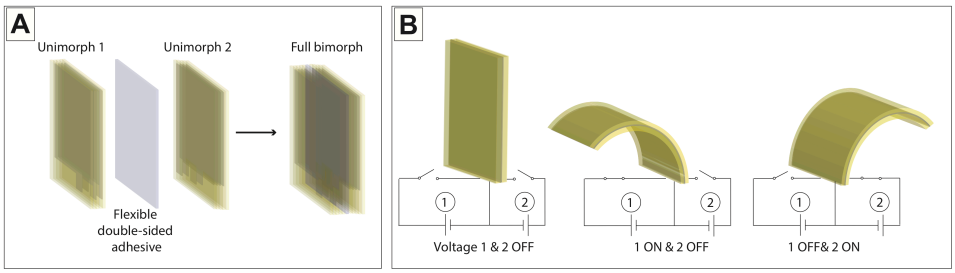


Figure 4.6: Bimorph construction and operation

A, Formation of a bimorph from two unimorphs and a flexible adhesive. **B**, Operation of a bimorph actuator. The two multilayer actuators comprising the bimorph are assembled in a simple way using a flexible adhesive. The proximal end of the stack is taken to be the mechanical ground, which can be rigidly attached to a robot.

4.4 Bimorph actuator design

Earlier we described a reliable method to build multilayer DEAs that can be made into fast unimorph bending actuators [57, 70]. Following the same reasoning as other research groups [96], we adapted a method to produce bimorph actuators which can flap and propel a swimming robot. Two similar unimorph actuators are bonded using a flexible double-sided adhesive (82600 from 3M Corporation, St. Paul, MN) to create a bimorph architecture as shown in Figure 4.6 **A**. When one half of the bimorph is actuated, the second half and the adhesive serve as a non-stretchable constraint, directing the actuator to bend, as shown in Figure 4.6 **B**. We used a model developed earlier [70] to guide the selection of layer thickness, number of layers, as well as the applied voltage. When testing full bimorphs in water we discovered the model predictions to be optimistic higher bounds due to localized electrical breakdown in the elastomer. However, we considered the low fabrication yield versus high thrust trade-off to be valuable. We report on the bimorphs which had a low concentration of defects in the electrodes and produced the highest thrust to demonstrate this technology.

The applied voltage was fixed to 2 kV to minimize the chance of electrical

breakdown. Since the actuator thrust output dictates swimming performance, we modified the design parameters, such as stiffness and number of layers, to increase the thrust output. The setup and method of measuring thrust is described in detail in Section 4.5. The actuator active area was limited to 20 mm $\times$ 25 mm by the size of the single-walled carbon nanotube (CNT) transfer filter. The results of the impact study for number of layers, material stiffness, and the relative trade-offs are discussed in Section 4.6. For consistency, and to link with the spin coating steps during fabrication, the bimorphs are labeled with the total number of layers (including sealing layers) per each unimorph. For example, a 17 layer fin includes two 17 layer unimorphs held together by a layer of double sided adhesive. The unimorphs can be made in parallel on a large wafer meaning that the total process time is dictated by the number of spin coating steps.

4.5 Bimorph fin testing setup

Soft actuators are traditionally less precise than their rigid counterparts, which makes them difficult to quantify. Our experimental setup allowed us to measure the forces generated by the DEA-fins, investigate their consistency, and improve the fin design.

We measured the thrust forces generated by the DEA-fins in a 1.2 m $\times$ 0.6 m $\times$ 0.5 m glass tank filled with still water. For this purpose, we mounted a rail across the tank, to which we attached a pivoted cantilever and a single-axis load cell (Transducer Techniques GSO-10). The cantilever rigidly connects the submerged fin to the load cell, which is above the waterline. The force generated by the fin causes the cantilever to rotate around a low-friction ceramic ball bearing and push on the load cell. The 100 mN range of the load cell is reached at a compression of 0.1 mm only. Consequently, the maximum angle of rotation in our cantilever design measures 0.2 $^\circ$ and satisfies a small-angle approximation. We mounted the cantilever and the load cell separately to prevent overloading of the load cell. The signal from the load cell is conditioned (Transducer Techniques LCA-RTC) and measured with an Arduino Uno at 100 Hz. The load

cell was calibrated with known loads in air prior to experiments in water. Our values for the static thrust measured in still water are expected to be lower than the dynamic thrust generated during free swimming where vortex shedding adds to the propulsion [97, 98].

4.6 Bimorph actuator optimization

Each multilayer was built with an inactive base and top soft elastomer layer (0 % crosslinker corresponding to a Young's modulus of 50 kPa) which provided insulation from the water environment. The elastomer formulation was based on acrylic urethane oligomers (CN9018 from Sartomer, West Chester, PA). The crosslinker 1,6-hexanediol diacrylate (HDDA from Sigma Aldrich, St. Louis, MO) was used in the 5-12.5 % range. The oligomers were spin coated at 6000 RPM for 60 s to make 35 micron layers. Each layer was cured by exposure to UV light in the absence of oxygen for 120 s. Electrodes were transferred to both sides of each active elastomer layer by stamping single-walled carbon nanotubes (CNTs from NanoC, Westwood, MA) from a PTFE filter.

The flapping motion of the fin is achieved by alternately switching on and off the two halves of the bimorph DEA (see Figure 4.6). Any frequency up to 10 Hz can be chosen and controlled by the microcontroller. The amplitude is dependent on the size, strength, and flexibility of the fin and decreases with increasing frequency at a constant applied electric field. The flapping direction is switched at low voltage before one voltage converter (EMCO AG30) per unimorph provides the required actuation voltage of 2 kV.

We kept the size of our DEA-fins constant at 20 mm $\times$ 25 mm and chose a generic rectangular shape to allow for a fair comparison between fins. We varied simple fabrication parameters, such as the number of layers of each fin and the stiffness of the elastomers and measured the force output of the fins. Fluid dynamic considerations were not part of our studies. A model for, and information about, the thrust production of oscillating fins can be found

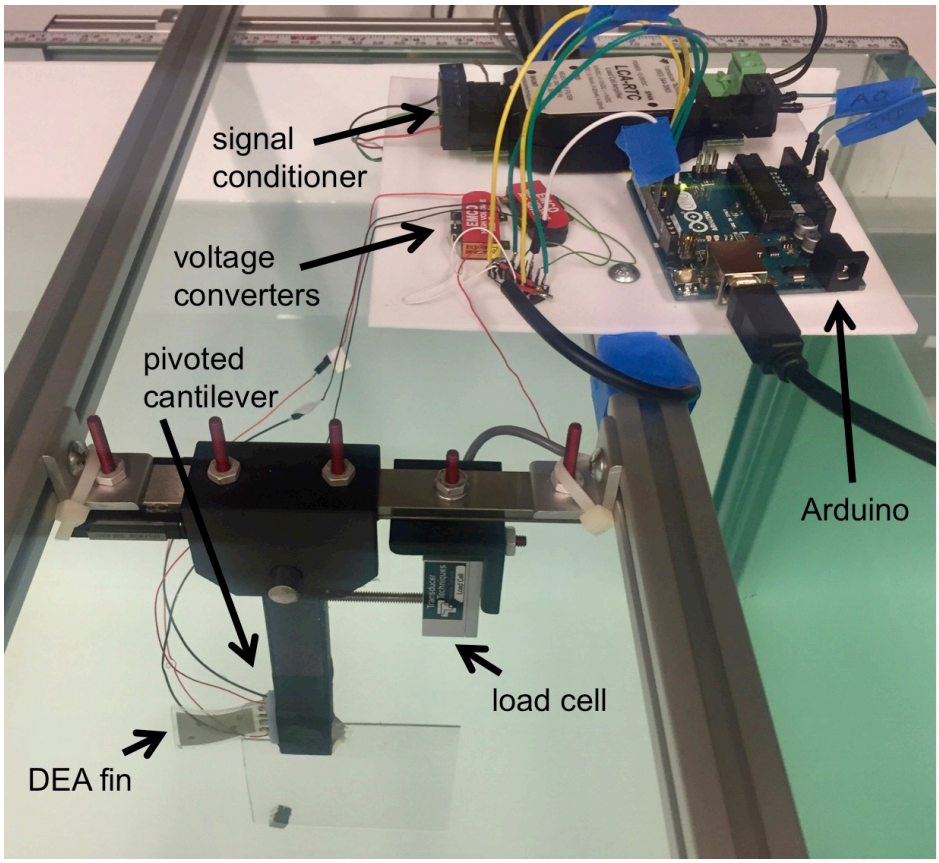


Figure 4.7: Fin thrust measurement setup

Our measurement setup installed across the tank. The Arduino commands the voltage converters, which actuate the DEA-fin. The generated thrust force makes the cantilever push on the load cell. The force signal is conditioned by the signal conditioner and read from the Arduino.

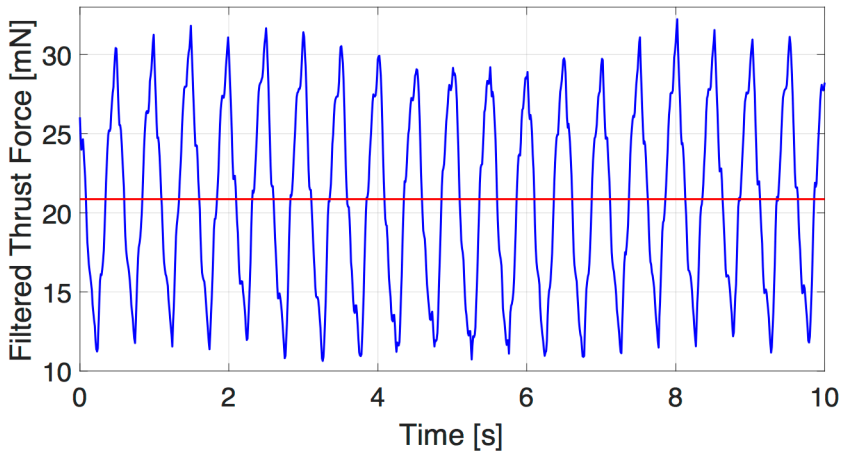


Figure 4.8: Thrust output vs. time
Time trace of the measured thrust force for a 17 layer fin at 2.0 Hz with its average being shown in red..

in [96, 99].

In a first step, we validated our measurement setup by looking at the time trace of the measured thrust force. The force data in Figure 4.8 was filtered with an equally weighted and 25 element long moving average filter. The observed sinusoid correlates with our input signal and constitutes the expected thrust pattern as shown in Figure 8 of [96].

In this and the following subsection, we present the resulting thrust forces for a variety of fins actuated at 1.0 Hz to 5.0 Hz in increments of 0.25 Hz. At each frequency, we measured the output thrust force at a sampling rate of 100 Hz for a duration of 10 s and averaged those 1000 samples to a single data point. We repeated this measurement procedure five times per fin and derived the mean and standard deviation as shown for an example 17 layer fin in Figure 4.9. The five measurements per fin were consistent with each other as the standard deviation was at least an order of magnitude smaller than the measured average force.

Figure 4.10 shows that the thrust force increases with the number of active

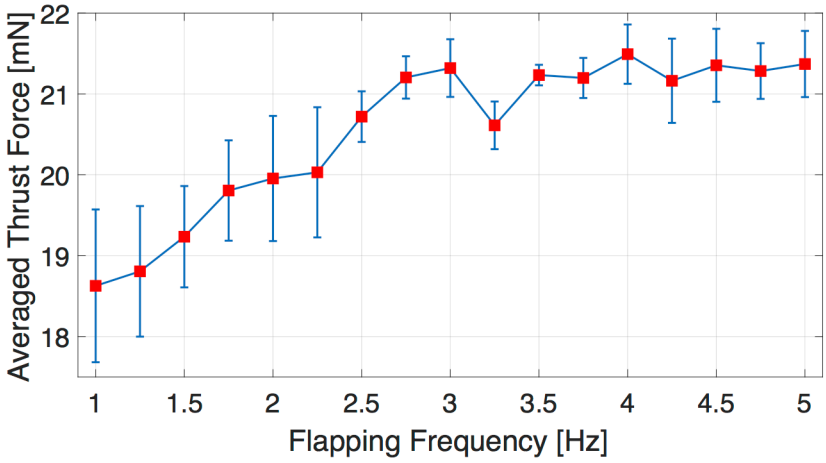


Figure 4.9: Thrust output vs. frequency
Average (red squares) and standard deviation (vertical errorbars) of measured thrust forces from five test runs with a 17 layer fin using 10 % HDDA crosslinker..

layers. There is a threshold thickness under which the fin is too soft and almost no useful thrust is generated, as shown by the seven layer fin. While this result is expected, there is a practical constraint to how many layers can be stacked. Operating these materials at 15-20 V/μm we found each layer to have a 1 % chance of electrical breakdown. For stacks of more than twenty layers the likelihood of breakdown approaches 20 %, which has a significant impact on fabrication yield.

In this experiment, we varied the stiffnesses of the elastomers by tuning the amount of HDDA crosslinker in the starting oligomer precursor from 5 % to 12.5 % corresponding to a Young's modulus of 200 kPa to 500 kPa, respectively. Our earlier model (described in Chapter 2), though based on a static configuration, was useful in providing guidelines for the range of material stiffness of interest. The lower limit was set by the minimal stiffness needed to prevent an electromechanical instability, in which the material becomes softer with applied deformation leading to electrical breakdown in the elastomer. The upper limit was set by the Young's modulus of the elastomer: the bimorphs made

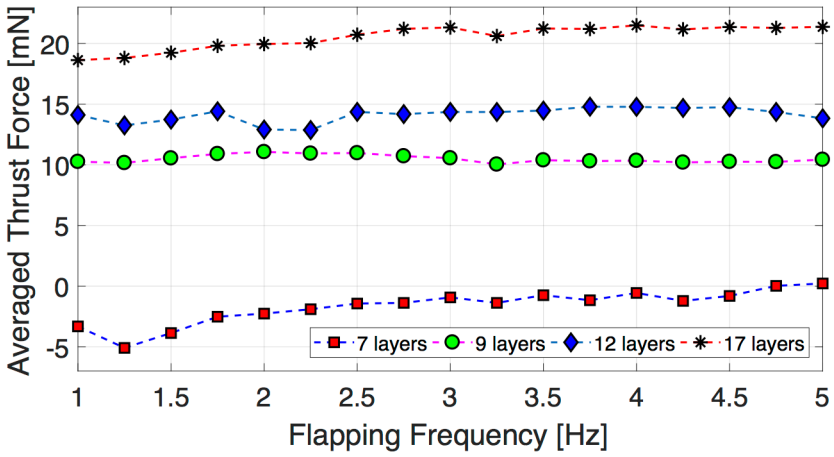


Figure 4.10: Thrust output vs. number of layers
Dependence of thrust on number of layers in the bimorph (all elastomers contain 10 % HDDA crosslinker).

with elastomers stiffer than 500 kPa did not deform enough to produce measurable thrust at the comparable electric fields. The model predicted the thrust to decrease linearly with increasing stiffness as the amplitude of each flap decreased at constant field. However, the mass of the water that must be displaced for a successful fin flap reduces the effectiveness of the softer elastomers leading to a peak in the thrust versus stiffness analysis. Figure 4.11 shows that the trust force is highest for elastomers containing 7.5 % crosslinker.

Based on the results of the thrust measurements we used a 17 layer fin made of elastomer containing 7.5 % crosslinker. Using the lessons from Figures **??** we aimed to operate the robot at the lowest frequency which maximized the thrust output to achieve fast swimming at a lower power. In this case that meant running the fin at 2.2 Hz produced speeds of up to 0.55 BL/s (= 55 mm/s), and turning radii as small as 1.2 BL (= 120 mm)[100].

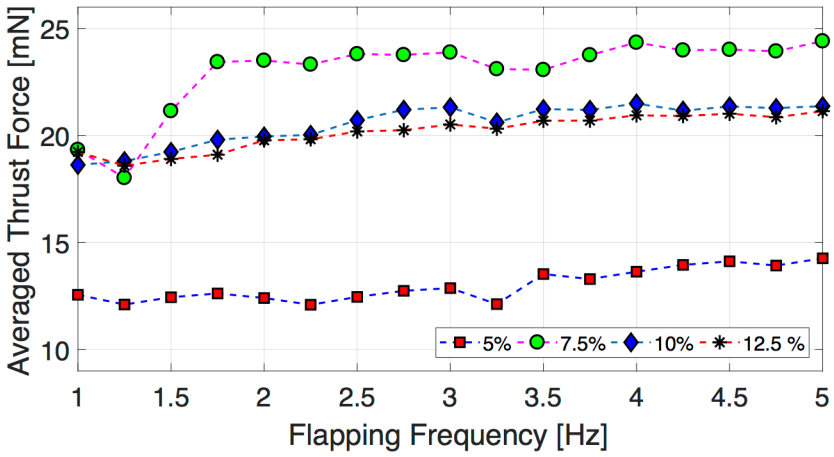


Figure 4.11: Thrust output vs. elastomer stiffness
Dependence of thrust on amount of crosslinker in the elastomer, which dictates material stiffness. All actuators tested were based on 17 layer unimorphs.

4.7 Robot design

The robot as shown in Figure 4.12 is 100 mm long, 60 mm high, and 30 mm wide at a mass of 115 g. At this size, the robot is big enough to hold all the electronics. The 3D-printed (Stratasys Objet500) plastic body contains an Arduino Pro Mini microcontroller, an SD card reader/writer for data logging, a Li-Ion battery (7.4 V, 180 mAh), and a power circuit to provide the high actuation voltage to the DEAs. A pressure sensor (TE Connectivity MS5803-02BA) was used for depth control, an LED for status indication, two waterproof Micro-B USBs for charging and programming, and an on/off switch penetrated the top end of the body; a ground and two positive supply voltage cables are routed to the DEA-driven fin at the back.

The robot is slightly positively buoyant and floats at the water surface if not actuated. Its center of gravity (CoG) and swimming direction can be changed respectively by placing external trimming weights. The weight blocks are easily reconnected to either sockets in the nose for vertical diving or to a rail on the

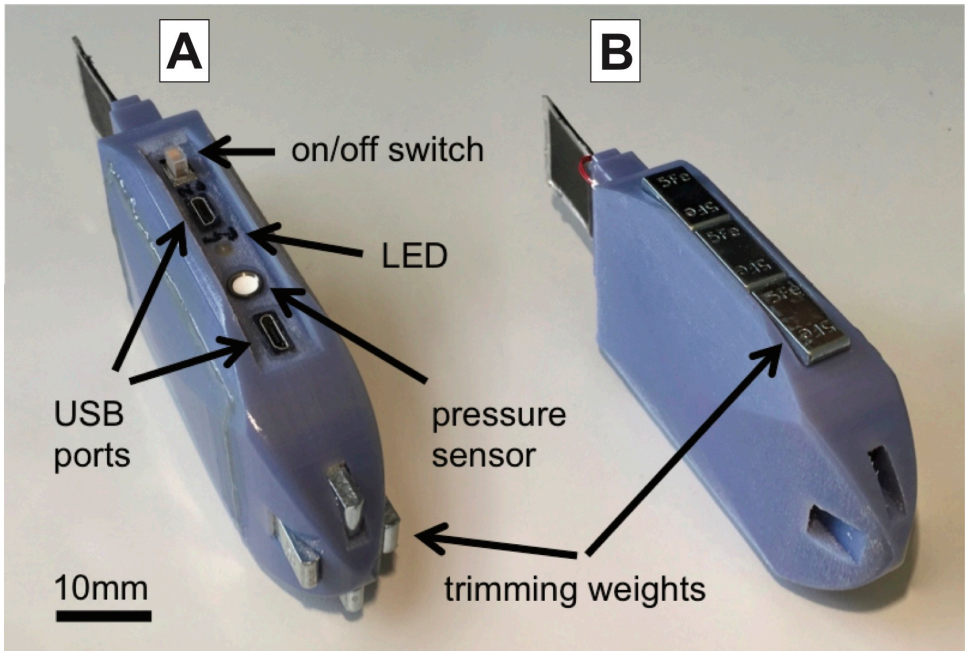


Figure 4.12: Swimming robot design

The reconfigurable robot driven by a soft fin made out of stacked dielectric elastomer actuators. **A**, Dorsal side. Diving configuration with all trimming weights placed on the nose. **B**, Ventral side. Planar swimming configuration with all trimming weights placed on the bottom of the robot.

ventral side for planar swimming. The weights are held in place by magnets mounted internally. The CoG is designed to be below the center of buoyancy in either configuration such that passive stability in pitch and roll is guaranteed.

The total component cost is around $300 of which the voltage converters account for 85 %. The assembly of one robot takes about four hours and includes soldering the circuitry using 36-gauge ultra-flexible wire, mounting the electronic components inside the body with liquid adhesive, waterproofing all penetrating components from the inside with instant epoxy, and finally sealing a lid on the side with plastic bonding epoxy.

4.8 Manuevers in planar swimming

Planar swimming experiments were carried out at the water surface. We placed the trimming weights at the robot's ventral side such that it swims forward in the horizontal direction. Straight line swimming was achieved by tuning the symmetry of the oscillation of the fin. The robot can swim circles of various radii when the oscillation is biased towards one side, e.g., by alternately switching on and off only one unimorph. A deliberately biased oscillation can be used to compensate for drift in order to swim exact trajectories.

4.9 Autonomous vertical diving

Vertical diving enhances the robot's performance from simply swimming on the surface (Figure 4.14). The robot was reconfigured for swimming in the vertical direction by moving the trimming weights to its nose. Altogether, the robot was slightly positively buoyant. The buoyancy made it rise to the surface when the fin was not active. An active fin made it dive in the vertical direction at a maximum rate of 0.3 BL/s (= 30 mm/s).

Our robot uses feedback from a pressure sensor to dive controllably. The

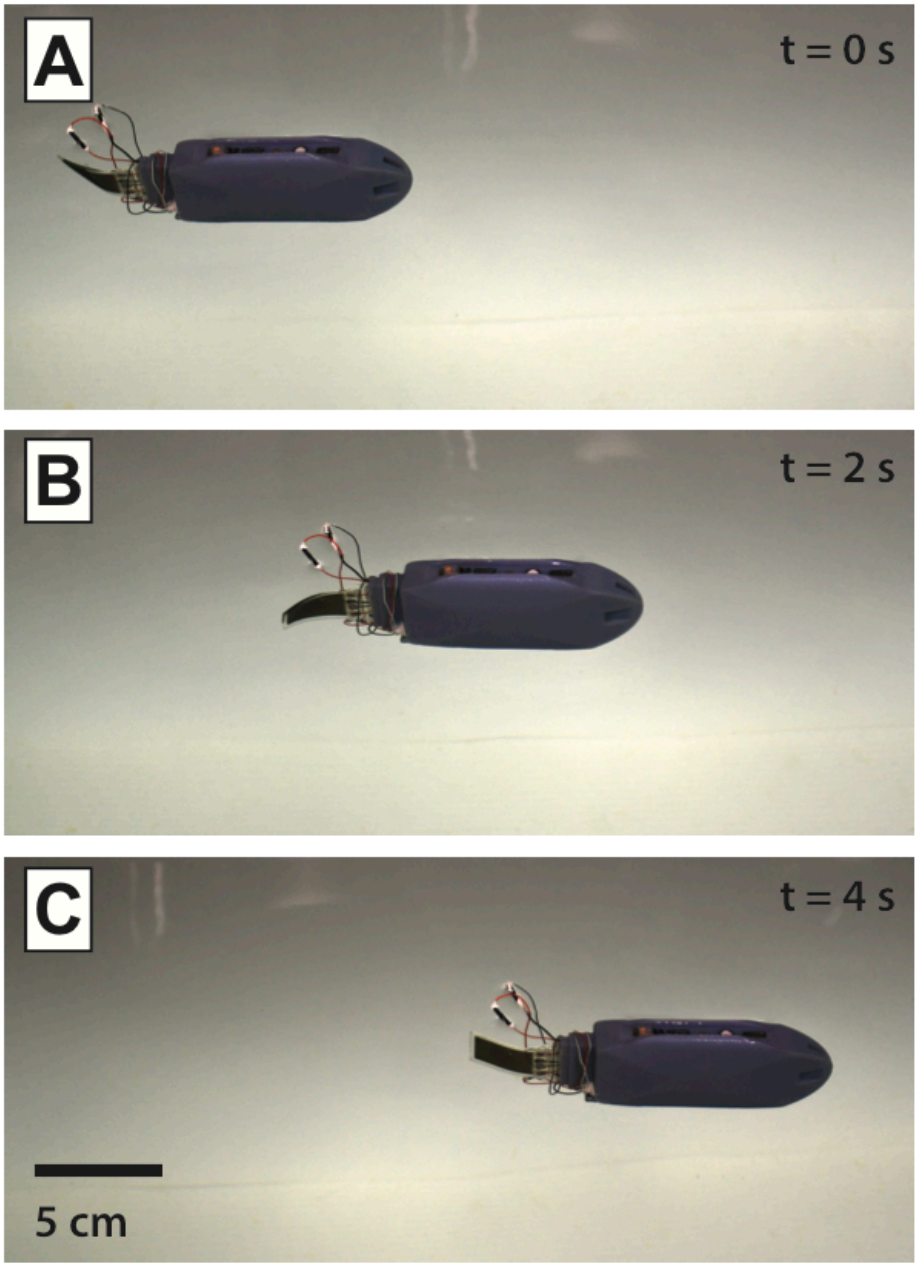


Figure 4.13: Horizontal swim demonstration

A,B,C, Untethered DEA-powered robot during an open-loop swimming experiment at three separate instances, showing a top speed of 0.55 body lengths per second or 55 mm/s.

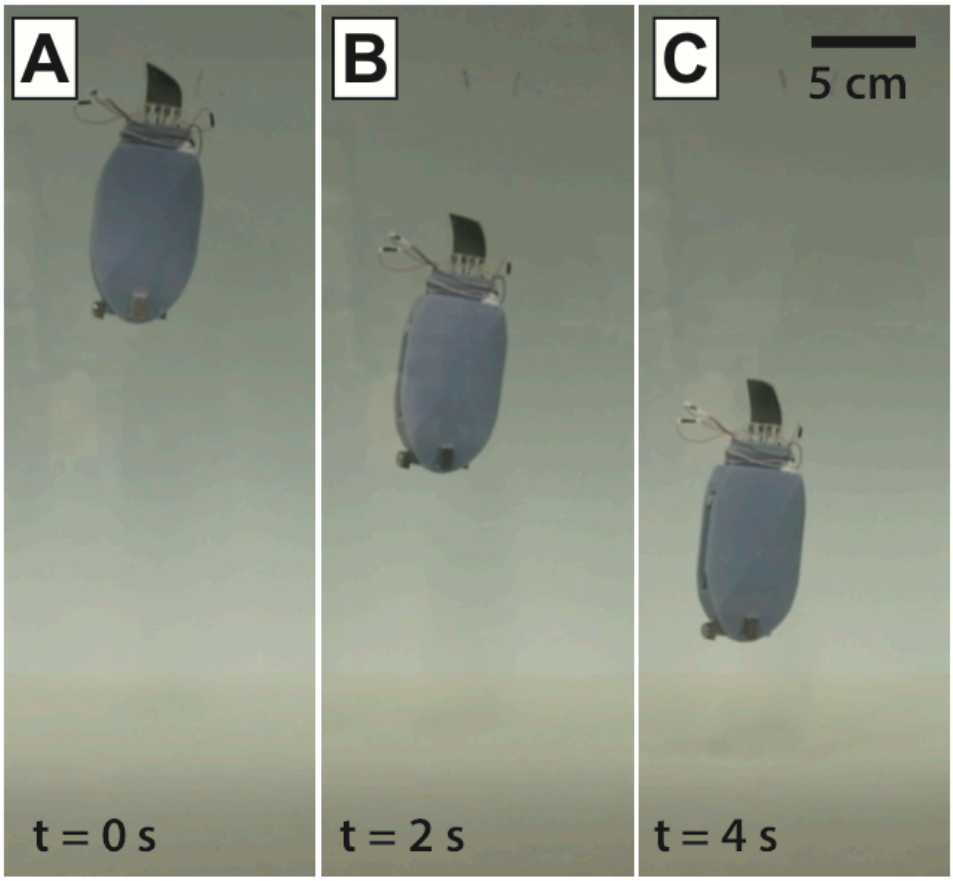


Figure 4.14: Vertical dive demonstration

A,B,C, Untethered DEA-powered robot during an open-loop vertical diving experiment at three separate instances, showing a top speed of 0.33 body lengths per second or 33 mm/s.

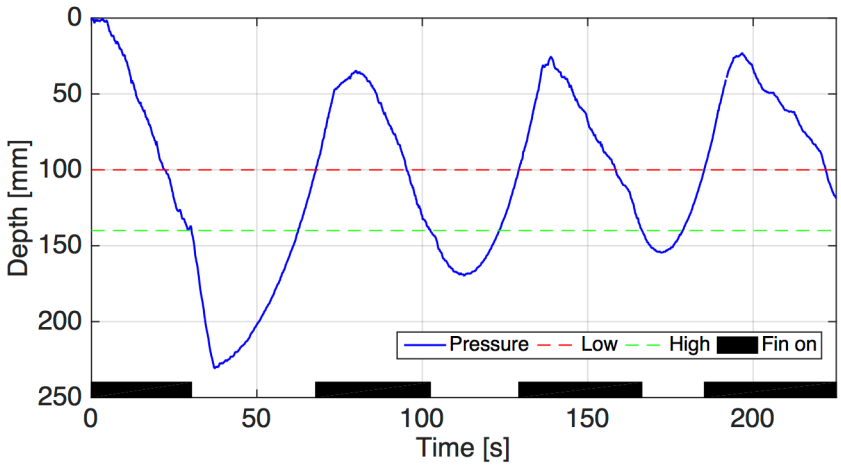


Figure 4.15: Autonomous dive depth control
Closed-loop periodic diving between target depths of 100 mm (low) and 140 mm (high). The solid blue line shows depth as sampled from the pressure sensor at 10 Hz. The black boxes indicate active periods of the fin.

robot's behavior is updated based on the feedback from a control loop running at 10 Hz. We demonstrated long-range repeatable diving between two thresholds set at 100 mm and 140 mm below an initial depth (Figure 4.15). The experiment showed significant overshoots caused by the robot's inertia, which could be reduced by applying predictive control strategies.

4.10 Power consumption

The average power consumption is approximately 0.75 W and allows for a robot runtime of more than 100 mins for a 17 layer fin operating at 2.2 Hz. The power consumption increases with the number of active layers per fin as they constitute a higher load.

An approximation of the output power of the robot is calculated by its speed times the measured thrust of the mounted fin. The maximum output power was 1.3 mW and results in an overall power efficiency of 0.17 %. We note that neither the robot nor the fin were optimized for efficient swimming.

4.11 Summary

We built active DEA-fins and measured their thrust forces in a standardized setup. Comparative experiments revealed that the thrust can be increased by stacking additional layers, at the expense of a higher risk of dielectric breakdown. The stiffness of the elastomer can be tuned by modifying the crosslinker concentration to reach peak thrust forces of up to 25 mN.

Our untethered underwater robot achieved a higher degree of autonomy than previous DEA-powered robots by using sensory feedback to update its behavior. The robot demonstrated free planar swimming with speeds of up to 0.55 BL/s (= 55 mm/s) and open-loop turning with radii of 1.2 BL/s (= 120 mm). It can be reconfigured with ease to also demonstrate closed-loop vertical diving at 0.3 BL/s (= 30 mm/s). The swimming performance was enabled by our modular DEA-fin and low footprint power circuitry.

Our results show that by careful selection of components, dielectric elastomer actuators can swim as fast as fluidic-powered actuators. The entire robot occupies a small footprint, comparable to those powered by IPMCs or SMAs, and the actuator fabrication is simple. Our DEAs are scalable in power output, as well as modular, soft, and waterproof. Their modularity allows us to mount multiple actuators on a single robot.

A key limitation of our current robot is the need for two voltage converters per DEA due to low voltage switching. In a future step, we envision a robot with several active fins that is capable of achieving high maneuverability. To this end, we plan to lower the actuation voltages to under 1.2 kV such that switching at high voltage becomes feasible with smaller components and one single voltage converter for several fins will be sufficient. Smaller, simpler, and more maneuverable robots could be implemented for studies of cooperative behavior. Overall, the multilayer bimorph actuators have been shown to overcome the issues due to on-board power (4), and autonomy (5). A different approach to overcoming the sixth limitation and achieving high power locomotion is described in the next chapter.

5

Latch-free dielectric elastomer actuator powered jumping robot

Animals at multiple scales make use of impulsive movements to escape predators[101], catch fast prey, or locomote more effciently[102]. Often, these biological systems make use of power amplification mechanisms to bypass the universal trade-off between force and velocity[103]. In short, the energy output of a muscle or actuator is used to deform a spring, which is held in place by a latch. When the latch is removed, the energy stored in the spring is released faster than the muscle or actuator can deform, increasing the power output of the system. The same principles have been employed in engineered systems to create robots capable of high jumps, an effective type of locomotion in unstructured environments[104]. Most jumping robots employ rigid actuators or motors to

store energy in a power-amplifying mechanism, including DC motors[105], shape memory alloys (SMAs)[106], and electrostatic inchworm motors[107].

Recent advances in fabrication and integration of soft robotic components have been adapted to create jumping systems. A bio-inspired approach uses pneumatic actuators as artificial muscles, while springs serve as the energy storing element[108]. To bypass the need for springs, a different approach uses combustion of ignitable gases to create large and rapid volume changes[109]. Some limitations of this approach can be addressed by 3D printing a gradient in stiffness across the robot body, from the soft deformable feet to the rigid chassis which encases the power electronics and fuel containers[14]. The same idea of using low viscoelasticity silicone elastomers as the energy storing spring, can be employed at smaller scales[110]. A hybrid approach uses flexible SMA coils to deform a soft, elastomeric body, to cause jumping[111] or caterpillar-inspired, ballistic rolling[112]. From all of these examples we extract two valuable concepts: that soft elastomers can be used as energy-storing springs, and that having an electrically powered actuator simplifies the robot design, bypassing the need for pumps or ignition mechanisms.

We propose to build a jumping robot driven by a dielectric elastomer actuator which uses the elastomer as a mechanical energy storage element. With the exception of a limited hop[113], DEAs have never been used to power jumping robots because of either low energy density, or slow response speed. Our material and fabrication advances have enabled multilayer actuators which deform without pre-stretch and exhibit energy density on par with natural muscles. The remaining challenge for building a jumping robot is to create a power amplification mechanism that allows the DEA to rapidly release the mechanical energy stored when actuated.

To build a simple power amplification mechanism we examined how conventional DEAs are made and found a simple solution. Most DEAs are made by pre-stretching an elastomer and attaching it to a rigid frame. The motivation is to increase the range of deformation, as well as the breakdown strength[35]. Some approaches use flexible frames set at a specific minimum energy state, as

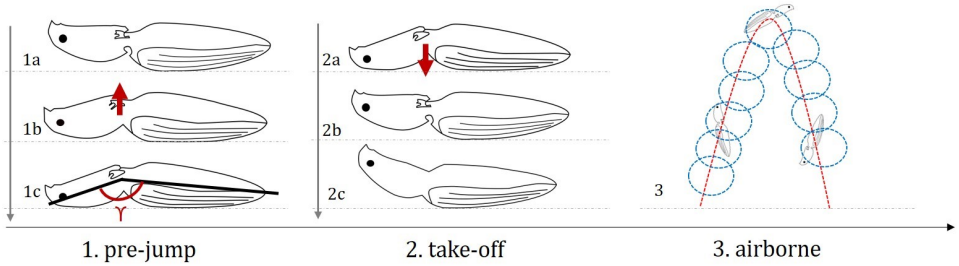


Figure 5.1: Click beetle jumping mechanism. Schematic of the jumping mechanism employed by a click beetle to invert its body relative to the ground. The image is reproduced from [117].

well as a deformation path for the DEA between the actuated and unactuated states[114]. One advantage to this approach is the ability to shuttle mechanical energy from the elastomer to the frame and back depending on the level of strain in the elastomer.

5.1 Biological inspiration

While most animals rely on legs for jumping[115], some unique insects and plants use deformations in their body to accomplish the same task. The jump of the click beetle [116], as described in Figure 5.1, is caused by flexing of the body relative to a hinge between the proto- and mesothorax[117]. In this case, the prothorax is the smaller part of the body, on the left side of the image in Figure 5.1. The prothorax moves relative to the larger and heavier mesothorax, which is on the right side of the body. The difference in masses between the two main body sections create angular momentum, which causes somersaulting maneuvers. From an initially inverted position, click beetles jack-knife their body to catapult themselves into the air and land back on their feet. This unique solution decouples the self-righting attributes (body and hinge,) from any other locomotion features (legs, wings).

An alternative jump mechanism which does not rely on legs is exhibited by

Esquietum spores[118]. Jumps occur when the spores suddenly release stored mechanical energy from structures named elaters. An elater is a cell (or structure attached to a cell) that is hygroscopic, and therefore will change shape in response to changes in moisture in the environment. In this case, the elaters store mechanical energy by being tightly folded as shown in Figure 5.2. For a population of spores, the large jumps result in a very efficient dispersal which allows the spores to cover a wider area, leading to an evolutionary advantage. From these two examples we imagine a simple cantilever robot which can rapidly transition between its bent and flat configurations, leading to jumping locomotion. The relative energy states are explored in the next section.

5.2 Fabrication

The multilayering process[57] was adapted to make actuator strips of a prescribed form factor, in most cases 5 cm by 1 cm. The elastomer of choice was CN9018 with 7.5% HDDA crosslinker. The reasons for selecting this elastomer were the following: it has a Young's modulus comparable to natural muscle (300 kPa), can sustain strains of 50% its initial length without breaking, which allows for large amounts of mechanical energy to be stored in the frame by pre-stretching. The adhesive used to bond the elastomer to the rigid frame was CN9018 with 0% HDDA crosslinker. The areal densities of electrodes were all below 15.59 μL/cm^2 to minimize the likelihood of dielectric breakdown at high applied electric fields. The completed and cured elastomer strips were then stretched and adhered to a rigid material frame, as described in Fig. 5.3. The material and geometric parameters used are listed in Table 5.1.

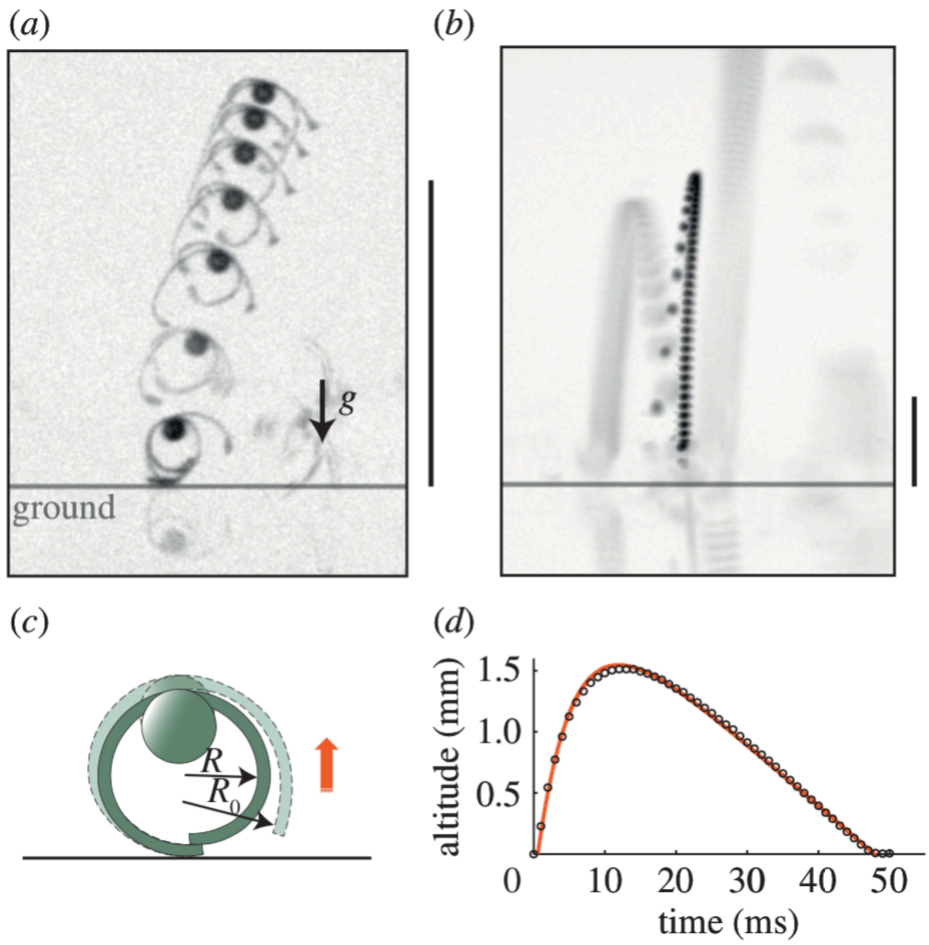


Figure 5.2: Spore jumping . An alternative biological jumping system reproduced from [118]. (a) Superposition of images immediately after the jump with an interval of 0.57 ms. The take-off velocity is 0.35 m/s. (b) Larger view with images taken every 1 ms. The take-off velocity is 0.4 m/s for the jump in the middle and 0.8 m/s for the jump starting on the right. On both images, the scale bar is 500 μm and the ground position is indicated by an horizontal line. (c) Jumping mechanism of a spore (only two elaters are drawn). Elaters can be stuck by friction. The released elaters, when stresses overcome static friction, are drawn with dashes. (d) The altitude of the spore (middle trajectory of figure 4b showing a dark spore). Circles represent measurements, and the line represents the model prediction with an initial velocity of 0.41 m/s and a drag radius of 21.2 μm.

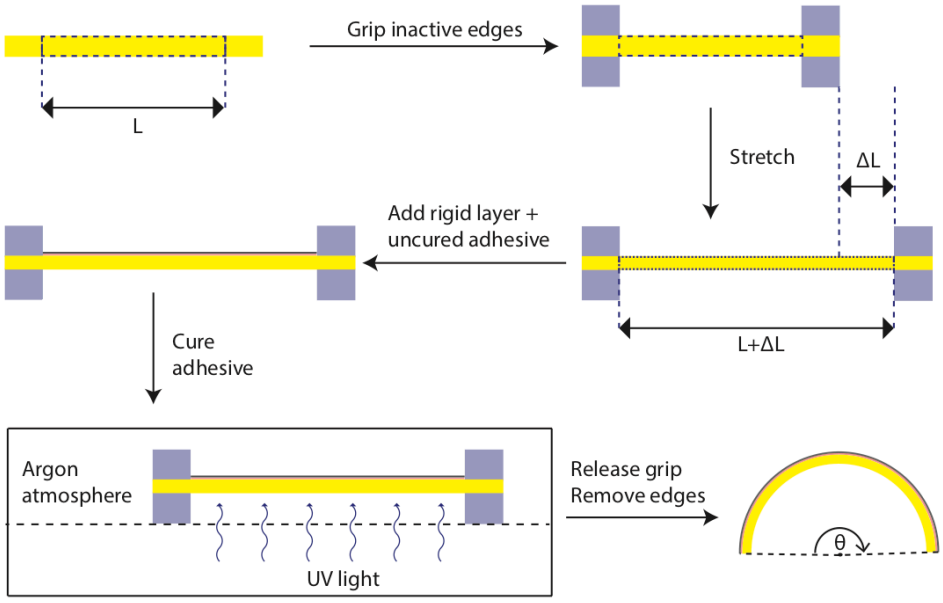


Figure 5.3: Fabrication of pre-stretched structure. The multilayer elastomer actuator starts in a relaxed state. We grip the inactive edges and apply the desired strain level to the elastomer. With the elastomer still in the strained state we apply uncured adhesive and a rigid frame to one side of the elastomer. After curing the adhesive, the grips are removed and the inactive sections are cut which leads to a curved elastomer-frame minimum energy structure. The angle θ corresponds to the bend angle of the frame.

Table 5.1: Material and geometric parameters for the modeled jumper.

Parameter	Value	Units
l	5	cm
w	1	cm
t_e	1	mm
t_f	0.3	mm
Y_e	0.3	MPa
Y_f	2000	MPa
N	10	layers

5.3 Modeling the mechanical and electrical energy stored in the DEA

In our model, we input mechanical energy by pre-stretching elastomer, then release the system causing most of that energy to be transferred into bending the frame. When electrical energy is then added by applying voltage, the frame returns to the flat state. In a simple approximation, the elastomer pre-strain and applied voltage are inputs, and the frame bending angle is an output. The mechanical energy of the strained elastomer can be modeled as:

$$u_{mech} = \frac{s^2 Y_e l^2 w t_e}{2} \tag{5.1}$$

where s is the applied strain to the elastomer, Y_e is the Young's modulus of the elastomer, l is the length of the elastomer, w is the width of the elastomer, t_e is the thickness of the elastomer, and ρ is the density of the elastomer. With respect to Figure 5.4, $s = \frac{\delta l}{l}$ and $L = \delta l + l$.

The rigid frame to which the elastomer is attached is considered too stiff to undergo appreciable strain. Instead, the frame can store mechanical energy via bending. The bending energy in the frame is:

$$u_{bending} = \frac{Y_f w t_f^3}{24L}\Theta^2 \tag{5.2}$$

where Y_f is the Young's modulus of the frame, w is the width of the frame, t_f is the thickness of the frame, L is the length of the frame and Θ is the bending angle.

Lastly, the applied electric field across the elastomer causes a Maxwell stress which leads to strain in the elastomer. The applied electrical energy can be described by

$$u_{electrical} = -\frac{CV^2}{2} = -\frac{N^2 \varepsilon w L V^2}{2t_e} \tag{5.3}$$

where C is the capacitance of the DEA and V is the applied voltage on the DEA. Given that the DEAs are multilayer parallel plate capacitors, the capacitance is

equal to $C = \frac{N^2 \varepsilon \times w \times L}{t_e}$, where w is the width of the DEA, L is the length of the elastomer, N is the number of layers, and t_e is the thickness of the elastomer. For simplicity, we made frame and elastomer have the same aspect ratio (5 to 1) and dimensions.

The energy balance in the system is given by

$$u_{total} = u_{mech} + u_{electrical} + u_{bending} \tag{5.4}$$

Using material parameters from Table 5.1, we modeled a specific system (elastomer made with 7.5% HDDA crosslinker and PETG frame), shown in Figure 5.4, and used these parameters for the demonstration in Section 5.5.

5.4 Power amplification

In addition to storing mechanical energy density by bending, the frame also increases the speed with which the energy is released. Given the simple construction and geometry, the elastomer and frame structure can be considered to be a two material cantilever. To a first degree, the response speed can be taken to be proportional to the first frequency of vibration of the cantilever. From [119] we know that the ratio of the frequency of vibration of the bimaterial cantilever and frequency of the elastomer-only cantilever can be estimted as

$$\left(\frac{f_{bim}}{f_e}\right)^2 = \left[\frac{(1 + E_r h_r)(1 + E_r h_r^3) + 3E_r h_r (1 + h_r)^2}{(1 + \rho_r h_r)(1 + E_r h_r)}\right] \tag{5.5}$$

where $E_r = \frac{Y_f}{Y_e}$, is the ratio of the Young's moduli of the frame and elastomer, respectively, $h_r = \frac{t_f}{t_e}$ is the ratio of the thicknesses of the frame and elastomer, respectively, and ρ_r is the ratio of the densities of the frame and elastomer, respectively. For the case modeled in Figure 5.4, the ratios are as follows: $E_r = \frac{210^9}{310^5} = 20,000$, $h_r = \frac{0.0003}{0.001} = 0.3$ and $\rho_r = 1$. The resulting boost in frequency is $\frac{f_{bim}}{f_e} = 12$, meaning the energy can be released $12\times$ faster because of the addition of a rigid frame.

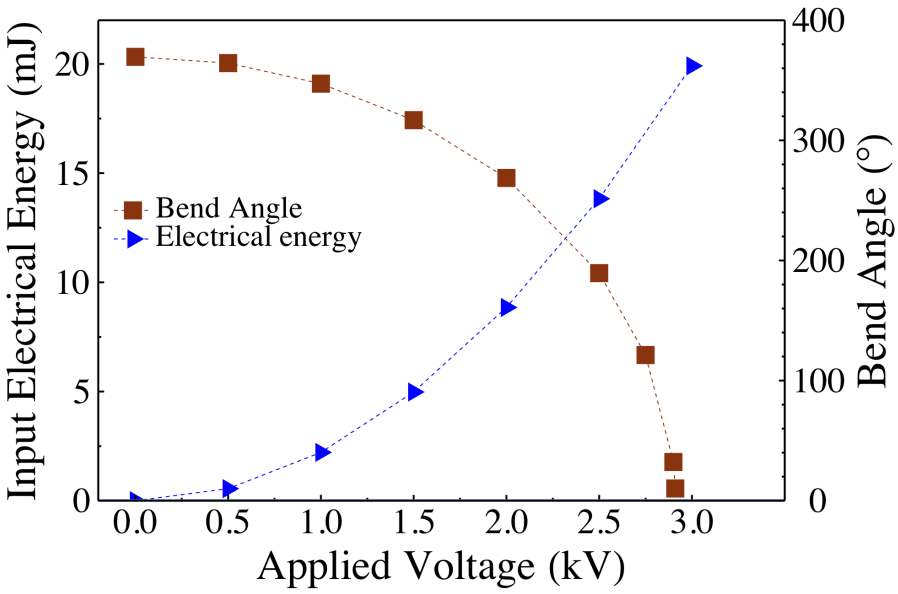


Figure 5.4: Energy states in pre-stretched structure. Dependence of the electrical energy input into the system as a function of applied voltage (left y-axis). The elastomer had been pre-stretched 30% of its initial length before attaching the frame. Dependence of the bend angle of the composite structure on the applied voltage in the system (right y-axis). The applied voltage allows the structure to switch between two states: circular beam at 0 kV and flat beam at 3kV.

5.5 Demonstrations

Using the model guidance we fabricated a DEA-frame composite structure, with the goal of demonstrating a successful jump. To date, there have been no successful demonstrations of DEA robots which can jump to a height greater than a body length. To record the deformation of the DEA jumper we used a high speed camera. The camera was a Phantom v7.3 from Vision Research, Wayne, NJ. The images were captured at 6,688 frames per second, corresponding to a resolution of 800 $\times$ 600 pixels. The actuator was made as described in Section 5.3, and powered to 8 kV using a high voltage amplifier (Trek, Lockport, NY). From its fully charged state the actuator was discharged at 10 mA, the maximum current allowed by the high voltage power supply. The captured images in Figure 5.5 show that the robot is able to complete a jump of approximately one body length in less than 0.2 seconds.

The potential energy in the jumping robot can be estimated from its weight and maximum height reached. In the example in Figure 5.5 the robot reaches a height of $h = 5$cm for a weight of $w = 2$g. The potential energy at the peak of the jump is

$$u_{pot} = mgh = 2g \times 9.8m/s^2 \times 5cm = 0.98mJ \tag{5.6}$$

Therefore the power released during the jump corresponds to the ratio of energy to the release time, in this case taken to be 22 ms, from when the capacitor is discharged to when it reaches its relaxed state configuration. Accordingly, the power in the system is estimated to be 44.5 mW, and the specific power of the robot is 22.5 W/kg. By comparison, the click beetle has a much higher specific power (0.8-1.8 kW/kg), for jumps which are close in duration (0.53 s)[120], suggesting that the robot could be further improved for greater jumping performance. In terms of efficiency, most of the energy stored in bending the frame (1.11 mJ) is transferred as kinetic energy used for jumping (88% efficiency). However, the electro-mechanical energy efficiency is low, as the

actuator requires 8 kV to deform, meaning more than 400 mJ of electrical energy are needed for 1 mJ of mechanical work.

5.6 Next steps

Considering the click beetle inspiration, we expect that future DEA-powered jumpers can perform controlled body inversions on demand. One requirement for such a taks is that weight be distributed appropriately evenly across the body. In the click beetle case the meso-thorax is approximately 4× larger than the proto-thorax which biases the rotation of the beetle during the jump.

In addition, we expect such robots to be capable of multi-modal locomotion, alternating between low power crawling, similar to [70], and high power jumping when required by the environment. Another significant demonstration would be untethered jumping, provided we can find or build components for a lightweight power supply. Lastly, the robot may become a useful tool to study biology to better understand the energy and ground contact requirements for other impulsive systems.

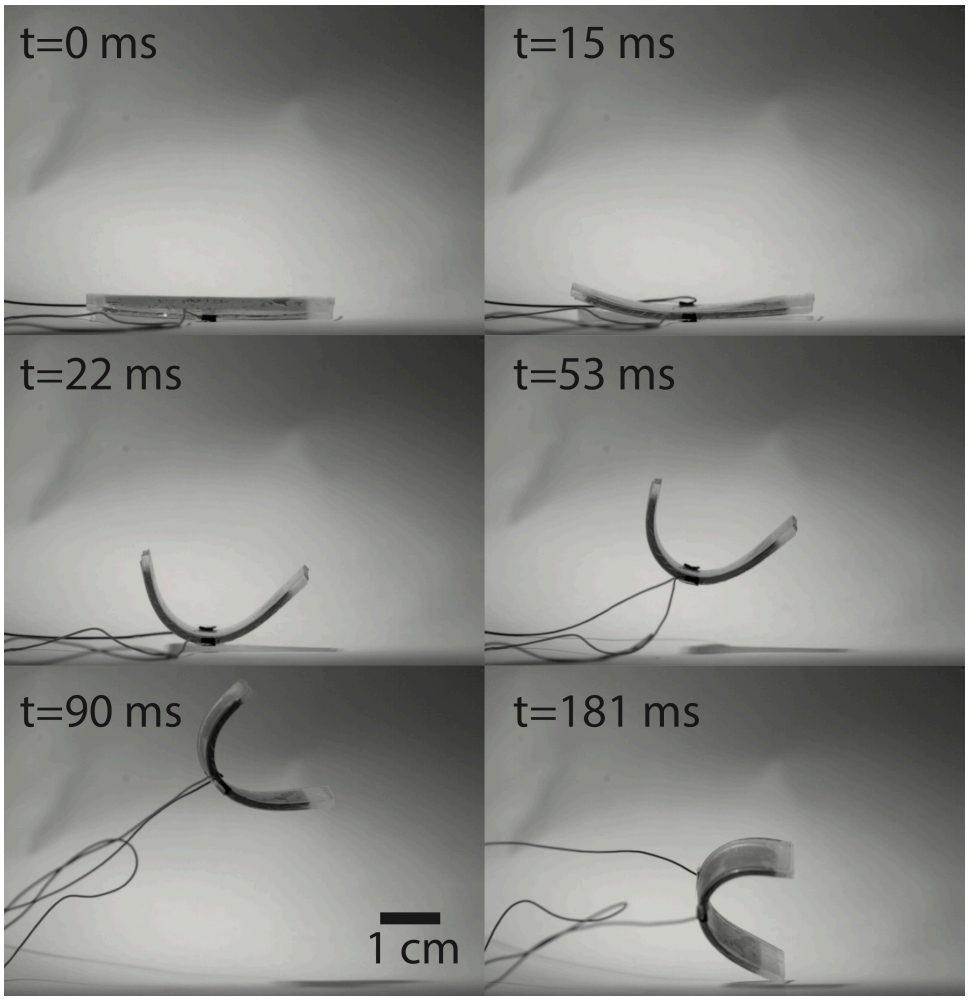


Figure 5.5: Jump demonstration. Six instances throughout the jump of a DEA powered robot. The entire jump between when the capacitor is discharged and the robot makes contact again with the ground takes less than 0.2 seconds.

6

Conclusions

This thesis has described a versatile approach to build dielectric elastomer actuators, selected material and processing conditions for enhanced performance, and demonstrated locomotion in multiple robotic systems. This final chapter discusses potential directions for further development. The most significant acheivement has been the creation of a multilayer device platform in which material improvements (elastomers with lower viscoelastic losses, electrodes with higher conductivity, etc.) can be readily translated into compelling advances in robotic components (high energy density, large bandwidth, impulsive behavior, etc.).

6.1 Multilayer process and materials

The method described in Chapter 2 has been proven a versatile tool to build bending, contracting, and expanding actuators. With careful control over electrode placement, more complex deformations can be achieved, bypassing the need for additional rigid components[121].

The main limitations come from trade-offs in performance, particularly between high energy density and response time of the actuator. As demonstrated in recent work, the response speed of the actuator can be increased significantly, by using materials with smaller viscoelastic losses, such as silicones[49]. However, to match the power density of natural muscles, these actuators must be able to also sustain high applied electric fields. A potential solution would be to make electrodes as blends of nanoscale conductors, using both silver nanowires (AgNWs) and carbon nanotubes[76]. The higher electrical conductivity of the AgNWs would allow for lower RC constants, and improve the energy efficiency of the DEA, provided the material can still sustain high applied electric fields.

6.2 Robotic demonstrations

While crawling, swimming, and jumping are all compelling demonstrations, more work is needed to ensure DEAs are easy to integrate into more complex robots. The actuation voltage needs to be reduced further, to allow smaller and lighter power supplies to be used. Part of this effort will need to be focused on fabrication techniques, in particular with respect to making uniform, large area elastomers in repeatable fashion. For acrylic-based DEAs, integration by adhesion with other components is easy, as shown in Chapter 5. For silicone-based DEAs, more work is needed to ensure robust bonds can be made with other, in particular, rigid components.

With strong actuators available, the next steps should be integration of sensing, and potentially computation. The multilayer process could be adapted to allow for some layers to operate as capacitive or resistive strain sensors, allowing the

actuators to be operated closed-loop. Building on existing work on DEA-based logic[81], and using more exotic semiconducting carbon nanotube electrodes, parts of the multilayer DEA could be made into logic components. By tuning the material composition and geometry of the multilayer, the entire device could operate as a smart composite, fully capable of sensing, computation, and actuation.

References

[1] Koichi Suzumori. Elastic materials producing compliant robots. *Robotics and Autonomous systems*, 18(1-2):135–140, 1996.

[2] Koichi Suzumori, Satoshi Endo, Takefumi Kanda, Naomi Kato, and Hiroyoshi Suzuki. A bending pneumatic rubber actuator realizing soft-bodied manta swimming robot. In *Robotics and Automation, 2007 IEEE International Conference on*, pages 4975–4980. IEEE, 2007.

[3] Dian Yang, Mohit S Verma, Ju-Hee So, Bobak Mosadegh, Christoph Keplinger, Benjamin Lee, Fatemeh Khashai, Elton Lossner, Zhigang Suo, and George M Whitesides. Buckling pneumatic linear actuators inspired by muscle. *Advanced Materials Technologies*, 1(3):1600055, 2016.

[4] Stephen A Morin, Robert F Shepherd, Sen Wai Kwok, Adam A Stokes, Alex Nemiroski, and George M Whitesides. Camouflage and display for soft machines. *Science*, 337(6096):828–832, 2012.

[5] Michael T Tolley, Robert F Shepherd, Michael Karpelson, Nicholas W Bartlett, Kevin C Galloway, Michael Wehner, Rui Nunes, George M Whitesides, and Robert J Wood. An untethered jumping soft robot. In *Intelligent Robots and Systems (IROS 2014), 2014 IEEE/RSJ International Conference on*, pages 561–566. IEEE, 2014.

[6] Robert F Shepherd, Filip Ilievski, Wonjae Choi, Stephen A Morin, Adam A Stokes, Aaron D Mazzeo, Xin Chen, Michael Wang, and George M Whitesides. Multigait soft robot. *Proceedings of the national academy of sciences*, 108(51):20400–20403, 2011.

[7] Takuya Umedachi, Vishesh Vikas, and Barry A Trimmer. Highly deformable 3-d printed soft robot generating inching and crawling locomotions with variable friction legs. In *Intelligent Robots and Systems*

(IROS), 2013 IEEE/RSJ International Conference on, pages 4590–4595. IEEE, 2013.

[8] Sheila Russo, Tommaso Ranzani, Conor J Walsh, and Robert J Wood. An additive millimeter-scale fabrication method for soft biocompatible actuators and sensors. *Advanced Materials Technologies*, 2(10):1700135, 2017.

[9] Joseph T Muth, Daniel M Vogt, Ryan L Truby, Yiğit Mengüç, David B Kolesky, Robert J Wood, and Jennifer A Lewis. Embedded 3d printing of strain sensors within highly stretchable elastomers. *Advanced Materials*, 26(36):6307–6312, 2014.

[10] Sungwon Lee, Amir Reuveny, Jonathan Reeder, Sunghoon Lee, Hanbit Jin, Qihan Liu, Tomoyuki Yokota, Tsuyoshi Sekitani, Takashi Isoyama, Yusuke Abe, et al. A transparent bending-insensitive pressure sensor. *Nature nanotechnology*, 11(5):472, 2016.

[11] Ryan L Truby, Michael Wehner, Abigail K Grosskopf, Daniel M Vogt, Sebastien GM Uzel, Robert J Wood, and Jennifer A Lewis. Soft robotics: Soft somatosensitive actuators via embedded 3d printing (adv. mater. 15/2018). *Advanced Materials*, 30(15):1870106, 2018.

[12] Michael Wehner, Ryan L Truby, Daniel J Fitzgerald, Bobak Mosadegh, George M Whitesides, Jennifer A Lewis, and Robert J Wood. An integrated design and fabrication strategy for entirely soft, autonomous robots. *Nature*, 536(7617):451, 2016.

[13] Michael T Tolley, Robert F Shepherd, Bobak Mosadegh, Kevin C Galloway, Michael Wehner, Michael Karpelson, Robert J Wood, and George M Whitesides. A resilient, untethered soft robot. *Soft robotics*, 1(3):213–223, 2014.

[14] Nicholas W Bartlett, Michael T Tolley, Johannes TB Overvelde, James C Weaver, Bobak Mosadegh, Katia Bertoldi, George M Whitesides, and Robert J Wood. A 3d-printed, functionally graded soft robot powered by combustion. *Science*, 349(6244):161–165, 2015.

[15] H Okuzaki, H Suzuki, and T Ito. Electrically driven pedot/pss actuators. *Synthetic Metals*, 159(21-22):2233–2236, 2009.

[16] Carter S Haines, Márcio D Lima, Na Li, Geoffrey M Spinks, Javad Foroughi, John DW Madden, Shi Hyeong Kim, Shaoli Fang, Mônica Jung de Andrade, Fatma Göktepe, et al. Artificial muscles from fishing line and sewing thread. *science*, 343(6173):868–872, 2014.

[17] Alex Villanueva, Colin Smith, and Shashank Priya. A biomimetic robotic jellyfish (robojelly) actuated by shape memory alloy composite actuators. *Bioinspiration & biomimetics*, 6(3):036004, 2011.

[18] Duncan J Maitland, Melodie F Metzger, Daniel Schumann, Abraham Lee, and Thomas S Wilson. Photothermal properties of shape memory polymer micro-actuators for treating stroke. *Lasers in Surgery and Medicine: The Official Journal of the American Society for Laser Medicine and Surgery*, 30(1):1–11, 2002.

[19] Menake E Piyasena, Robert Newby, Thomas J Miller, Benjamin Shapiro, and Elisabeth Smela. Electroosmotically driven microfluidic actuators. *Sensors and Actuators B: Chemical*, 141(1):263–269, 2009.

[20] Ron Pelrine, Roy Kornbluh, and Guggi Kofod. High-strain actuator materials based on dielectric elastomers. *Advanced Materials*, 12(16):1223–1225, 2000.

[21] Ron Pelrine, Roy Kornbluh, Qibing Pei, and Jose Joseph. High-speed electrically actuated elastomers with strain greater than 100%. *Science*, 287(5454):836–839, 2000.

[22] Samuel Shian, Katia Bertoldi, and David R Clarke. Dielectric elastomer based "grippers" for soft robotics. *Advanced Materials*, 27(43):6814–6819, 2015.

[23] G Kovacs, L Düring, S Michel, and G Terrasi. Stacked dielectric elastomer actuator for tensile force transmission. *Sensors and actuators A: Physical*, 155(2):299–307, 2009.

[24] Arun Rajamani, Michael D Grissom, Christopher D Rahn, and Qiming Zhang. Wound roll dielectric elastomer actuators: fabrication, analysis, and experiments. *IEEE/ASME Transactions On Mechatronics*, 13(1):117–124, 2008.

[25] Tiefeng Li, Guorui Li, Yiming Liang, Tingyu Cheng, Jing Dai, Xuxu Yang, Bangyuan Liu, Zedong Zeng, Zhilong Huang, Yingwu Luo, et al. Fast-moving soft electronic fish. *Science Advances*, 3(4):e1602045, 2017.

[26] Jiawei Cao, Lei Qin, Jun Liu, Qinyuan Ren, Choon Chiang Foo, Hongqiang Wang, Heow Pueh Lee, and Jian Zhu. Untethered soft robot capable of stable locomotion using soft electrostatic actuators. *Extreme Mechanics Letters*, 21:9–16, 2018.

[27] Xuanhe Zhao and Zhigang Suo. Method to analyze electromechanical stability of dielectric elastomers. *Applied Physics Letters*, 91(6):061921, 2007.

[28] Samuel Shian, Katia Bertoldi, and David R Clarke. Use of aligned fibers to enhance the performance of dielectric elastomer inchworm robots. In *Electroactive Polymer Actuators and Devices (EAPAD) 2015*, volume 9430, page 94301P. International Society for Optics and Photonics, 2015.

[29] Robert J Full and Kenneth Meijer. Metrics of natural muscle function. *Chapter*, 3:73–89, 2001.

[30] Jun Shintake, Samuel Rosset, Bryan E Schubert, Dario Floreano, and Herbert R Shea. A foldable antagonistic actuator. *IEEE/ASME Transactions on Mechatronics*, 20(5):1997–2008, 2015.

[31] Iain A Anderson, Emilio P Calius, Todd Gisby, Thom Hale, Thomas McKay, Benjamin O'Brien, and Scott Walbran. A dielectric elastomer actuator thin membrane rotary motor. In *Electroactive Polymer Actuators and Devices (EAPAD) 2009*, volume 7287, page 72871H. International Society for Optics and Photonics, 2009.

[32] Kwangmok Jung, Ja Choon Koo, Young Kwan Lee, Hyouk Ryeol Choi, et al. Artificial annelid robot driven by soft actuators. *Bioinspiration & biomimetics*, 2(2):S42, 2007.

[33] Luc Maffli, Samuel Rosset, Michele Ghilardi, Federico Carpi, and Herbert Shea. Ultrafast all-polymer electrically tunable silicone lenses. *Advanced Functional Materials*, 25(11):1656–1665, 2015.

[34] Canh Toan Nguyen, Hoa Phung, Tien Dat Nguyen, Choonghan Lee, Uikyum Kim, Donghyouk Lee, Hyungpil Moon, Jachoon Koo,

Hyouk Ryeol Choi, et al. A small biomimetic quadruped robot driven by multistacked dielectric elastomer actuators. *Smart Materials and Structures*, 23(6):065005, 2014.

[35] Guggi Kofod. The static actuation of dielectric elastomer actuators: how does pre-stretch improve actuation? *Journal of Physics D: Applied Physics*, 41(21):215405, 2008.

[36] Xuanhe Zhao and Zhigang Suo. Theory of dielectric elastomers capable of giant deformation of actuation. *Physical review letters*, 104(17):178302, 2010.

[37] Soon M Ha, Wei Yuan, Qibing Pei, Ron Pelrine, and Scott Stanford. Interpenetrating polymer networks for high-performance electroelastomer artificial muscles. *Advanced Materials*, 18(7):887–891, 2006.

[38] Xiaofan Niu, Hristiyan Stoyanov, Wei Hu, Ruby Leo, Paul Brochu, and Qibing Pei. Synthesizing a new dielectric elastomer exhibiting large actuation strain and suppressed electromechanical instability without prestretching. *Journal of Polymer Science Part B: Polymer Physics*, 51(3):197–206, 2013.

[39] Jean-Sébastien Plante and Steven Dubowsky. Large-scale failure modes of dielectric elastomer actuators. *International journal of solids and structures*, 43(25-26):7727–7751, 2006.

[40] Alexandre Poulin, Samuel Rosset, and Herbert R Shea. Printing low-voltage dielectric elastomer actuators. *Applied Physics Letters*, 107(24):244104, 2015.

[41] Samuel Rosset and Herbert R Shea. Flexible and stretchable electrodes for dielectric elastomer actuators. *Applied Physics A*, 110(2):281–307, 2013.

[42] OA Araromi, AT Conn, CS Ling, JM Rossiter, R Vaidyanathan, and SC Burgess. Spray deposited multilayered dielectric elastomer actuators. *Sensors and Actuators A: Physical*, 167(2):459–467, 2011.

[43] Peter Lotz, Marc Matysek, and Helmut F Schlaak. Fabrication and application of miniaturized dielectric elastomer stack actuators. *IEEE/ASME Transactions on mechatronics*, 16(1):58–66, 2011.

[44] Wei Yuan, LB Hu, ZB Yu, Tuling Lam, James Biggs, Soon M Ha, DJ Xi, Bin Chen, Matthew K Senesky, George Grüner, et al. Fault-tolerant dielectric elastomer actuators using single-walled carbon nanotube electrodes. *Advanced Materials*, 20(3):621–625, 2008.

[45] Samuel Shian, Roger M Diebold, Alena McNamara, and David R Clarke. Highly compliant transparent electrodes. *Applied Physics Letters*, 101(6):061101, 2012.

[46] Federico Carpi, Iain Anderson, Siegfried Bauer, Gabriele Frediani, Giuseppe Gallone, Massimiliano Gei, Christian Graaf, Claire Jean-Mistral, William Kaal, Guggi Kofod, et al. Standards for dielectric elastomer transducers. *Smart Materials and Structures*, 24(10):105025, 2015.

[47] Samuel Shian, Roger M Diebold, and David R Clarke. Tunable lenses using transparent dielectric elastomer actuators. *Optics express*, 21(7):8669–8676, 2013.

[48] Federico Carpi, Gabriele Frediani, Simona Turco, and Danilo De Rossi. Optics: Bioinspired tunable lens with muscle-like electroactive elastomers (adv. funct. mater. 21/2011). *Advanced Functional Materials*, 21(21):4002–4002, 2011.

[49] Huichan Zhao, Aftab M Hussain, Mihai Duduta, Daniel M Vogt, Robert J Wood, and David R Clarke. Compact dielectric elastomer linear actuators. *Advanced Functional Materials*, 28(42):1804328, 2018.

[50] Michael Karpelson, Gu-Yeon Wei, and Robert J Wood. Milligram-scale high-voltage power electronics for piezoelectric microrobots. In *Robotics and Automation, 2009. ICRA'09. IEEE International Conference on*, pages 2217–2224. IEEE, 2009.

[51] Michael Karpelson, Gu-Yeon Wei, and Robert J Wood. Driving high voltage piezoelectric actuators in microrobotic applications. *Sensors and actuators A: Physical*, 176:78–89, 2012.

[52] Martin Kaltenbrunner, Tsuyoshi Sekitani, Jonathan Reeder, Tomoyuki Yokota, Kazunori Kuribara, Takeyoshi Tokuhara, Michael Drack, Reinhard Schwödiauer, Ingrid Graz, Simona Bauer-Gogonea, et al. An ultra-lightweight design for imperceptible plastic electronics. *Nature*, 499(7459):458, 2013.

[53] Iain A Anderson, Thom Hale, Todd Gisby, Tokushu Inamura, Thomas McKay, Benjamin O'Brien, Scott Walbran, and Emilio P Calius. A thin membrane artificial muscle rotary motor. *Applied Physics A*, 98(1):75, 2010.

[54] Mihai Duduta, Robert J Wood, and David R Clarke. Flexible, stretchable electroadhesives based on acrylic elastomers. In *Electroactive Polymer Actuators and Devices (EAPAD) 2016*, volume 9798, page 97981D. International Society for Optics and Photonics, 2016.

[55] Guang-Zhong Yang, Jim Bellingham, Pierre E Dupont, Peer Fischer, Luciano Floridi, Robert Full, Neil Jacobstein, Vijay Kumar, Marcia McNutt, Robert Merrifield, et al. The grand challenges of science robotics. *Science Robotics*, 3(14):eaar7650, 2018.

[56] R McN Alexander and HC Bennet-Clark. Storage of elastic strain energy in muscle and other tissues. *Nature*, 265(5590):114–117, 1977.

[57] Mihai Duduta, Robert J Wood, and David R Clarke. Multilayer dielectric elastomers for fast, programmable actuation without prestretch. *Advanced Materials*, 28(36):8058–8063, 2016.

[58] Federico Carpi, Siegfried Bauer, and Danilo De Rossi. Stretching dielectric elastomer performance. *Science*, 330(6012):1759–1761, 2010.

[59] Federico Carpi, Claudio Salaris, and Danilo De Rossi. Folded dielectric elastomer actuators. *Smart Materials and Structures*, 16(2):S300, 2007.

[60] RK Josephson. Contraction dynamics and power output of skeletal muscle. *Annual review of physiology*, 55(1):527–546, 1993.

[61] William M Kier and Kathleen K Smith. Tongues, tentacles and trunks: the biomechanics of movement in muscular-hydrostats. *Zoological journal of the Linnean Society*, 83(4):307–324, 1985.

[62] Robert K Josephson. Mechanical power output from striated muscle during cyclic contraction. *Journal of Experimental Biology*, 114(1):493–512, 1985.

[63] Kenneth Meijer, Marc S Rosenthal, and Robert J Full. Muscle-like actuators? a comparison between three electroactive polymers. In *Smart*

Structures and Materials 2001: Electroactive Polymer Actuators and Devices, volume 4329, pages 7–16. International Society for Optics and Photonics, 2001.

[64] Andrew P Mizisin and Robert K Josephson. Mechanical power output of locust flight muscle. *Journal of Comparative Physiology A: Neuroethology, Sensory, Neural, and Behavioral Physiology*, 160(3):413–419, 1987.

[65] Christoph Keplinger, Jeong-Yun Sun, Choon Chiang Foo, Philipp Rothemund, George M Whitesides, and Zhigang Suo. Stretchable, transparent, ionic conductors. *Science*, 341(6149):984–987, 2013.

[66] Baohong Chen, Jing Jing Lu, Can Hui Yang, Jian Hai Yang, Jinxiong Zhou, Yong Mei Chen, and Zhigang Suo. Highly stretchable and transparent ionogels as nonvolatile conductors for dielectric elastomer transducers. *ACS applied materials & interfaces*, 6(10):7840–7845, 2014.

[67] Canhui Yang and Zhigang Suo. Hydrogel ionotronics. *Nature Reviews Materials*, page 1, 2018.

[68] Jianfeng Zang, Seunghwa Ryu, Nicola Pugno, Qiming Wang, Qing Tu, Markus J Buehler, and Xuanhe Zhao. Multifunctionality and control of the crumpling and unfolding of large-area graphene. *Nature materials*, 12(4):321, 2013.

[69] Sze-Hsien Low and Gih-Keong Lau. Bi-axially crumpled silver thin-film electrodes for dielectric elastomer actuators. *Smart Materials and Structures*, 23(12):125021, 2014.

[70] Mihai Duduta, David R Clarke, and Robert J Wood. A high speed soft robot based on dielectric elastomer actuators. In *Robotics and Automation (ICRA), 2017 IEEE International Conference on*, pages 4346–4351. IEEE, 2017.

[71] AN Gent. A new constitutive relation for rubber. *Rubber chemistry and technology*, 69(1):59–61, 1996.

[72] Hristiyan Stoyanov, Paul Brochu, Xiaofan Niu, Christopher Lai, Sungryul Yun, and Qibing Pei. Long lifetime, fault-tolerant freestanding actuators based on a silicone dielectric elastomer and self-clearing carbon nanotube compliant electrodes. *RSC Advances*, 3(7):2272–2278, 2013.

[73] John DW Madden, Nathan A Vandesteeg, Patrick A Anquetil, Peter GA Madden, Arash Takshi, Rachel Z Pytel, Serge R Lafontaine, Paul A Wieringa, and Ian W Hunter. Artificial muscle technology: physical principles and naval prospects. *IEEE Journal of oceanic engineering*, 29(3):706–728, 2004.

[74] E Acome, SK Mitchell, TG Morrissey, MB Emmett, C Benjamin, M King, M Radakovitz, and C Keplinger. Hydraulically amplified self-healing electrostatic actuators with muscle-like performance. *Science*, 359(6371):61–65, 2018.

[75] Rahimullah Sarban, Jakob Oubaek, and Richard W Jones. Closed-loop control of a core free rolled eap actuator. In *Electroactive Polymer Actuators and Devices (EAPAD) 2009*, volume 7287, page 72870G. International Society for Optics and Photonics, 2009.

[76] Ye Rim Lee, Hyungho Kwon, Do Hoon Lee, and Byung Yang Lee. Highly flexible and transparent dielectric elastomer actuators using silver nanowire and carbon nanotube hybrid electrodes. *Soft Matter*, 2017.

[77] Samuel Rosset and Herbert Shea. Towards fast, reliable, and manufacturable deas: miniaturized motor and rupert the rolling robot. In *Electroactive Polymer Actuators and Devices (EAPAD) 2015*, volume 9430, page 943009. International Society for Optics and Photonics, 2015.

[78] Hareesh Godaba, Jisen Li, Yuzhe Wang, and Jian Zhu. A soft jellyfish robot driven by a dielectric elastomer actuator. *IEEE Robotics and Automation Letters*, 1(2):624–631, 2016.

[79] Tiefeng Li, Guorui Li, Yiming Liang, Tingyu Cheng, Jing Dai, Xuxu Yang, and Bangyuan Liu. Fast-moving soft electronic fish. *Science Advances*, pages 1–8, 2017.

[80] Chao Tang, Bo Li, and Hualing Chen. U-turning an agile robotic cube by a soft dielectric elastomer resonator. In *2018 IEEE International Conference on Soft Robotics (RoboSoft)*. IEEE, 2018.

[81] E-F Markus Henke, Samuel Schlatter, and Iain A Anderson. Soft dielectric elastomer oscillators driving bioinspired robots. *Soft robotics*, 4(4):353–366, 2017.

[82] Jun Shintake, Herbert Shea, and Dario Floreano. Biomimetic underwater robots based on dielectric elastomer actuators. In *Intelligent Robots and Systems (IROS), 2016 IEEE/RSJ International Conference on*, pages 4957–4962. Ieee, 2016.

[83] C Jordi, S Michel, and E Fink. Fish-like propulsion of an airship with planar membrane dielectric elastomer actuators. *Bioinspiration Biomimetics*, 2010.

[84] Jinwan Lim, Hyunjun Park, Jaemin An, Yeh-Sun Hong, Byungkyu Kim, and Byung-Ju Yi. One pneumatic line based inchworm-like micro robot for half-inch pipe inspection. *Mechatronics*, 18(7):315–322, 2008.

[85] Min-Saeng Kim, Won-Shik Chu, Jae-Hoon Lee, Yun-Mi Kim, and Sung-Hoon Ahn. Manufacturing of inchworm robot using shape memory alloy (sma) embedded composite structure. *International journal of precision engineering and manufacturing*, 12(3):565–568, 2011.

[86] T Umedachi, V Vikas, and BA Trimmer. Softworms: the design and control of non-pneumatic, 3d-printed, deformable robots. *Bioinspiration & biomimetics*, 11(2):025001, 2016.

[87] Sangok Seok, Cagdas Denizel Onal, Kyu-Jin Cho, Robert J Wood, Daniela Rus, and Sangbae Kim. Meshworm: a peristaltic soft robot with antagonistic nickel titanium coil actuators. *IEEE/ASME Transactions on mechatronics*, 18(5):1485–1497, 2013.

[88] Alan T Asbeck, Sangbae Kim, Arthur McClung, Aaron Parness, and Mark R Cutkosky. Climbing walls with microspines. In *IEEE ICRA*, 2006.

[89] Ron Pelrine, Roy Kornbluh, Qibing Pei, Scott Stanford, Seajin Oh, Joe Eckerle, Robert J Full, Marcus A Rosenthal, and Kenneth Meijer. Dielectric elastomer artificial muscle actuators: toward biomimetic motion. In *Proc. Spie*, volume 4695, pages 126–137, 2002.

[90] Michael Rubenstein, Alejandro Cornejo, and Radhika Nagpal. Programmable self-assembly in a thousand-robot swarm. *Science*, 345(6198):795–799, 2014.

[91] Andrew D. Marchese, Cagdas D. Onal, and Daniela Rus. Autonomous Soft Robotic Fish Capable of Escape Maneuvers Using Fluidic Elastomer Actuators. *Soft Robotics*, 1(1):75–87, 2014.

[92] Matteo Aureli, Vladislav Kopman, and Maurizio Porfiri. Free-locomotion of underwater vehicles actuated by ionic polymer metal composites. *IEEE/ASME Transactions on Mechatronics*, 15(4):603–614, 2010.

[93] X Tan, D Kim, N Usher, D Laboy, J Jackson, A Kapetanovic, J Rapai, B Sabadus, and X Zhou. An autonomous robotic fish for mobile sensing. *Proceedings of the IEEE/RSJ International Conference on Intelligent Robots and Systems (IROS)*, pages 5424–5429, 2006.

[94] Hyung-Jung Kim, Sung-Hyuk Song, and Sung-Hoon Ahn. A turtle-like swimming robot using a smart soft composite (ssc) structure. *Smart Materials and Structures*, 22(1), 2013.

[95] Zhenlong Wang, Guanrong Hang, Jian Li, Yangwei Wang, and Kai Xiao. A micro-robot fish with embedded SMA wire actuated flexible biomimetic fin. *Sensors and Actuators*, 144(2):354–360, 2008.

[96] Vladislav Kopman and Maurizio Porfiri. A miniature and low-cost robotic fish for ethorobotics research and engineering education i: bioinspired design. In *ASME DSCC—Dynamic Systems and Control Conference*, pages pp–MoBT6, 2011.

[97] Fangfang Liu, Kok-Meng Lee, and Can-Jun Yang. Hydrodynamics of an undulating fin for a wave-like locomotion system design. *IEEE/ASME Transactions on Mechatronics*, 17(3):554–562, 2012.

[98] Pablo Valdivia y Alvarado and Kamal Youcef-Toumi. Design of machines with compliant bodies for biomimetic locomotion in liquid environments. *Journal of dynamic systems, measurement, and control*, 128(1):3–13, 2006.

[99] R. P. Clark and A. J. Smits. Thrust production and wake structure of a batoid-inspired oscillating fin. *Journal of Fluid Mechanics*, 562:415–429, 2006.

[100] Florian Berlinger, Mihai Duduta, Hudson Gloria, David Clarke, Radhika Nagpal, and Robert Wood. A modular dielectric elastomer actuator to drive miniature autonomous underwater vehicles. In *Robotics and Automation (ICRA), 2017 IEEE International Conference on*, pages –. IEEE, 2018.

[101] W Gronenberg. Fast actions in small animals: springs and click mechanisms. *Journal of Comparative Physiology A*, 178(6):727–734, 1996.

[102] Robin Huw Crompton, William I Sellers, and Michael M Günther. Energetic efficiency and ecology as selective factors in the saltatory adaptation of prosimian primates. *Proc. R. Soc. Lond. B*, 254(1339):41–45, 1993.

[103] Mark Ilton, M Saad Bhamla, Xiaotian Ma, Suzanne M Cox, Leah L Fitchett, Yongjin Kim, Je-sung Koh, Deepak Krishnamurthy, Chi-Yun Kuo, Fatma Zeynep Temel, et al. The principles of cascading power limits in small, fast biological and engineered systems. *Science*, 360(6387):eaao1082, 2018.

[104] Rhodri Armour, Keith Paskins, Adrian Bowyer, Julian Vincent, and William Megill. Jumping robots: a biomimetic solution to locomotion across rough terrain. *Bioinspiration & biomimetics*, 2(3):S65, 2007.

[105] Mirko Kovac, Martin Fuchs, André Guignard, Jean-Christophe Zufferey, and Dario Floreano. A miniature 7g jumping robot. In *Robotics and Automation, 2008. ICRA 2008. IEEE International Conference on*, pages 373–378. IEEE, 2008.

[106] Minkyun Noh, Seung-Won Kim, Sungmin An, Je-Sung Koh, and Kyu-Jin Cho. Flea-inspired catapult mechanism for miniature jumping robots. *IEEE Transactions on Robotics*, 28(5):1007–1018, 2012.

[107] Sarah Bergbreiter and Kristofer SJ Pister. Design of an autonomous jumping microrobot. In *Robotics and Automation, 2007 IEEE International Conference on*, pages 447–453. IEEE, 2007.

[108] Ryuma Niiyama, Akihiko Nagakubo, and Yasuo Kuniyoshi. Mowgli: A bipedal jumping and landing robot with an artificial musculoskeletal system. In *Robotics and Automation, 2007 IEEE International Conference on*, pages 2546–2551. IEEE, 2007.

[109] Robert F Shepherd, Adam A Stokes, Jacob Freake, Jabulani Barber, Phillip W Snyder, Aaron D Mazzeo, Ludovico Cademartiri, Stephen A Morin, and George M Whitesides. Using explosions to power a soft robot. *Angewandte Chemie International Edition*, 52(10):2892–2896, 2013.

[110] Aaron P Gerratt and Sarah Bergbreiter. Incorporating compliant elastomers for jumping locomotion in microrobots. *Smart Materials and Structures*, 22(1):014010, 2012.

[111] Yuuta Sugiyama and Shinichi Hirai. Crawling and jumping by a deformable robot. *The International journal of robotics research*, 25(5-6):603–620, 2006.

[112] Huai-Ti Lin, Gary G Leisk, and Barry Trimmer. Goqbot: a caterpillar-inspired soft-bodied rolling robot. *Bioinspiration & biomimetics*, 6(2):026007, 2011.

[113] Qibing Pei, Ron Pelrine, Marcus A Rosenthal, Scott Stanford, Harsha Prahlad, and Roy D Kornbluh. Recent progress on electroelastomer artificial muscles and their application for biomimetic robots. In *Smart Structures and Materials 2004: Electroactive Polymer Actuators and Devices (EAPAD)*, volume 5385, pages 41–51. International Society for Optics and Photonics, 2004.

[114] Samuel Rosset, Oluwaseun A Araromi, Jun Shintake, and Herbert R Shea. Model and design of dielectric elastomer minimum energy structures. *Smart Materials and Structures*, 23(8):085021, 2014.

[115] R McN Alexander. Leg design and jumping technique for humans, other vertebrates and insects. *Phil. Trans. R. Soc. Lond. B*, 347(1321):235–248, 1995.

[116] MEG Evans. The jump of the click beetle (coleoptera, elateridae)—a preliminary study. *Journal of zoology*, 167(3):319–336, 1972.

[117] Ophelia Bolmin. *Observing and modelling the legless jumping mechanism of click beetles for bio-inspired robotic design*. PhD thesis, 2017.

[118] Philippe Marmottant, Alexandre Ponomarenko, and Diane Bienaimé. The walk and jump of equisetum spores. *Proc. R. Soc. B*, 280(1770):20131465, 2013.

[119] A López-Puerto, F Avilés, F Gamboa, and AI Oliva. A vibrational approach to determine the elastic modulus of individual thin films in multilayers. *Thin Solid Films*, 565:228–236, 2014.

[120] MEG Evans. The jump of the click beetle (coleoptera: Elateridae)—energetics and mechanics. *Journal of zoology*, 169(2):181–194, 1973.

[121] Ehsan Hajiesmaili and David R Clarke. Reconfigurable shape-morphing dielectric elastomers using spatially varying electric fields. *arXiv preprint arXiv:1809.09301*, 2018.